11-9-2022

Numerical Modeling and Analyses of a Crankshaft System as a Reciprocating-Airfoil (Ra) Driver for Ra-based VTOL Aircraft

Mohammad Didarul Alam
malam052@fiu.edu

FLORIDA INTERNATIONAL UNIVERSITY

Miami, Florida

NUMERICAL MODELING AND ANALYSES OF A CRANKSHAFT SYSTEM AS A RECIPROCATING-AIRFOIL (RA) DRIVER FOR RA-BASED VTOL AIRCRAFT

A dissertation submitted in partial fulfillment of

the requirements for the degree of

DOCTOR OF PHILOSOPHY

in

MECHANICAL ENGINEERING

by

Mohammad Didarul Alam

2022

To: Dean John L. Volakis
College of Engineering and Computing

This dissertation, written by Mohammad Didarul Alam, and entitled Numerical Modeling and Analyses of a Crankshaft System as a Reciprocating-Airfoil (RA) Driver for RA-Based VTOL Aircraft, having been approved in respect to style and intellectual content, is referred to you for judgment.

We have read this dissertation and recommend that it be approved.

Ibrahim Nur Tansel

Bilal El-Zahab

Armando Barreto

Yiding Cao, Major Professor

Date of Defense: November 09, 2022

The dissertation of Mohammad Didarul Alam is approved.

Dean John L. Volakis
College of Engineering and Computing

Andrés G. Gil
Vice President for Research and Economic Development
and Dean of the University Graduate School

Florida International University, 2022

DEDICATION

Dedicated to my parents and friends.

ACKNOWLEDGMENTS

I would like to express my sincere appreciation and gratitude to my wonderful advisor, Professor Yiding Cao, for his valuable advice throughout my study. His guidance, support, and patience were essential to the completion of this dissertation. I would also like to acknowledge my doctoral committee, Professor Ibrahim Nur Tansel, Professor Bilal El-Zahab, and Professor Armando Barreto, for their efforts in providing advice and suggestions that have improved this dissertation.

I am also thankful to the Department of Mechanical & Materials Engineering and FIU graduate school for all types of support including graduate assistantships, scholarships, and fellowships. I highly appreciate the help and support from all of my colleagues, especially, Soheil Soleimanikutanaei and Majid Almas.

Finally, I wish to express my deepest gratitude to my family members for their love, encouragement, and support.

ABSTRACT OF THE DISSERTATION

NUMERICAL MODELING AND ANALYSES OF A CRANKSHAFT SYSTEM AS A RECIPROCATING-AIRFOIL (RA) DRIVER FOR RA-BASED VTOL AIRCRAFT

by

Mohammad Didarul Alam

Florida International University, 2022

Miami, Florida

Professor Yiding Cao, Major Professor

Since the invention of fixed-wing airplanes, they remain the dominant air-transportation vehicles. However, the airplane's massive runway requirement and airport maintenance would hinder its widespread uses without the convenience of the automotive transportation systems. On the other hand, the helicopter was invented more than 80 years ago, but still with very limited civilian air-transportation markets. Helicopters' inherent flight mechanism is too noisy and complex, and poses a compromised safety due to aerodynamic balancing challenges, making them expensive for mass-scale transportation applications. Likewise, despite initially showing promise in terms of small drone/UAV flight demonstration, rotary-fan-driven vertical takeoff and landing (VTOL) technology also failed to become a viable VTOL technology due to fans' poor lifting capability and low energy efficiency. It is anticipated that an efficient VTOL technology would be a stepping stone that will revolutionize the transportation system and overcome the present traffic congestion problem. As a motivation from the existing technological limitations and growing demands, the novel Reciprocating Airfoil (RA) driven VTOL technology has been invented and promises to become an efficient VTOL technology.

The primary objective of this research is to design and develop a crankshaft reciprocating driver for the novel RA-driven VTOL aircraft. The reciprocating driver is a critical component of the novel VTOL technology to produce the long-stroke reciprocating motion of the two wings in an RA aircraft module to generate the necessary lift during takeoff. The nonlinear three-dimensional static models were developed to study the response of the designed reciprocating driver under different working conditions in conjunction with the analytical and rigid body dynamic studies. Additionally, modal and nonlinear eigenvalue analyses have been conducted to avoid possible vibration and buckling failures. The numerical model was validated against the available referenced experimental result. The structural parameters examined include total deformation, von-Mises and maximum principal stresses, and equivalent and maximum principal strains, all of which are acceptable to the present structural design. The average safety factor under the highest loading is above 14. The maximum stress is developed in the corner zone at the junction between the main shaft and the crank web. The close resonance frequency is 26.51 Hz whereas the working frequency of the crankshaft is 12 Hz. As a result, the possibility of resonance is low. The reciprocating driver response during operation under different safety tools and useful design recommendations have been produced, all of which provide archival information for the successful implementation of the crankshaft reciprocating driver. In brief, this research will beacon the development of a new fixed-wing aircraft with an added VTOL capability. Moreover, considering the unique and efficient lifting capability, the RA-driven VTOL technology could also be deployed for drone and unmanned aerial vehicle applications.

TABLE OF CONTENTS

CHAPTER PAGE

LIST OF TABLES

TABLE PAGE

LIST OF FIGURES

TABLE PAGE

Chapter 1:

1 Introduction

1.1 History of the novel Reciprocating-Airfoil (RA) Driven VTOL Aircraft

Human has a long-cherished dream to design and develop more efficient Vertical Takeoff and Landing (VTOL) technology vehicles for widespread applications. These applications may include a new mode of transportation system to overcome the current traffic congestion problem, a new delivery system, an automated guided vehicle system, and military/surveillance systems. As a result, fixed-wing aircraft with added vertical takeoff and landing capability to overcome helicopter limitations have been exploited for many years. However, the success is not noticeable so far as a fixed-wing aircraft still needs a massive runway and airport. On the other hand, the helicopters' inherent flying mechanisms are too noisy, inefficient, and polluting, and pose a complex aerodynamic balancing challenge. Most importantly, the helicopter is expensive and unreliable for large-scale commercial applications.

Over the last 70 years, to improve the performance of helicopters, numerous VTOL technologies have been developed all over the world in terms of hybrid aircraft/drone/unmanned aerial vehicles but with limited success. For instance, V-22 Osprey (developed by the USA) and Yak-38 Forger (developed by Russia) were the initial inventions of the hybrid VTOL systems [1][2]. Their flying mechanisms involved short-run takeoff and landing (STOL) or jump style. However, the Yak-38 forger was never in operation since the aircraft was outrageously complicated and had inconsistent flight

characteristics. The Bell Boeing V-22 Osprey was highly successful but has only limited applications for military service. Hawker Siddeley P.1127 and MV-22 were the most remarkable VTOL systems that had been developed so far but still with limited success [3–6].

One of the most common and widely used types of VTOL systems is Rotary-fan-driven flying mechanisms, such as amazon delivery drones, Flytrex drones, DHL delivery drones, Wing aviation, Manna, etc [7–9]. Initially, the rotary fan-driven flying mechanism showed promise. However, the mainstreaming implementation of the rotary fan-driven VTOL system has been curtailed due to complex flying mechanisms, poor lifting capacity, and safety issues. As a result, Amazon is still unable to provide us with a moderate lifting-capable delivery drone since its first take-off flight in 2013. Likewise, DHL has already officially abandoned its Parcelcopter delivery drone project after spending millions of dollars. The key limitation of rotatory fan-driven VTOL system is poor lifting capacity, short flying range, and inefficient energy density. As mentioned earlier, another type of flying mechanism is a hybrid VTOL system where a rotary fan is incorporated for vertical takeoff and landing in conjunction with the fixed-wing setup [10,11]. The most common examples are tail-sitters and convertiplanes. However, all their success has been constrained by limitations.

As a motivation from the current state of the art in VTOL technologies, a novel VTOL technology called reciprocating-airfoil (RA) driven VTOL aircraft has been invented based on which the challenges that hinder the widespread application of helicopters can be

overcome [12]. Figure 1.1 represents a SolidWorks model design of the novel aircraft [13]. In this aircraft, the reciprocating airfoil (RA) wing works in cycles, each including a forward stroke and a reverse stroke during the taking-off and landing operation. Fig. 1.2 represents a schematic of a reciprocating cycle including forward and reverse strokes. The airfoil moves back and forth within a limited stroke, and near each dead-end of the stroke, it is actuated to rotate an angle while reversing the direction with a positive effective angle of attack (AoA). However, once the aircraft reaches the cruise altitude and gains enough flight speed, the reciprocating wings can stop reciprocating and work as fixed wings, so that the aircraft can operate as a fixed-wing aircraft utilizing the airflow due to the aircraft's flight speed to generate lift [14]. In brief, the novel aircraft can be called a natural extension of fixed-wing aircraft with added capabilities for vertical takeoff and landing.

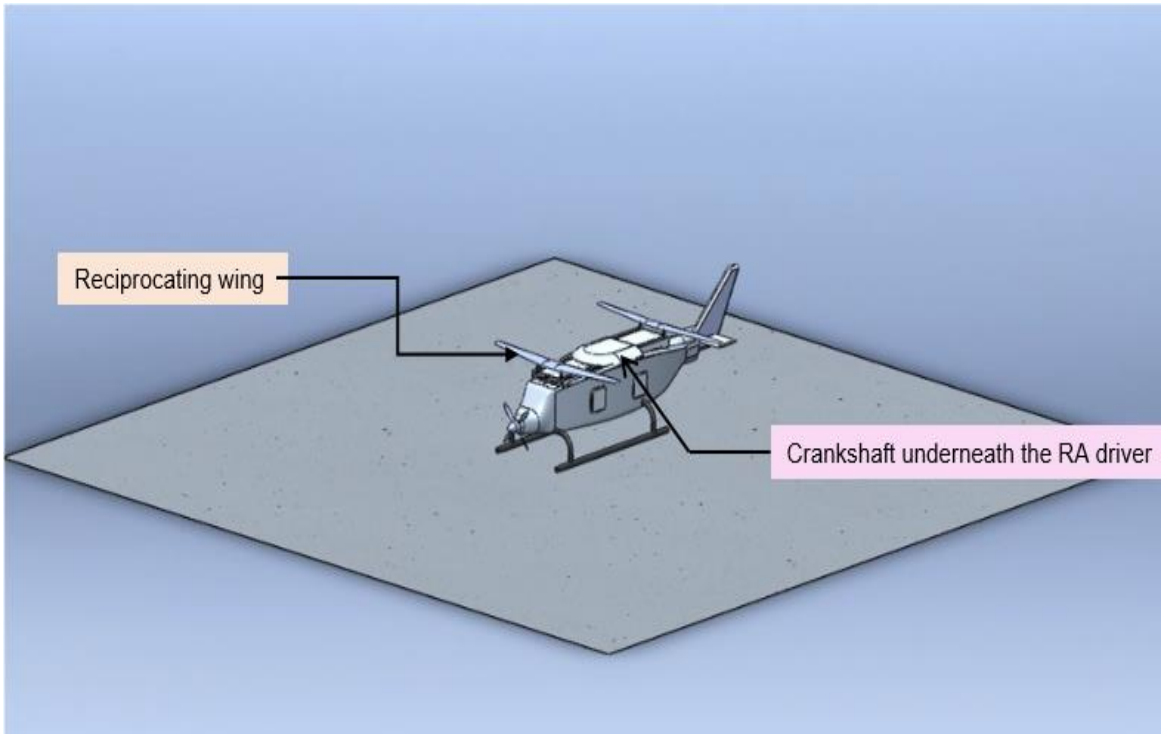

Figure 1.1 CAD Model of Reciprocating-Airfoil (RA) Driven VTOL Aircraft

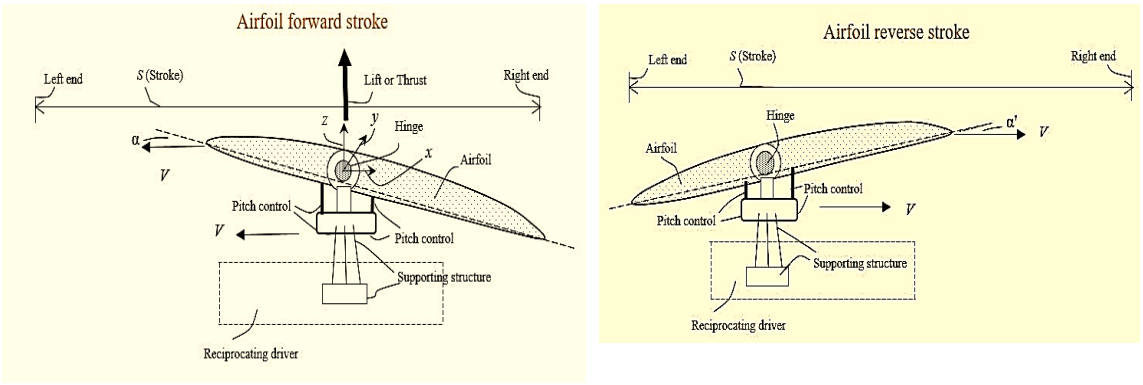

Fig.1.2: Schematic illustration of a reciprocating cycle: (a) Forward stroke and (b) Reverse stroke[12, 14].

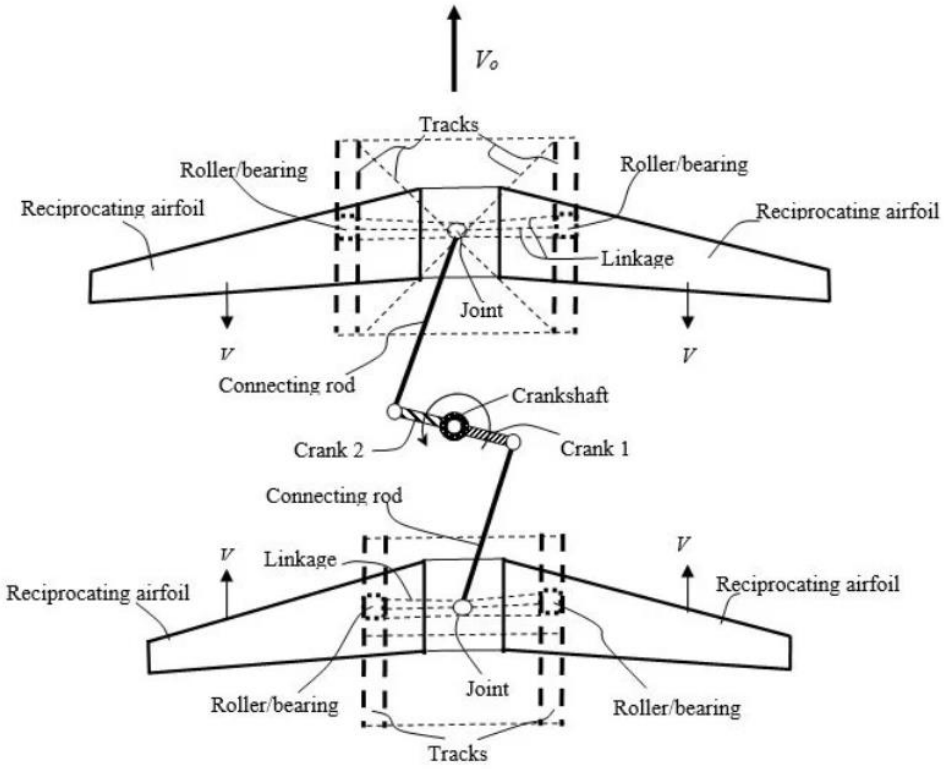

V: Reciprocating speed relative to vehicle/Vo: Vehicle flight speed

Fig 1.3: Schematic diagram of a RA module [12, 14].

A schematic diagram of the RA module can be seen in figure 1.3. For balancing purposes, reciprocating airfoils may be deployed in modules. An RA module includes two airfoils that reciprocate simultaneously with the same velocity magnitude but in opposite directions to substantially cancel out the inertia forces and moments associated with the individual airfoils. As shown in figure 1.3, two reciprocating airfoils reciprocate, with the respective roller/bearing, in a front-back direction of the vehicle to take the advantage of the functionality of fixed wings during the cruise. In this case, the crankshaft is disposed in a direction substantially perpendicular to the vehicle's top surface and the two cranks 1 and 2, are arranged along the length of the crankshaft [12, 14]. They could take streamlined shapes to reduce aerodynamic losses. In addition, by adding blades or shaping crank arms like airfoils or fan blades, the crankshaft system could also act as a fan that produces additional lift for vertical takeoff and landing. During the cruise, when the crankshaft is not operating, the top of the crankshaft system may be covered. For more complete balancing of the inertia forces and moments or larger wing area, more than one RA module may be deployed (not shown). These modules may be disposed at different elevations and reciprocate with different speeds or directions at a given time. To improve the rigidity of the tracks, the two tracks for each airfoil may be integrated into a truss or another suitable structure and the track structure would be directly assembled into the aircraft body, as shown in Fig. 1.3. To minimize the weight penalty, aircraft backbones can be used as tracks. As will be seen in Technical Data [14], the spacing between the two airfoils could be rather small.

1.2 Aerodynamic performance of the novel RA-driven aircraft

An extensive computational aerodynamic study has been undertaken and some of the results are shown in Fig. 1.4 and 1.5. The governing equations including continuity and momentum have been solved using Ansys Fluent commercial solver. The coupled algorithm along with PRESTO scheme was used to solve the Navier-Stokes equations. The realizable k-ε model with enhancing wall function is used as the turbulence model in this study. The second-order upwind and first-order methods were used for space and time discretization respectively. The Dynamic Mesh Motion available in Ansys Fluent was used to model the airfoil motion as a moving rigid body. The airfoil velocity U (t) and rotational velocity around the airfoil's point of impact Ω (t) was implemented by User-Defined functions (UDF) using the dynamic mesh macro DEFINE_CG_MOTION. The time step for all simulations was set to 2e-5 s.

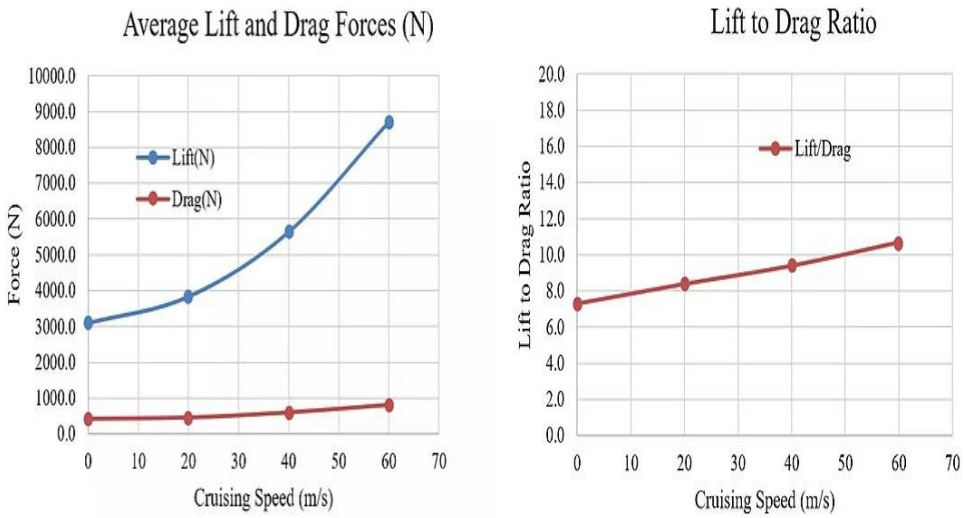

Fig.1.4: Three-dimensional Computational Results of a Reciprocating Wing (S1223) at different Aircraft Flight Speeds[14].

The fig 1.4 shows lift and drag (left), and lift-to-drag ratio (right) as a function of aircraft flight speed at an angle of attack of 12 for both forward and reverse strokes, with a chord of 0.25 m, aspect ratio: 16, a total airfoil planform area: 1 m^2, an average airfoil reciprocating speed of 50 m/s, and a reciprocating stroke of 2 m. A positive AoA for both strokes is maintained through the rotation of the airfoil around the leading edge near each end of the stroke.

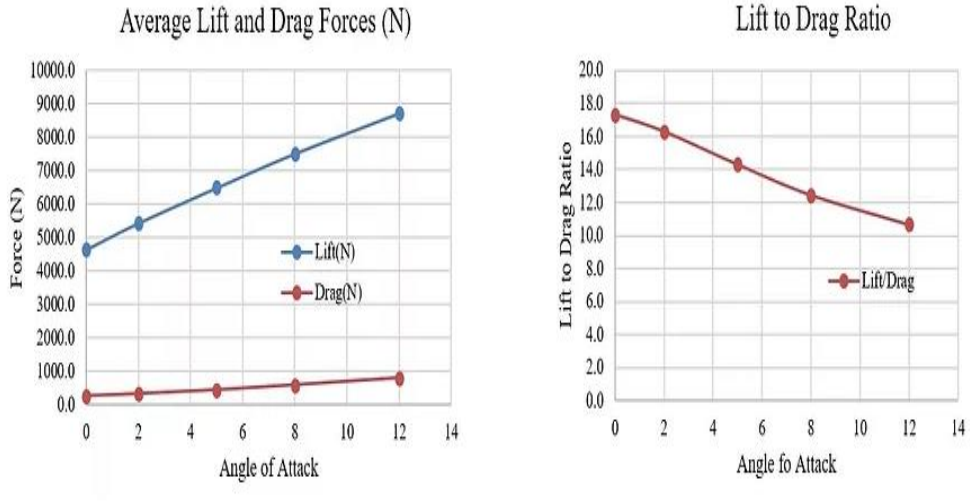

Fig.1.5: Three-dimensional Computational Results of a Reciprocating Wing (S1223) at different Aircraft angles of attacks[14].

Fig. 1.5 shows lift and drag (left), and lift-to-drag ratio (right) as a function of the angle of attack for both forward and reverse strokes at an aircraft cruise speed of 60 m/s (134 mph), with a chord of 0.25 m, aspect ratio: 16, a total airfoil planform area: 1 m^2, an average airfoil reciprocating speed of 50 m/s, and a reciprocating stroke of 2 m. A positive AoA for both strokes is maintained through the rotation of the airfoil around the leading edge at each end of the stroke.

For more detailed results regarding the aerodynamic performance of the RA-driven wings please see the referenced website [14]. Based on the results, it shows that during the aircraft takeoff (zero cruise speed), the reciprocating wing approaches the performance of a fixed-wing with a lift-to-drag ratio more than 70% higher than that of a helicopter main rotor. At a high cruise speed, the lift force increases significantly, so that the reciprocating wing would reduce its reciprocating speed and eventually come to a complete stop to function as a fixed wing and use the aircraft's cruise speed to generate the needed lift.

1.3 Advantages of RA-driven Aircraft

To evaluate the advantage of RA-driven aircraft, a comparison has been made between RA-driven aircraft and helicopters or rotorcraft. According to the invention, RA-driven VTOL aircraft may have the following technological advantages [14]:

1. Significantly improved safety and reliability.

The motion of the airfoil of this invention is linear and reciprocating, and the primary concern related to potential vibration is the balance of the inertia forces and moments due to the reciprocating motion. The system may be easily balanced by using more than one airfoil unit similar to the use of multiple horizontally-opposed pistons/cylinders in a reciprocating compressor. Unlike the situation in helicopters, even if the balance is imperfect, it is unlikely to cause catastrophic failure due to the nature of bidirectional motion. As a result, many difficult issues related to helicopters, such as anti-torque mechanisms and in-flight control of vibration and instabilities, are removed. Thus, an

aircraft built upon the system of this invention may have significantly improved safety and reliability [14].

2. Large cost reduction.

The present system may employ airfoils similar to conventional fixed-wing airfoils and a conventional crankshaft driver similar to that in a reciprocating compressor with costs potentially much lower than that of the main rotor system in a helicopter. The lower costs of the aircraft of this invention may enable their penetration into mass markets [14].

3. Great modularity and controllability.

Multiple airfoil assemblies may be flexibly deployed at different locations of a vehicle for the benefit of the operation and to balance inertia forces and moments. For example, a plurality of airfoils may be arranged on the top or bottom surface of a vehicle, which may share the same reciprocating driver or be driven by separate drivers. Additionally, more than one airfoil assembly may be deployed in a vertical direction, which may share the same reciprocating driver. For helicopters, however, the deployment of multiple rotors is a challenging undertaking. For these reasons, an aircraft of this invention may be able to deploy a much larger airfoil area per unit volume of the aircraft's main body, resulting in a significantly reduced footprint as compared to a helicopter of similar loads, which may enable entering passenger transportation markets in crowded urban areas [14].

4. Greatly improved energy efficiency, flight range, and flight speed compared to helicopters.

The performance of a reciprocating airfoil may match or exceed the performance of a fixed wing of similar size and can have a lift and lift-to-drag ratio much greater than those of a helicopter main rotor. Consequently, an aircraft equipped with the present lift or thrust system could have a significantly improved flight range due to the greatly increased energy efficiency. The aircraft of this invention can also fly much faster than the helicopter because the reciprocating airfoils of this invention may be shaped like fixed wings and function as fixed wings during the cruise. The aircraft of this invention is thus a natural extension of fixed-wing aircraft with added functionality for vertical takeoff and landing [14].

5. Significantly reduced performance difference between the infinite-span airfoil and finite-span wing.

In a fixed-wing aircraft, the lift-to-drag ratio of a finite-span wing is significantly lower than that of a corresponding infinite-span airfoil due to the trailing-edge vortex that induces a downward velocity component, called downwash. Due to the reciprocating motion of the airfoil of this invention, at a sufficiently high frequency, the induced downwash may be difficult to be established. Considering the motion of an airfoil with a finite span moving from the right end to the left end in a stroke, the downwash may attempt to develop near the trailing edge at the right end of the airfoil. However, before the downwash may have been fully established, the airfoil may have reached the left dead end. The left leading edge moves downward to become a trailing edge and the right trailing edge moves upward to become a leading-edge while the airfoil changes direction and moves from the left to the right. These combined actions may quickly eliminate the downwash before it is fully

established. Consequently, the lift-to-drag ratio of the airfoil of this invention with a finite span may potentially approach that of a reciprocating airfoil with an infinite span [14].

1.4 Project Motivation and Research Objectives

As a motivation from the existing technology limitation and new modes of transportation demands, a novel Reciprocating Airfoil-driven VTOL aircraft has been invented where the crankshaft assembly works as a reciprocating driver to generate the necessary lift and drag during takeoff and landing time. The crankshaft reciprocating driver is considered the critical component for the successful deployment of the new RA-driven aircraft. Since the reciprocating driver not only reciprocate the two wing simultaneously but also has to handle a large inertia loading condition due to its dynamic nature, the structural rigidity of the crankshaft driver is a very critical challenge. The aim of this project is to design and develop a crankshaft reciprocating driver for this challenging application and ensure structural rigidity for its successful operation in the new VTOL aircraft. The conventional crankshaft system is inappropriate in this application because the current system requires a large crank radius, long connecting rods, and a small weight while handling large inertia forces simultaneously. Preliminary studies have already shown that the traditional crankshaft failed to meet the present design requirements. The crankshaft driver development is considered to be one of the most important and challenging steps toward the successful demonstration of the new aircraft.

The objective of this research is to numerically design and develop a crankshaft reciprocating driver in such a way that it can be replicable and manufactured, and serve as an example of reference study in structural mechanics. Regarding that, at the beginning of the study (Chapter two), it illustrates the fundamental science and law in structural mechanics, different failure criteria of the structure, mechanics of material, the state of the art in numerical method, advanced numerical procedures, and quality parameters for highest accuracy. Chapter three provides the detail of the underlying mechanics within the crankshaft driver during operation by using both analytical and rigid body dynamic methods that can be used to study any multibody dynamic system. After that, Chapter four established the detailed studies of the crankshaft in terms of nonlinear static and vibrations studies where the crankshaft is carefully investigated and analyzed. Finally, the connecting rod design and development were summarized in Chapter five for the successful development of a crankshaft reciprocating driver.

1.5 Literature Review

The purpose of the study is to design and develop a crankshaft reciprocating driver for the novel RA-driven VTOL aircraft. The crankshaft system is widely used to perform the conversion between rotary and reciprocating motions in automotive applications. It is considered the backbone of an internal combustion engine. Due to sophisticated loading conditions and stringent requirements, the design and development of a crankshaft system have always been very important tasks for automotive manufacturers to satisfy low costs, minimum weight, sufficient strength, and other functional requirements. System design

and development are commonly practiced in several ways. Among them, finite element analysis (FEA) based numerical simulation is the best tool for designing the crankshaft system with low economical cost and few limitations. FEA facilitates the easy and inexpensive study of random pairs of input parameters along with the design and manufacturing requirements. Numerous successful designs use the finite element analysis technique and have produced products on the markets.

Heath and McNamara [15] presented a crankshaft study in combination with finite element and classical methods. Along with the classical methods, their study performed various levels of FE analysis where the crankshaft stress field was generated during the engine's entire cycle. Also, crankshaft fatigue life was performed to evaluate the fatigue safety factor on the crankshaft surface. This level of detail study can be used further for failure investigation, design optimization, and improvement.

Shrinivasa et al [16] made a detailed discussion about the limitation of the classical crankshaft design approach which is based heavily on empirical formulas and in-house experience. For better efficacy, they developed a systematic procedure to design their crankshaft where both advantages from the classical method and finite element method were exploited. A simulation software named TVAL was developed and used to calculate the crankshaft's natural frequencies, critical modes, displacement, and stresses. Their finding emphasized the accuracy of the FEM method compared with the classical design approach.

Garcia et al [17] investigate a catastrophic crankshaft failure for a four-stroke 18 V diesel engine for power plant application. For the necessary investigation, a finite element model has been developed, and the crankshaft was modeled to predict the most fractured zone.

Based on the result, the FEM model correctly predicts the fracture zone of the crankshaft during operation. Also, the physical investigation of the fracture zone location was matched with the FEM method prediction. The fracture occurred in the web between the 2nd journal and the 2nd crankpin.

Silva et al [18] performed a detailed study regarding the failure of 7 crankshafts reported between 1995-2020. The purpose of their study is to figure out the major failure reasons for crankshaft failure. According to the study findings, The crankshafts' major failures were the influence of material imperfections, fillet effect, fatigue, and unwanted vibration. The study also developed a Finite element model and investigated the crankshafts failure criterion.

Mourelatos [19] performed crankshaft structural analysis by using the Finite-element method and dynamic sub structuring with Ritz vectors and predicted the dynamic response during operation. During analysis, the crankshaft was coupled with the engine block which was incorporated as a distributed linear elastic foundation inside the FEM solver. The analysis addressed the nonlinearity between the journal and the corresponding engine block. Finally, the accuracy of the analysis was established by the comparison between the result from analytical prediction and experimental results.

Montazersadgh and Fatemi [20] investigated the weight and cost minimization scopes for a forged steel crankshaft. In this study, finite element analysis has been used to model individual cranks, and the superposition of stresses was reckoned from unit load analysis, resulting in stress history at different locations on the crankshaft geometry during an entire engine cycle.

Peng and Zhang [21] developed a crankshaft and studied its dynamic characteristics numerically for mud pump applications. The study investigated maximum and minimum main stress as well as the von Mises stress under three different critical working conditions. The maximum stresses of the crankshaft in different operating modes were obtained, which are located in the critical regions of the failure zone in most fractured crankshafts.

Kang et al.[22] investigated the coupled modes for non-rotating crankshafts by using finite element models of both beam and solid elements that are under a free–free suspended condition. Two model results are obtained and compared with experimental data. Based on their results, it is evident that the solid-element model is more appropriate than the beam-element model for modal analysis of the crankshaft.

Imumbhon et al. [23] executed FE analysis for the structural design of a high-lift, low Reynolds number airfoil profile, the Selig S1223, under reciprocating inertial force loading, to determine the feasibility of its use in a new reciprocating airfoil (RA) driven VTOL UAV. The developed stress and strain under the loading conditions were satisfactory and the designed wing could sustain the high reciprocating inertia forces in the RA-driven VTOL UAV module. Similarly, the crankshaft has also been designed and developed for that aircraft application[24].

Similarly, Thejasree et al. [25] modeled and analyzed a crankshaft for a passenger car by using the ANSYS solver. The study showed distortion and stress development during the operation and provided conceptual support to enhance the design by weight reduction.

Witek et al. [26] performed stress and failure analyses of a diesel engine crankshaft. To explain the premature crankshaft damage, the finite element method (FEM) was utilized. The results of the nonlinear static analysis showed that the high-stress area was located in

the crack initiation zone during the operation of the engine with maximum power. It was concluded that the main reason for premature fatigue failure was the high-cycle fatigue of the material in the external zone of the crankpin where the small structural radius was designed.

Shahane and Pawar [27] performed static and dynamic structural analyses on a single-cylinder four-stroke diesel engine crankshaft to obtain the variation of stresses at different critical locations of the crankshaft. Also, the optimization of the crankshaft in terms of geometrical area and shape was studied by using an Ansys solver. The finding of the study concluded that the optimized design should replace the existing crankshaft for the engine block and head. The finding helped to reduce the weight of the original crankshaft by 4.37%. A similar study was conducted by Singh et al. [28]. Their study includes the static analysis of a four-cylinder engine crankshaft as well as the use of different methods to optimize the crankshaft in terms of weight, stress, and cost reduction.

Aliakbari [29] analyzed the fatigue failure of fractured truck crankshafts. The study contains several experimental studies including chemical composition, material strength, hardness, and microstructure to evaluate the cause of the failure. In addition, a nonlinear three-dimensional stress analysis model is used to estimate the crankshaft stress field under cyclic bending combined with steady torsion. The numerical stress analysis is in good agreement with those obtained in the experimental field measurements and indicated that the highest stress is in the crankpin–web fillet zone.

Mateus et al. [30] studied the cause of the failure of a well-known 1900 cm^3 turbo diesel engine. Their study finding concluded that the fatigue failure was predominantly due to the

failure of the crankshaft. To understand the failure mode and mechanism, fractographic, metallographic, and numerical analyses were conducted.

Jiao et al.[31] investigated the causes of multiple failures of a KL crankshaft. Their studies include physical and chemical studies along with the modal and fatigue analysis performed by FEM solver ANSYS. Based on their results, fatigue is the main failure mode of the crankshaft.

Finite element method-based connecting rod design is also well-established and widely practiced[32–37]. Webster et al. [38] executed a three-dimensional finite element analysis for a high-speed diesel engine connecting rod under the maximum compressive load and the maximum tensile load. The study modeled the connecting rod cap separately and also modeled the bolt pretension using beam elements and multi-point constraint equations. Similarly, Folgar et al. [39] designed a composite connecting rod via FEA based on the loads from the kinematic analysis. After that, they built the prototype and tested the strength of the both crank end and piston pin end.

Mantovani et al [40] presented a detailed study about connecting rod failure in terms of common and uncommon failure. They developed a FEA based numerical model to interpret connecting rod failure reason. Before the numerical modeling, a physical inspection has been done to check the failure modes of the connecting rod. The study also included a brief extension to tribological problems.

Zelec et all [41] investigated failure and stress analysis of a turbocharged diesel engine connecting rod. They performed a nonlinear static structural analysis via Ansys solver and showed that the high-stress zones were located in the crack origins when the engine operated with maximum power. The study concluded that the main reason for the

connecting rod's failure was a high-stress level in zones near the bolt hole caused by the high pretension of bolts. Rabb [42] numerically investigated the failure of an engine connecting rod in a detailed fashion. The study clearly showed that the connecting rod failure location at the thread root was due to the improper screw thread profile. Ilman and Barizy [43] analyze the failure of a reciprocating air compressor that is subjected to complex dynamic loads. They analyzed the connecting rod's chemical composition, microstructural examination using optical microscopy, hardness, and tensile tests, scanning electron microscopy (SEM) fractography, and stress analysis. The cause of failure was low cycle fatigue and the initial crack location was consistent with high-stress concentration located at the fillet radius.

Along with stress analysis, connecting rod fatigue life is another key research interest. Plenty of studies are attempted regarding the connecting rod fatigue life via the FEA approach [44–48]. In literature, numerous studies in different fields have been performed using FEA [49]. Omid et all [50] investigated a universal tractor connecting rod through the ANSYS solver and estimated its lifespan. The study emphasized that connecting rod behavior is affected strongly by the fatigue phenomenon for cyclic loading. Based on the findings, it suggests the necessary modification to ensure a better life span as well as manufacturing. In literature, connecting rod’s FEA optimization can also be found [51–53]. Shenoy and Fatemi [54] performed an optimization on a steel forged connecting rod toward weight and production cost minimization. The weight minimization has been performed under a cyclic load constituted with tensile and compressive forces. They proposed an optimized connecting rod that is 10% lighter and 25% less expensive. Hippliti [55] studied the shape optimization of a connecting rod by parametric yield study using

2D- and 3D-FE models. Some studies also tried to optimize the connecting rod by using topology and geometric optimization [49,56]. Although the stress and fatigue life was the center of research attention, the significance of buckling is not negligible to ensure its safety and adequate life cycle. A few studies have already been attempted on connecting rod buckling phenomena [32,57]. Jang et all [58] performed a buckling sensitivity of a connecting rod to reduce its shank sectional area. They demonstrate FEA approaches that evaluate the first and second modes of buckling phenomena. The stress sensitivity in buckling is relatively higher than in the stress and fatigue analysis. Further, they emphasized that during connection rod shank weight reduction buckling should be considered an essential factor.

In the studies discussed above, the crankshaft systems are all for internal combustion (IC) engine applications. On the other hand, the crankshaft of this study is the reciprocating driver to generate long-stroke reciprocating motions of the wings in the reciprocating airfoil-driven VTOL aircraft [12]. Still, because of the similar configurations, a lot can be learned from the state-of-the-art IC engine crankshaft designs for the present VTOL vehicle applications. Also, FEM analyses are well-established methods for crankshaft design and can be employed for the present structural analyses. However, the current system has significant differences from the conventional crankshaft systems. The conventional crankshaft is characterized by a small crank radius with less inertial load, strong combustion loads, high rotational speed, and a high-temperature working environment. Weight is an important issue but is not very stringent because of ground applications. On the other hand, the present crankshaft demands a much larger crank radius to produce a

sufficiently long reciprocating stroke of the wings and requires the capability to handle large inertial force associated with the mass of the wing assembly. Most importantly, for the present aircraft/air-taxi/drone applications, weight minimization is critical. Similarly, the connecting rod must be much longer than the conventional one with minimum weight and a suitable life cycle. Along with the above requirements, safety would be the highest priority in the design. Therefore, combining all the challenges, the present work would signify its novelty.

Chapter 2

2 Theory and Numerical Procedure

2.1 Summary of the Chapter

The purpose of this chapter is to provide background information about solid mechanics and the finite element method. At the beginning of the chapter, a detailed discussion and necessary governing equations for solid mechanics are presented for a fundamental understanding of solid mechanics in mathematical form. Then, different types of structural failure modes and their respective mechanisms were thoroughly discussed along with the necessary mathematical formulations, and different materials models and their similarities and dissimilarity are discussed thoroughly. The later portion of the chapter would discuss finite element methods, the steps in finite element analysis, types of grid/mesh and the quality parameters in the finite element method, the source of nonlinearity in the structural analysis, etc. This chapter would establish a strong reference in terms of solid mechanics and the finite element method solution procedure so that they can be used for successful structural modeling and analyses.

2.2 Governing Equations for Solid Mechanics

In solid mechanics, the deformation of a body can be expressed by its displacement fields {u}which is a function of position. Because of the vector in nature, the displacement field can be expressed as follows:

$$\{u\} = \left\{u_x, u_y, u_z\right\} \tag{1}$$

The stress in a body under loading conditions is generally defined as the force per unit area. There are two types of stress developed in a structure: (a) normal stress and (b) shear stress. Normal stress acts perpendicular to the face whereas the shear stress always acts parallel to the associated face. For demonstration purposes, let's consider a six faces cube in Fig 2.1

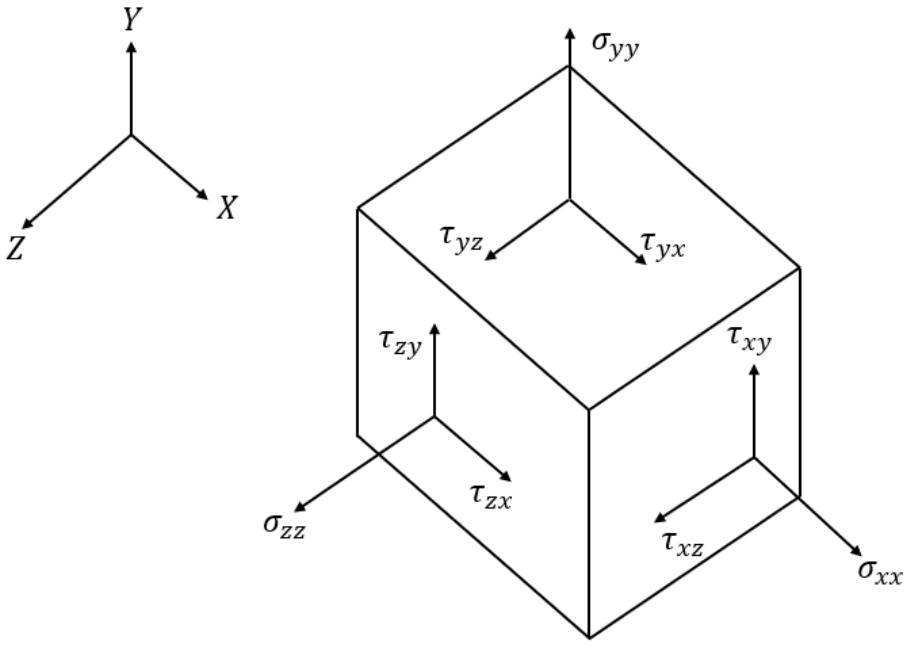

Fig 2.1: Six faces cube for stress demonstration

The six faces of the cube can be termed by the following names, X face, Y face, Z face, negative X face, negative Y face, and negative Z face according to the axis orientation. Let's consider a force F_x acting on the positive X face and due to its three components the developed normal and shear stresses can be respectively denoted by $\sigma_{xx}, \tau_{xy}, \tau_{xz}$. It should be noted that the first subscript in each stress indicates the face direction, and the second subscript indicates the direction of the associated stress. Similarly, for the Positive Y and the Positive Z face the relative stresses are $\sigma_{yy}, \tau_{yx}, \tau_{yz}$ and $\sigma_{zz}, \tau_{zx}, \tau_{zy}$. Moreover, based on the force equilibrium analysis, it can be shown that the shear stresses are symmetric to each other on each axis. Therefore,

$$\tau_{xy} = \tau_{yx}, \tau_{yz} = \tau_{zy}, \tau_{zx} = \tau_{xz}$$

Hence, for a 3D body stress phenomenon, three components of normal and the three components of shear stresses are adequate enough to describe the overall stress condition at a point in a body. Let's write it in a tensor form by the following equation:

$$\{\sigma\} = \{\sigma_x, \sigma_y, \sigma_z, \tau_{xy}, \tau_{yz}, \tau_{zx}\} \quad (2)$$

Note that here normal stress subscript is written as a single subscript instead of a double subscript since they are normal to their associated faces.

Likewise, the strain parameter quantifies the overall deformation of a body as well as the distortion. Similar to the above stress and force equilibrium analysis, it can also be shown

that to evaluate a body's overall strain three normal and shear strain components are fundamentally required and represented in equation (3) in a tensor form.

$$\{\varepsilon\} = \{\varepsilon_x, \varepsilon_y, \varepsilon_z, \gamma_{xy}, \gamma_{yz}, \gamma_{zx}\} \quad (3)$$

wherein ε represents normal strain and γ represents shear strain with associated subscriptions where the first subscript indicates face direction and the second subscript indicates the direction of the strain. In any structural analysis, equation 1-3 demonstrates the response of the structure when it is subjected to a load as well as the associated environment.

These equations are also called the governing equations of the structure. To evaluate structure response under different loading conditions, engineers/researchers need to solve those governing equations. On closer inspection, it seems that the governing equation contains fifteen parameters to capture the structure's overall response under any loading and boundary conditions. Therefore, to solve the governing equations- a set of fifteen equations are needed. To develop necessary additional equations, the engineering mechanics equations and concepts were adopted and implemented here. Based on force equilibrium, the body must satisfy the following equations –

$$\sum F_x = 0, \sum F_y = 0, \sum F_z = 0 \quad (4)$$

By applying stress and body forces in the force equilibrium Eq. (4), it can be written as follows:

$$\frac{\partial \sigma_x}{\partial X} + \frac{\partial \tau_{xy}}{\partial Y} + \frac{\partial \tau_{xz}}{\partial Z} + b_x = 0$$

$$\frac{\partial \tau_{yx}}{\partial X} + \frac{\partial \sigma_y}{\partial Y} + \frac{\partial \tau_{xz}}{\partial Z} + b_y = 0$$

$$\frac{\partial \tau_{zx}}{\partial X} + \frac{\partial \tau_{zy}}{\partial Y} + \frac{\partial \sigma_z}{\partial Z} + b_z = 0$$

(5)

According to the strain-displacement relationship, the normal and shear strain can be written as follows with respect to the displacement:

$$\varepsilon_x = \frac{\partial u_x}{\partial X}, \varepsilon_y = \frac{\partial u_y}{\partial Y}, \varepsilon_z = \frac{\partial u_z}{\partial Z}$$

$$\gamma_{xy} = \frac{\partial u_x}{\partial Y} + \frac{\partial u_y}{\partial X}, \gamma_{yz} = \frac{\partial u_y}{\partial Z} + \frac{\partial u_z}{\partial Y}, \gamma_{zx} = \frac{\partial u_z}{\partial X} + \frac{\partial u_x}{\partial Z}$$

(6)

In engineering analyses, a relationship exists between materials stress and strain. There is no mathematical proof for this relationship. However, based on the experiment as well as practical examples it seems that a linear relationship often exists between stress and strain

in the material, which is known as a famous Hook's law (Law of elasticity). According to Hook's law, within the material elastic limit, the displacement or the deformation size is directly proportional to the deforming force or load. Therefore, the following equation can be derived:

$$\varepsilon_x = \frac{\sigma_x}{E} - \nu\frac{\sigma_y}{E} - \nu\frac{\sigma_z}{E}$$

$$\varepsilon_y = \frac{\sigma_y}{E} - \nu\frac{\sigma_z}{E} - \nu\frac{\sigma_x}{E}$$

$$\varepsilon_z = \frac{\sigma_z}{E} - \nu\frac{\sigma_x}{E} - \nu\frac{\sigma_y}{E}$$

$$\gamma_{xy} = \frac{\tau_{xy}}{G}, \gamma_{yz} = \frac{\tau_{yz}}{G}, \gamma_{zx} = \frac{\tau_{zx}}{G}$$

(7)

Note that, here parameters E ,ν and G represent Young's Modulus, Poisson's ratio, and Shear Modulus, respectively. Equation (7) is purely empirical and handy. It is also well known as a material model, there is an interesting relationship among Young's Modulus, Poisson's ratio, and Shear Modulus which can be written as follow:

$$G = \frac{E}{2(1+\nu)}$$

If two of the parameters are known for a material the third one can be calculated from the above relationship. With the above relation, the requirement for 16 independent equations is reduced to 15 to evaluate structure response under loading conditions. In summary, solving those 15 equations is all about structural mechanics, which are summarized below:

Three equations from force equilibrium:

$$\frac{\partial \sigma_x}{\partial X} + \frac{\partial \tau_{xy}}{\partial Y} + \frac{\partial \tau_{xz}}{\partial Z} + b_x = 0$$

$$\frac{\partial \tau_{yx}}{\partial X} + \frac{\partial \sigma_y}{\partial Y} + \frac{\partial \tau_{xz}}{\partial Z} + b_y = 0$$

$$\frac{\partial \tau_{zx}}{\partial X} + \frac{\partial \tau_{zy}}{\partial Y} + \frac{\partial \sigma_z}{\partial Z} + b_z = 0$$

Six equations based on the strain-displacement relationship:

$$\varepsilon_x = \frac{\partial u_x}{\partial X}, \varepsilon_y = \frac{\partial u_y}{\partial Y}, \varepsilon_z = \frac{\partial u_z}{\partial Z}$$

$$\gamma_{xy} = \frac{\partial u_x}{\partial Y} + \frac{\partial u_y}{\partial X}, \gamma_{yz} = \frac{\partial u_y}{\partial Z} + \frac{\partial u_z}{\partial Y}, \gamma_{zx} = \frac{\partial u_z}{\partial X} + \frac{\partial u_x}{\partial Z}$$

Six relationships based on stress-strain relationships:

$$\varepsilon_x = \frac{\sigma_x}{E} - \nu \frac{\sigma_y}{E} - \nu \frac{\sigma_z}{E}$$

$$\varepsilon_y = \frac{\sigma_y}{E} - \nu \frac{\sigma_z}{E} - \nu \frac{\sigma_x}{E}$$

$$\varepsilon_z = \frac{\sigma_z}{E} - \nu \frac{\sigma_x}{E} - \nu \frac{\sigma_y}{E}$$

$$\gamma_{xy} = \frac{\tau_{xy}}{G}, \gamma_{yz} = \frac{\tau_{yz}}{G}, \gamma_{zx} = \frac{\tau_{zx}}{G}$$

2.3 Structure failure criterion

A structure may fail for different reasons for example it might fail due to static failure, vibration, creep, fatigue, thermal failure, etc. Understanding the fundamental of different failures mechanism is a prerequisite before any structural modeling and analysis. Also, which failure criteria should we check to avoid the structure's ultimate failure? The answer

to this question depends on the structure application, its loading conditions, and the environment. Here, a short overview of different mechanical failures and their criteria have been presented.

2.4 Static failure

In this failure criteria, the structure fails due to the stress which exceeds the material elastic limit. There are two types of major static failures: ductile fracture and brittle fracture. Those failures can be distinguished based on the amount of material plastic deformation before its fracture. For example, in the case of ductile failure, materials experience a significant deformation before the fracture, whereas in the case of brittle failure, materials show minimum deformation. Most metal alloys show ductile failures, whereas ceramics, plastic, and alloy with low plasticity experience brittle failure. It should be noted ductile materials fail mostly for shear stress whereas brittle materials fail due to normal stress. Different theories have been developed to evaluate those failure criteria. Here, several important theories have been discussed further according to their classifications.

(a) Maximum shear stress theory or Tresca Criterion

According to this theory, ductile failure occurs when the maximum shear stress exceeds half of the material's yield strength. It can be written as follows:

$$\tau^{\max} \angle \frac{\sigma_y}{2n}$$

where $\tau^{\max}$, σ_y and n represents maximum shear stress, materials yield strength, and factor of safety of the design, respectively.

(b) Maximum Shear Strain Energy theory or Von-Mises stress

Based on this theory, ductile material fails under loading conditions when maximum von-mises stress is beyond the material yield strength, which means the design is safe when,

$$\sigma^{\max} \angle \frac{\sigma_y}{2n}$$

(c) Maximum Normal Stress theory or Rankine's Theory

According to this theory, brittle material fails whenever the developed maximum normal stress in the structure is greater than the ultimate tensile strength of the material. It can be written as follows:

$$-\frac{\sigma_{uc}}{n} \angle \left\{\sigma_x, \sigma_y, \sigma_z\right\} \angle -\frac{\sigma_{ut}}{n}$$

where $\left\{\sigma_x, \sigma_y, \sigma_z\right\}$ represent maximum principal stresses and $\sigma_{uc,}\sigma_{ut}$ are respectively ultimate compressive strength and ultimate tensile strength, respectively.

(d) Mohr-Coulomb Theory

The Mohr- Coulomb theory is considered a brittle failure based on the comparison where principal stress compares with the ultimate tensile stress and minimum principal stress

compares with the compressive strength of the material. The design safe principal stresses should lie within the hexagonal failure criteria developed by the Mohr-Coulomb theory.

2.5 Buckling failure

Buckling failure occurs due to the present of compressive load in the structure. This type of failure is observed usually in the column, slender like structure, or any structure that undergoes a large compressive load. Buckling failure usually occurs in a stress range which is generally below the material's elastic range. It is directly related to the lateral stiffness of a structure. When the structure is under compressive load its lateral stiffness decreases. With the gradual increase of the compressive load, the lateral stiffness gradually decreases. At a certain compressive load, the structure's lateral stiffness becomes almost zero. At that time even a small increase in compressive force can create catastrophic instability in the structure. The purpose of the buckling analysis is to find the critical compressive load in a structure which generates the buckling failure.

2.6 Fatigue failure

In contrast to static failure, a structure may fail due to dynamic or cyclic loading conditions at a stress level that might be lower than the material yield or ultimate strength of the materials. Fatigue failure occurs in three stages: crack initiation, crank propagation, and failure. There are several theories deployed to measure the fatigue failure of a structure. Among them, Soderberg, Goodman, and Gerber's failure theories are the most famous According to Soderberg's theory, the structure is safe when

$$\frac{\sigma_a}{S_e} + \frac{\sigma_m}{S_Y} \angle \frac{1}{n}$$

where, σ_a and σ_m represent respectively alternating stress and mean stress while S_e and S_Y -represent endurance limit and yield strength, respectively.

Similarly, according to the Goodman theory, the structure is safe when

$$\frac{\sigma_a}{S_e} + \frac{\sigma_m}{S_{ut}} \angle \frac{1}{n}$$

where S_{ut} represents ultimate tensile strength.

On the other hand, Gerber's failure theory state that, the structure is safe when

$$\frac{\sigma_a}{S_e} + (\frac{\sigma_m}{S_{ut}})^2 \angle \frac{1}{n}$$

2.7 Creep failure

The structure is often placed in a high-temperature work environment and exposed to different static loading conditions. The associated deformation and failure due to static loading conditions at an elevated temperature failure are termed creep failure. Several important properties affect the structure/material creep failure including elastic modulus, melting temperature, grain size, etc. For example, a higher melting temperature of material has a greater elastic modulus and a higher resistance against creep.

2.8 Materials Models

In the previous section, governing equation of structure, major mechanical failures, and failure criteria have been discussed extensively. However, there is an important underlying question in numerical modeling: how those physical phenomena are interrelated and predicted mathematically? The answer to this question signifies the importance of the material model. The material model is defined as the mathematical representation of the expected behavior of a material under loading conditions. There are plenty of materials models that have been developed based on the material's unique properties. Among them most widely used material models are the linear elastic model, nonlinear elastic model, viscoelastic model, plastic model, viscoplastic model, and nonlinear materials model, etc. In the elastic model, the material stress is proportional to the strain whereas, in a non-linear elastic model, material stress is not proportional to the strain. It can be easily explained in Fig 2.2, which represents the typical stress vs strain relation for the linear elastic model (a) and non-linear elastic model (b).

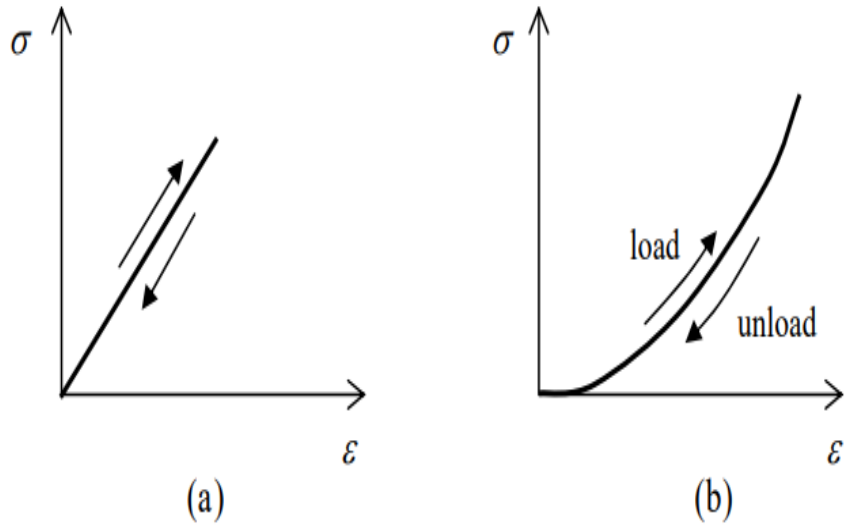

Fig 2.2: Elastic material model: (a) Linear Elastic model and (b) Non-linear elastic model

In engineering analysis, a linear elastic model is heavily used during numerical analysis. It provides the material stress-strain response up to the elastic limit before the fracture point. This model can also be used and worked for any materials when the stress is sufficiently small enough. On the other hand, the non-linear elastic model is useful to evaluate the response of soft materials like tissue, rubber, etc. The plasticity model is used when permanent deformation is particularly important to the structure. The viscoelasticity model is important when the structure works in a high-temperature setup.

2.9 Finite Element Method

The finite element method is well established numerical procedure to solve diverse types of engineering problems from heat transfer, stress analysis, and fluid flow, to electro-magnetism analysis, etc. As we know, governing equations of a system are the

mathematical representation of physical problems, and they are a set of differential equations with initial and boundary conditions. Analytical solutions of those governing equations are often impossible in most practical engineering applications. As a result, numerical approximation/technique plays a pivotal role in solving those complex sets of governing equations. In contrast to the analytical solution that shows the exact behavior of a system at each point, numerical approximation shows solutions only at discrete nodes. The finite element method uses the integral formulations method to create a system of algebraic equations for the governing equations. In addition, a continuous function is deployed to generate the continuous function from the discrete nodal points value. After that, the complete solution is created by connecting or assembling the individual solutions, allowing for continuity at the inter-elemental boundaries.

Note that there are three important phases in any finite element analysis:

1. Processing phase
    (a) Discretize or divide the physical body into many small and geometrically simple bodies (called an element) so that governing equation for each body can be established and solved simultaneously.
    (b) Establish a shape function for the discretized element that approximates the solution of each element.
    (c) Develop relevant algebraic equations for each element.
    (d) Finally, implement boundary, initial, and loading conditions.
2. Solution phase

(a) Solve the set of linear or nonlinear algebraic equations that are derived from the governing equations for each nodal point. For example, in structure analysis displacement value is calculated in each node whereas in heat transfer analysis temperature is calculated.

3. Post-processing Phase

(a) Derive essential information from the problem domain such as maximum principal stress, strain, the factor of safety, heat flux, static and dynamic time-varying electromagnetic field, etc.

In addition to the above-mentioned solution phases, there are several approaches to formulate finite element problems: (1) direct formulation (2) minimum total potential energy formulation (3) weighted residual formulation. FEA solvers selected the formulation types based on the general problem requirements. Commercial FEA solvers adopt mostly weighted residual formulas or minimum total potential energy formulas due to their associated advantages.

2.10 Governing equation for the Structural analysis

The governing equation for structural modeling in any FEA solver can be written as follows:

$$[M]\{\ddot{u}\}+[C]\{\dot{u}\}+[k]\{u\}=\{\mathrm{F}\} \quad \text{..... (7)}$$

where, $[M]$, $[C]$, $\{F\}$ and $[k]$ represents respectively mass matrix, damping matrix, an applied force vector, and global stiffness matrix. Similarly, $\{\ddot{u}\}$, $\{\dot{u}\}$ and $\{u\}$ represents acceleration, velocity, and the nodal displacement vector, respectively. The governing

equation can be viewed as a force equilibrium relation. Equation (7) transformed into different shapes according to the respective analysis. When applied force on the structure F = 0, equation (7) can be written as:

$$[M]\{\ddot{u}\}+[C]\{\dot{u}\}+[k]\{u\}=0 \quad \ldots\ldots(8)$$

Equation (8) is called the governing equation for free vibration or Modal analysis. In this analysis, the structure excited and the respective responses are evaluated without any external force.

On the other hand, when the applied load F is incorporated for a long time and is no longer a function of time, the governing equation of structure can be reduced as the following:

$$[k]\{u\}=\{\mathrm{F}\} \quad \ldots\ldots (9)$$

Equation (9) is called a governing equation for static analysis where the inertia force and damping force effect is negligible.

2.11 Nonlinearity in structural Modeling and analysis

Performing linear structure analysis when the simulation is non-linear in nature often leads ~~you~~ inaccurate and misleading results. Structure engineers should have a firm understanding as well as knowledge of three types of nonlinearities in structural design:

1. Geometric Nonlinearity: It is often associated with the large deflection of the structure under loading conditions. When a structure undergoes large deformations in each step of the load application, the structure must have geometric nonlinearity. Ignoring this large deflection will give inaccurate results as well as estimations about the structure's overall

safety. Therefore, in analysis, incorporation of the large deflection in each step will help to solve the geometric nonlinearity.

2. Topology Nonlinearity: This sort of nonlinearity is related to the topological change of the structure. For example, a change of contact status may cause an abrupt change in materials stiffness when bodies come into or out of contact with each other. Special consideration should be adopted during the structure design as well as boundary conditions.

4. Material Nonlinearity: When materials' stress-strain relationship is nonlinear in nature then this type of nonlinearity comes to light. In linear analysis, the material is considered by default as a linear material. Thus, performing linear analysis by using nonlinear materials is misleading and inaccurate. If the material is nonlinear then selecting models to solve the analysis is another area of expertise. The most widely used models to solve the nonlinear materials are the elastoplastic material model, the perfect plastic material model, the visco-elastic material model, and the nonlinear elastic material model, etc.

2.12 Mesh and Mesh Quality

There are two major steps in a finite element method analysis: (1) establish a governing equation and (2) solve the governing equation. In the real world, the problem geometry is complex, and setting up the governing equation for the complex geometry is often impossible. As a result, the geometry is divided into finite-size elements and then the

governing equation can be easily set up for the simple element. This element is called a grid or mesh. Each element is connected with the surrounding element by nodes. The accuracy of any finite element method result highly depends on the mesh/grid type as well as grid quality. Poor grid quality often provides inaccurate results or fails to converge the numerical simulation. In finite element analysis, several types of grids have been developed with these associated pros and cons.

For two-dimensional geometry, the following mesh elements are used in finite element analysis

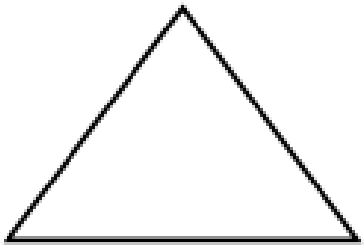

Triangle

Quadrilateral

For three-dimensional geometry, the following mesh elements are usually used in finite element analysis:

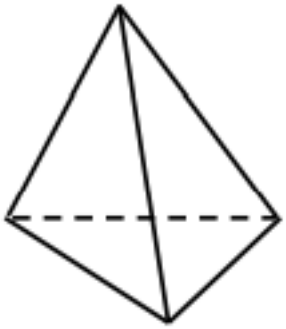

Tetrahedron

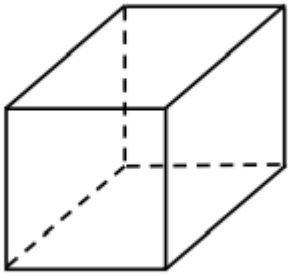

Hexahedron

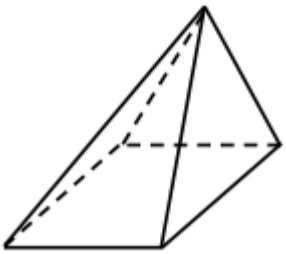

Pyramid

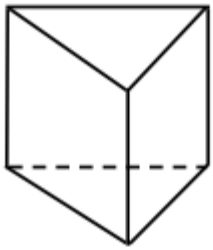

Wedge

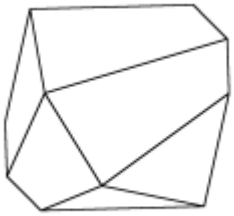

Polyhydron

Each mesh element has unique pros and cons. For example, when the geometry is complex and big tetrahedron mesh has the advantage to discretize the geometry more than the hexahedron mesh type. However, hexahedron mesh is computationally efficient and easily converges compared with tetrahedron mesh. It is often a good practice to use a combination of mesh types in geometry for efficient mesh type and quality results.

Along with mesh type selection, mesh quality is one of the critical steps for numerical simulation. Numerical model accuracy is highly dependent on the generated mesh quality. A poor-quality mesh will create inaccurate solutions or slow convergence. There are several mesh-quality parameters available to quantify the quality of the generated mesh. The most commonly used and accepted mesh quality parameters are Orthogonal quality and skewness.

According to the meshing guidelines, the mesh orthogonal quality should be as maximum as possible whereas the skewness mesh matric quality should be as minimum as possible.

Orthogonal Quality mesh metrics spectrum

Unacceptable	Bad	Acceptable	Good	Very good	Excellent
0-0.001	0.001-0.14	0.15-0.20	0.20-0.69	0.70-0.95	0.95-1.00

Skewness mesh metrics spectrum

Excellent	Very good	Good	Acceptable	Bad	Unacceptable
0-0.25	0.25-0.50	0.50-0.80	0.80-0.94	0.95-0.97	0.98-1.00

Chapter 3

3 Dynamic load analysis in Reciprocating driver

3.1 Background

The objective of this chapter is to determine dynamic loads acting on the crankshaft reciprocating driver system during its operation. Then, the dynamic loads from the dynamic analysis will be deployed in the structural design studies since handling these dynamic loads is the primary goal for the reciprocating driver for its successful operation. Note that for critical operation of the RA aircraft, the crankshaft must withstand several loading conditions. In other words, the present dynamic analysis will facilitate the necessary boundary conditions in the structural design and analysis. There are several ways a dynamic analysis can be performed: analytical method, rigid body dynamics analysis/motion study, or a combination of both. To ensure the analysis accuracy, the present study deal with both study approaches. At first, the study performs an analytical study and after that, it will perform the rigid body dynamic simulation. Finally, based on the analysis results, a constructed comparison will be presented between analytical and rigid body dynamic simulation results. It should be noted that the rigid body dynamic analysis is a transient simulation in nature.

3.2 Analytical approach

To perform the analytical study, a slider-crank mechanism approach has been adopted and implemented, where a wing assembly is replaced by a slider. Fig. 3.1 represents a sample slider crank mechanism and sample velocity diagram for the analysis. To calculate the

necessary reaction forces, the necessary diagram in terms of velocity, force, and acceleration has been developed and analyzed carefully.

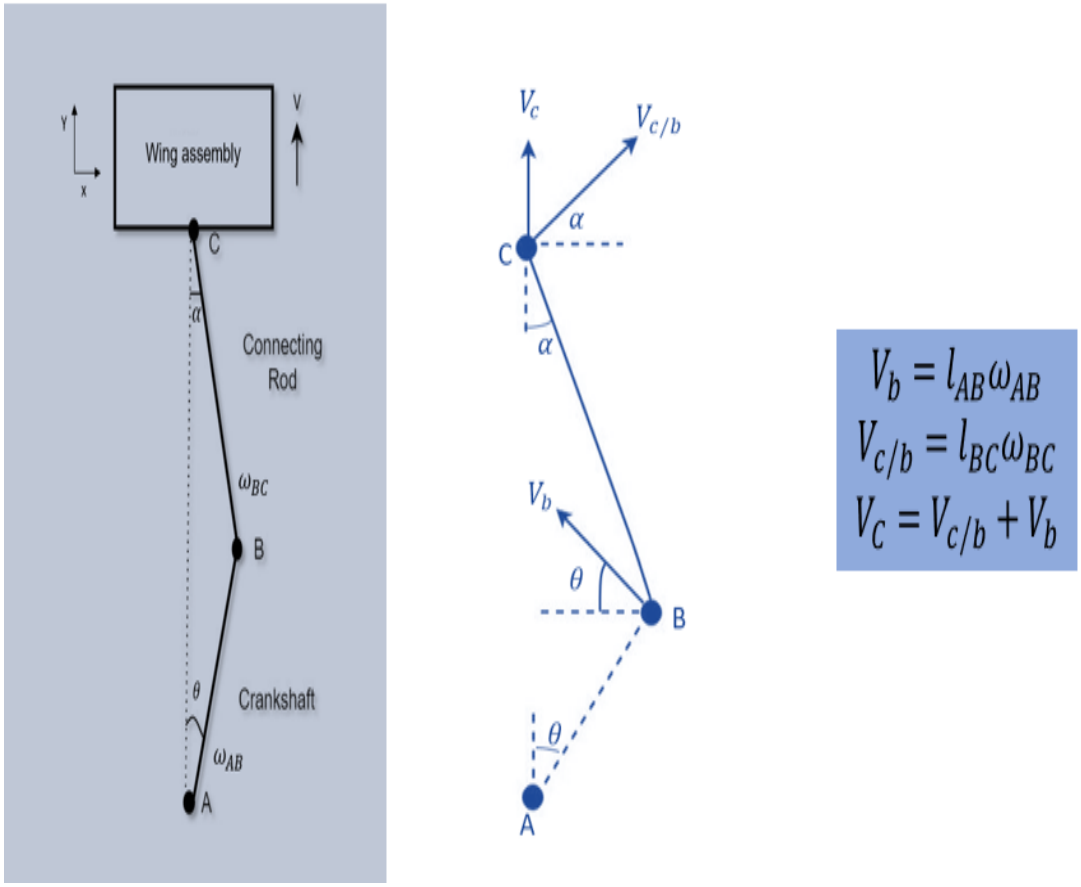

Fig. 3.1: Slider-crank mechanism and a sample velocity diagram.

Section AB

$V_A = 0$ m/s since its fixed. Therefore,

$$V_{\frac{B}{A}} = V_B - V_A$$

$$V_{\frac{B}{A}} = V_B$$

Where $V_B = l_{AB}\omega_{AB}$

Similarly, for section BC:

$$V_{\frac{C}{B}} = l_{BC}\omega_{BC}$$

$$V_{\frac{C}{B}} = V_C - V_B$$

$$V_C = V_{\frac{C}{B}} + V_B$$

It should be noted that here $V_{\frac{B}{A}}$ represents Velocity at B with respect to point A and $V_{\frac{C}{B}}$ represents Velocity at C with respect to point A.

X-comp:

$$V_{\frac{C}{x}} = V_{\frac{C}{B}} + V_{Bx}$$

$$0 = l_{BC}\omega_{BC}\cos(\alpha) + V_B\cos(\theta)$$

$$\omega_{BC} = -\frac{V_B\cos(\theta)}{l_{BC}\cos(\alpha)}$$

Y comp:

$$V_{cy} = l_{BC}\omega_{BC}\sin(\alpha) + V_B\sin(\theta)$$
$$= V_B\sin(\theta) - V_B\cos(\theta)\tan(\alpha)$$
$$= V_B\sin(\theta) - V_B\cos(\theta)\tan[\sin^{-1}(\frac{\sin(\theta)}{l_{BC}})]$$

$$\mathrm{V}_C = l_{AB}\omega_{AB}[\sin(\theta) + \frac{l_{AB}\sin(2\theta)}{2l_{BC}}]$$

Velocity,

Acceleration,

$$\mathrm{a}_C = \frac{dV_C}{d\theta} = l_{AB}\omega_{AB}[\frac{d}{d\theta}\sin(\theta) + \frac{l_{AB}}{2l_{BC}}\frac{d}{d\theta}\sin(2\theta)]$$

$$\mathrm{a}_C = l_{AB}\omega_{AB}{}^2[\cos(\theta) + \frac{l_{AB}}{l_{BC}}\frac{d}{d\theta}\cos(2\theta)]$$

Displacement,

$$\mathrm{x} = (l_{AB} + l_{BC}) - (l_{AB}\cos(\theta) + l_{BC}\cos(\alpha))$$
$$= l_{AB}(1-\cos(\theta)) + l_{BC}(1-\cos(\alpha))$$
$$= l_{AB}(1-\cos(\theta)) + l_{BC}[(\frac{l_{AB}}{l_{BC}})^2\frac{\sin(\theta)^2}{2}]$$

Slider side

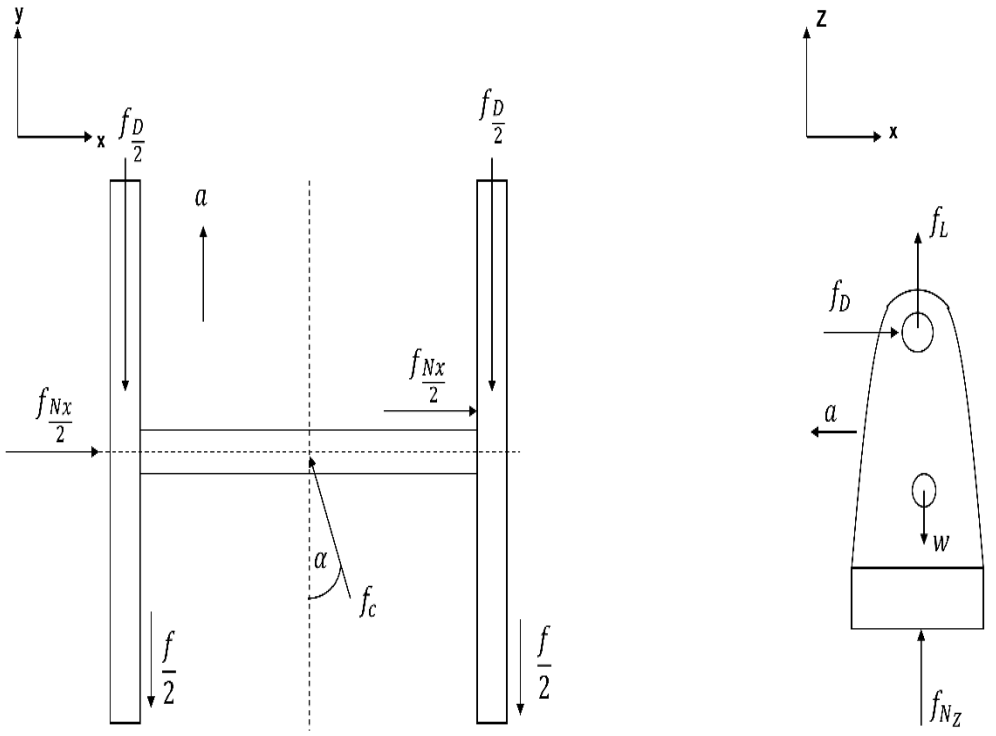

X-comp:

$$\sum f_x = f_{N_x} - f_{C_x} = 0$$

$$f_{N_x} = f_{C_x}$$

$$f_{N_x} = f_C \sin(\alpha) = f_C (\frac{l_{AB}}{l_{BC}}) \sin(\theta)$$

…….. (1)

Y-comp:

$$\sum f_y = f_{cy} - f_D - f = ma_c$$

$$f_C \cos(\alpha) = f_D + f + ma_c$$

$$fc = \frac{f_D + f + ma_c}{\cos(\alpha)}$$

$$fc = (f_D + f + ma_c)[1 - (\frac{l_{AB}}{l_{BC}})^2 \sin^2(\theta)]^{-\frac{1}{2}}$$

……(2)

Eq. (2) + Eq. (1):

$$f_{Nx} = (f_D + f + ma_c)[1 - (\frac{l_{AB}}{l_{BC}})^2 \sin^2(\theta)]^{-\frac{1}{2}} (\frac{l_{AB}}{l_{BC}}) \sin(\theta)$$

$$\tan(\alpha) = [1 - (\frac{l_{AB}}{l_{BC}})^2 \sin^2(\theta)]^{-\frac{1}{2}} (\frac{l_{AB}}{l_{BC}}) \sin(\theta)$$

Where

Connecting Rod side

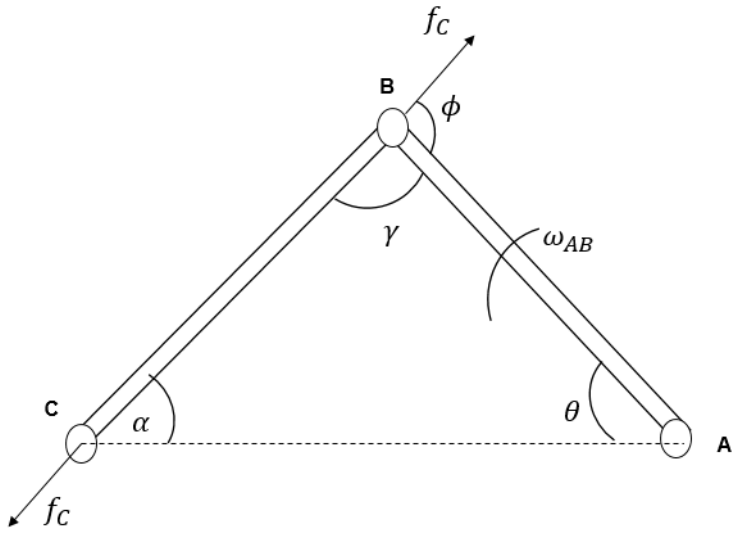

$$180 = \gamma + \theta + \alpha$$

$$\phi = \theta + \alpha$$

$$f_T = f_c \sin(\phi) = f_c \sin(\theta + \alpha)$$

$$f_R = f_c \cos(\phi) = f_c \cos(\theta + \alpha)$$

The moment on A:

$$\mathrm{M}_A = l_{AB} f_T = l_{AB} f_C \sin(\theta + \alpha)$$

When the crankshaft frequency is 12.5 Hz

$$\omega_{AB} = 2\pi f = 750 rad/\mathrm{m}$$

Load on slider when total mass is 40 kg, crank radius 1 meter, and connecting rod length 2.76 meter-

$$fc = (f_D + f + ma_c)[1-(\frac{l_{AB}}{l_{BC}})^2 \sin^2(\theta)]^{-\frac{1}{2}}$$

$$fc = ma_c[1-(\frac{l_{AB}}{l_{BC}})^2 \sin^2(\theta)]^{-\frac{1}{2}}$$

$$\mathrm{a}_C = l_{AB}\omega_{AB}{}^2[\cos(\theta) + \frac{l_{AB}}{l_{BC}}\frac{d}{d\theta}\cos(2\theta)]$$

During tension, maximum acceleration is:

$$(\mathrm{a}_C)_{T,\max} = -1*\omega_{AB}{}^2[\cos(0) + \frac{1}{2.76}\cos(2.0)]$$

$$= -8403.468\frac{m}{s^2}$$

During compression, maximum acceleration is:

$$(\mathrm{a}_C)_{\mathrm{C,max}} = -1*\omega_{AB}{}^2[\cos(0.74\pi) + \frac{1}{2.76}\cos(2.0\times 0.74\pi)]$$

$$= 4363.098\frac{m}{s^2}$$

The maximum force acting on the slider during tension

$$(fc)_{Tension} = (40)\times(-8403.468)[1-(\frac{1}{2.76})^2 \sin^2(0)]^{-\frac{1}{2}}$$

$$= -336138N$$

The maximum force acting on the slider during compression

$$(fc)_{Compressio} = (40)\times(4363.098)[1-(\frac{1}{2.76})^2 \sin^2(0.74\pi)]^{-\frac{1}{2}}$$

$$= -180857N$$

Crankshaft side

$$(f_T)_{T=}(fc)_{Compression}\sin(\theta+\alpha)$$

$$= (-336138)\sin(0+0)$$

$$= 0\ \mathrm{N}$$

Reaction force acting in the crankshaft during maximum tension

$$(f_R)_{T=}(fc)_{Tension}\cos(\theta+\alpha)$$

$$=(-336138)\cos(0+0)$$

$$= -336138\ \mathrm{N}$$

Moment

$$M_A = l_{AB}(fc)_{Tension}\sin(\theta+\alpha)$$

$$=(1)(-336138)\sin(0+0)$$

$$= 0Nm$$

Reaction force acting in the crankshaft during maximum compression

$$(f_R)_{c=}(fc)_{Compression}\cos(\theta+\alpha)$$

$$=(180857)\cos(0.74\pi+0.2654)$$

$$= -154731\ \mathrm{N}$$

Moment

$$M_A = l_{AB}(fc)_{compression} \sin(\theta + \alpha)$$

$$=(1)(180857)\sin(0.74\pi+0.2654)$$

$$= 93634\,Nm$$

Therefore, based on the analytical result, it seems that the maximum tension and compression forces developed in the crankshaft driver are respectively 336 KN and 155 KN.

3.3 Dynamic Approach

A rigid body dynamic model has been developed to calculate the necessary reaction force, velocity, and acceleration of the reciprocating driver with the help of FEA. The purpose of the Rigid body dynamics analysis is to study the movement of the individual components in a system which usually provides the foundation for different engineering analyses. To perform our reciprocating driver rigid body dynamics analysis, Ansys rigid body dynamic module has been employed whereas for the driver assembly CAD model was developed in the design software SOLIDWORKS. Note that the simulation module is transient in nature. During the analysis, the reciprocating driver crankshaft rotates at different angular speeds along with the original operational speed (750 rev/min or 78 rad/s), and the response for each individual speed is carefully analyzed as well as discussed further. The ultimate goal of this FEA-based rigid body dynamic analysis is to approximate the different resultant forces of the underlying system. Note that, rigid body dynamic analysis also facilitates different boundary conditions (Velocity, acceleration, moment, force, etc.) and those boundary conditions can be implemented in different structural design and development

analyses. Also, it should be noted that the numerical study results from the rigid body dynamic analysis will be compared with the analytical result that ultimately provides the ground to use rigid body dynamic analysis further. Fig. 3.2 represents a crankshaft reciprocating driver assembly CAD model that has been used in the rigid body dynamic analysis. Table 3.1 represents the assembly details for the rigid body dynamic analysis.

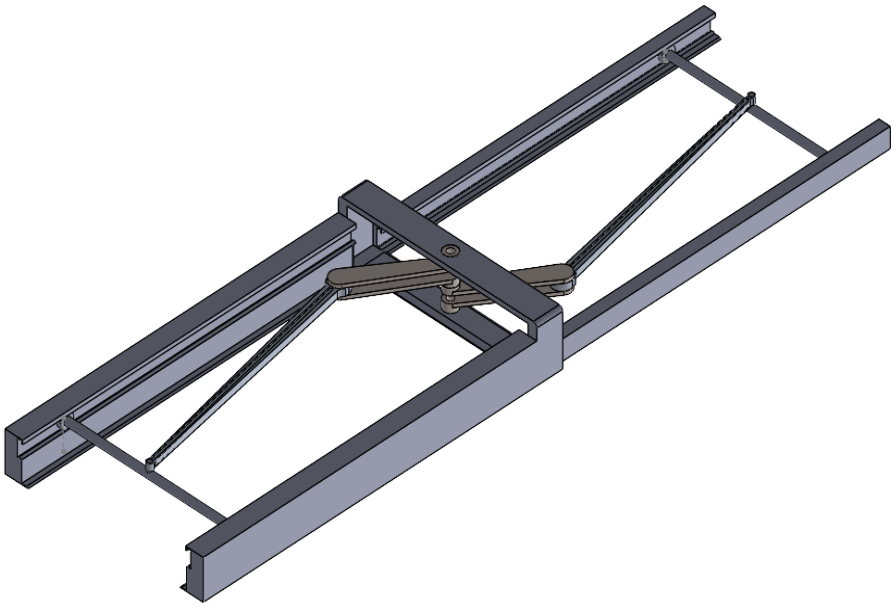

Fig 3.2: Reciprocating assembly driver for rigid body dynamics analysis.

Table 3.1: Details of the assembly used in the rigid body dynamic analysis.

Component	Mass (kg)
Crankshaft	55
Connecting rod	14

Slider (Wing+ driver + other)	40

Rigid body dynamics analysis has been performed for different crankshaft angular velocities: 600 rev/min, 650 rev/min, 700 rev/min, and 750 rev/min. The actual angular velocity of the reciprocating driver is 750 rev/min. For different angular velocities, the necessary reaction forces in the X-direction, Y-direction, Z-direction, and the total resultant force were evaluated and presented in Figures 3.2 to 3.6. The resultant force in the Z-direction is very small and hence, negligible. Figure 3.3 represent the resulting force in the X-direction and Y-direction and the total force acting on the connecting rod when the angular velocity of the crankshaft is 600 rev/min, where the maximum total resultant tensile force developed is around 204 kN with a compressive force of 106 kN.

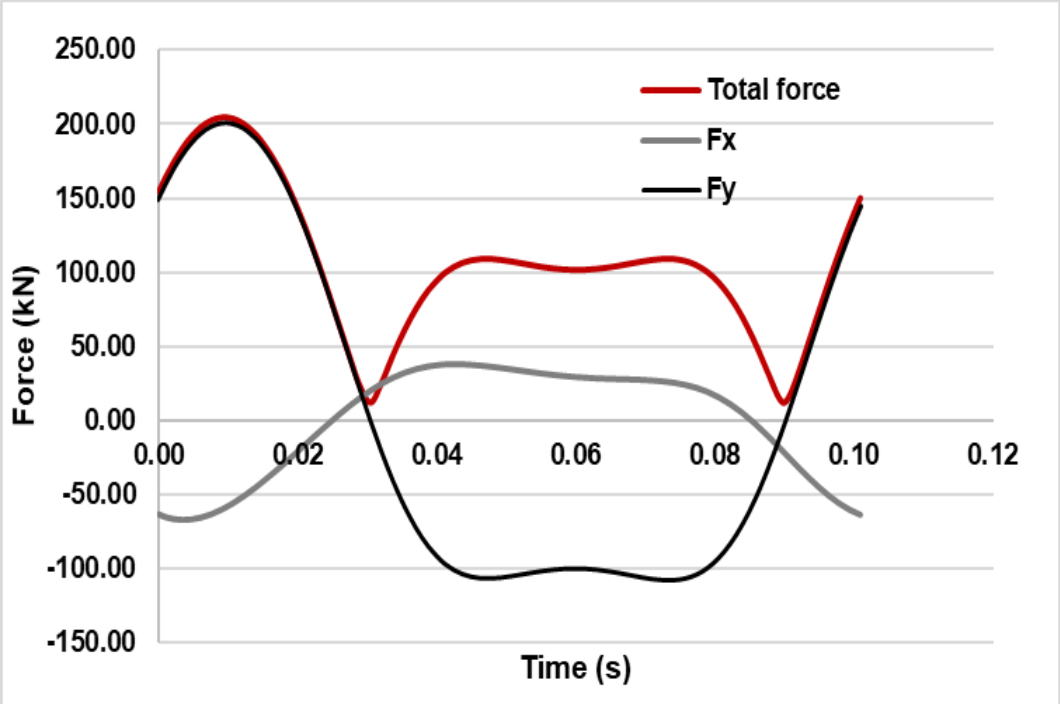

Fig 3.3: Different force at the junction between the slider and connecting rod when crankshaft rotational speed is 600 rev/min.

Similarly, the different forces for crankshaft speed 650 rev/min are presented in fig 3.4 whereas figure 3.5 represent the result for crankshaft speed 700 rev/min.

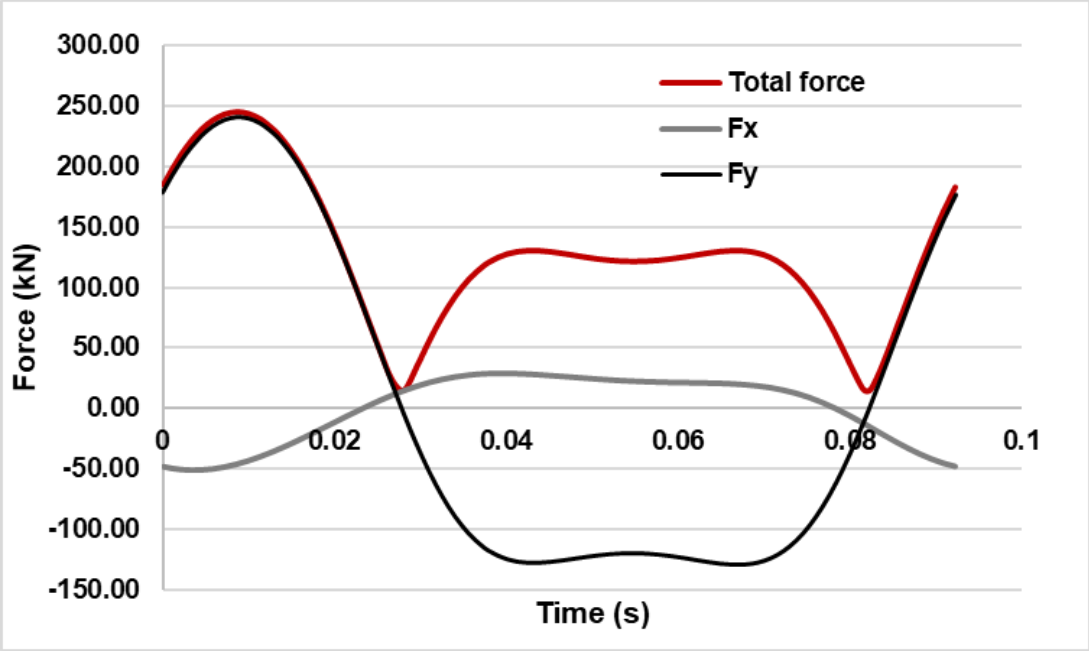

Fig 3.4: Different force at the junction between the slider and connecting rod when crankshaft rotational speed is 650 rev/min.

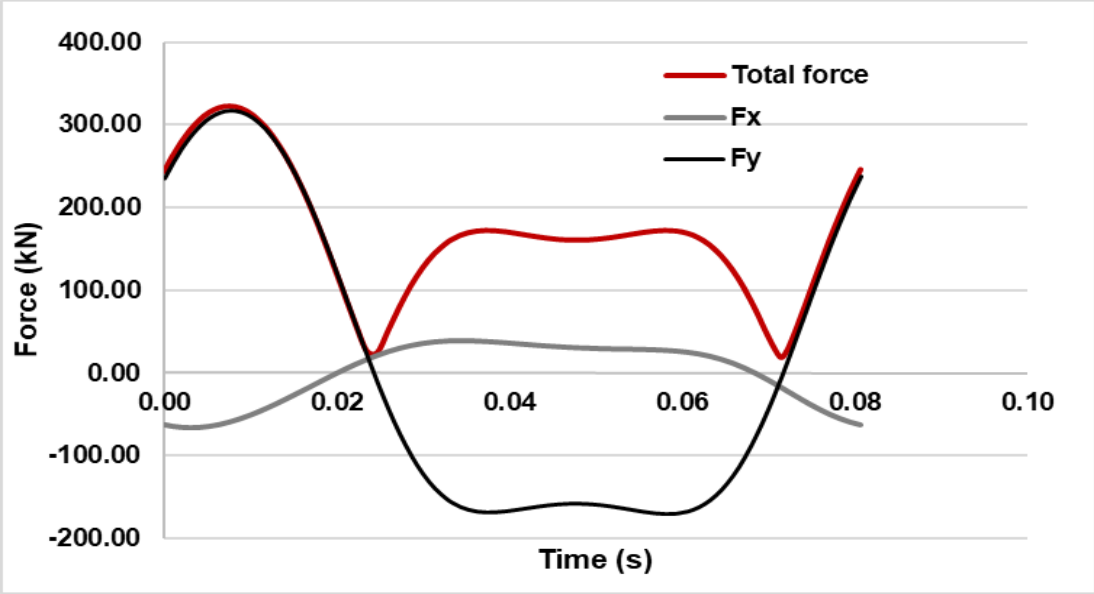

Fig 3.5: Different force at the junction between the slider and connecting rod when crankshaft rotational speed is 700 rev/min.

Since the actual working speed of the crankshaft during operation is 750 rev/min. The rigid body dynamics analysis has also been performed for the actual operating condition and the resultant force has been plotted and compared with the analytical result with respect to crankshaft angular speed. The maximum tensile force developed in the rigid body dynamic analysis was 336.134 kN whereas the maximum compressive force developed at 176 kN. In analytical analysis, the maximum tensile force developed was 336.138 kN, and the maximum compressive force developed was 154.731kN. It seems that the tension force value in both studies is almost the same whereas the compressive force has a difference. Figure 3.6 presents a more detailed comparison between analytical and rigid body dynamic analysis (Motion Study) results. It can be clearly seen from Figure 3.6 that the motion study (rigid body dynamic analysis) result is well agreed with the analytical result. Therefore, rigid body dynamic analysis can be further implemented and used in future studies

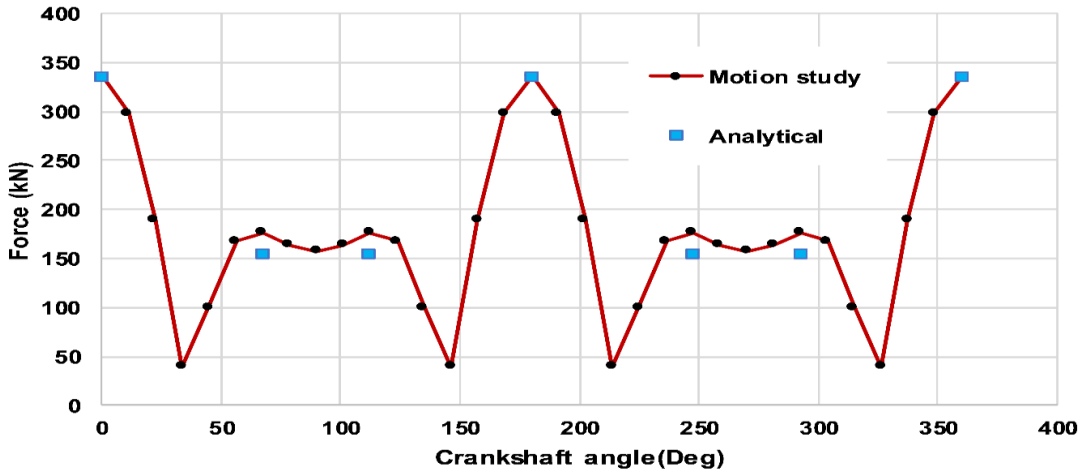

Fig. 3.6: Variation of the reaction force magnitude on the crank pin over one complete cycle with a crankshaft speed of 750 rev/min and a wing assembly weight of 40 kg.

CHAPTER 3

4 Crankshaft Design

4.1 Background

The crankshaft system is widely used to perform the conversion between rotary and reciprocating motions. It is considered the backbone of an internal combustion engine and usually worked with connecting rods. Because of the complex loading circumstances and strict standards, designing and developing a crankshaft has always been a critical challenge for automobile industries in order to meet cheap prices, minimum weight, enough strength, and other functional requirements. Crankshaft design and development are commonly practiced in several ways: Experimentally, analytical and numerical procedures. Earlier, the crankshaft has been designed and developed based on some empirical formulas and experimental tests [59,60]. However, design based on empirical always leads to compromised design or overdesigned crankshaft which directly impacts the economy of the associated system. Continuous development of the Finite element method and computing capacity facilitates robust FEA-based crankshaft design which is now become a dominant crankshaft design approach. FEA facilitates the easy and inexpensive study of random pairs of input parameters along with the design and manufacturing requirements. Numerous successful designs have been developed and deployed on the markets by using the finite element analysis technique [61–64].

In the novel Vertical takeoff and landing technology, the crankshaft has considered the critical component for the reciprocating driver. It will produce a long-stroke reciprocation motion for the wings from which RA aircraft will generate the necessary lift. The objective

of this study is to model a crankshaft to structurally determine the feasibility of using a crankshaft as the reciprocating driver of the new VTOL technology. The reciprocating driver is a critical component of the VTOL technology to produce the long-stroke reciprocating motion of the two wings in an RA aircraft to generate lift for takeoff. The two wings reciprocate simultaneously with the same velocity magnitude, but in opposite directions so that the inertia forces and moments associated with both wings will be canceled. The conventional crankshaft system is inappropriate in this application because the current system requires a large crank radius, long connecting rods, and a small weight while handling large inertia forces simultaneously. Preliminary studies have already shown that the traditional crankshaft failed to meet the present technology requirements. The crankshaft driver development is considered to be one of the most important and challenging steps toward the successful demonstration of new aircraft applications. Although the crankshaft driver is coupled with the two reciprocating wings, as the first step, this study concentrates on the crankshaft only.

4.2 Model design and Boundary Conditions

One of the goals of this research is to model a crankshaft that has enough crank radius so that it can provide enough stroke simultaneously for the two reciprocating wings in back and forth motion. The long reciprocating stroke is critical for the wings to generate sufficient lift during the takeoff and landing of the aircraft. Our present aircraft design requires the crankshaft radius to be one meter and the total weight of the crankshaft less than 55 kg. Also, since each crank would drive one of the two wings, the distance between

the two crank webs is minimized to maintain the two wings at almost the same elevation. Figure 3.1 shows a SolidWorks design of the crankshaft and its necessary dimensions.

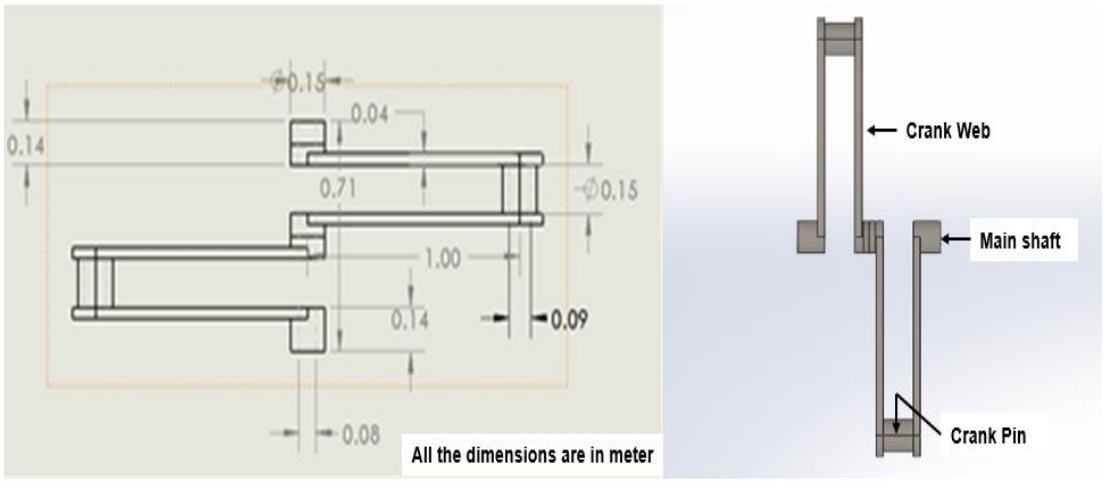

Fig. 3.1: Drawing and SolidWorks designed crankshaft with specified dimensions.

In an internal combustion engine, there are two types of loads acting on the crankshaft, a combustion load (dominant force) and a dynamic load due to the nature of the mechanism. The crankshaft of the present aircraft application does not subject to combustion load but subject to very strong dynamic loads associated with the inertia force due to the reciprocating motion of the two wings and connecting rods.

Based on the rigid body dynamics and analytical analysis, the maximum tensile and compressive inertia forces developed are, respectively, 336 kN and 175 kN when the operating angular velocity of the crankshaft is 750 rpm. As a result, the designed crankshaft must withstand this large inertia force along with the other specified conditions. In the analysis, a range of applied loads are incorporated on the crankshaft and their respective effects are carefully analyzed. The compressive load varies from 170 to 180 kN whereas the tensile load varies from 330 to 340 kN. Figure 3.2 shows a sample tensile boundary

condition setup for the present numerical analysis [65]. The effect of gravitational force is also considered.

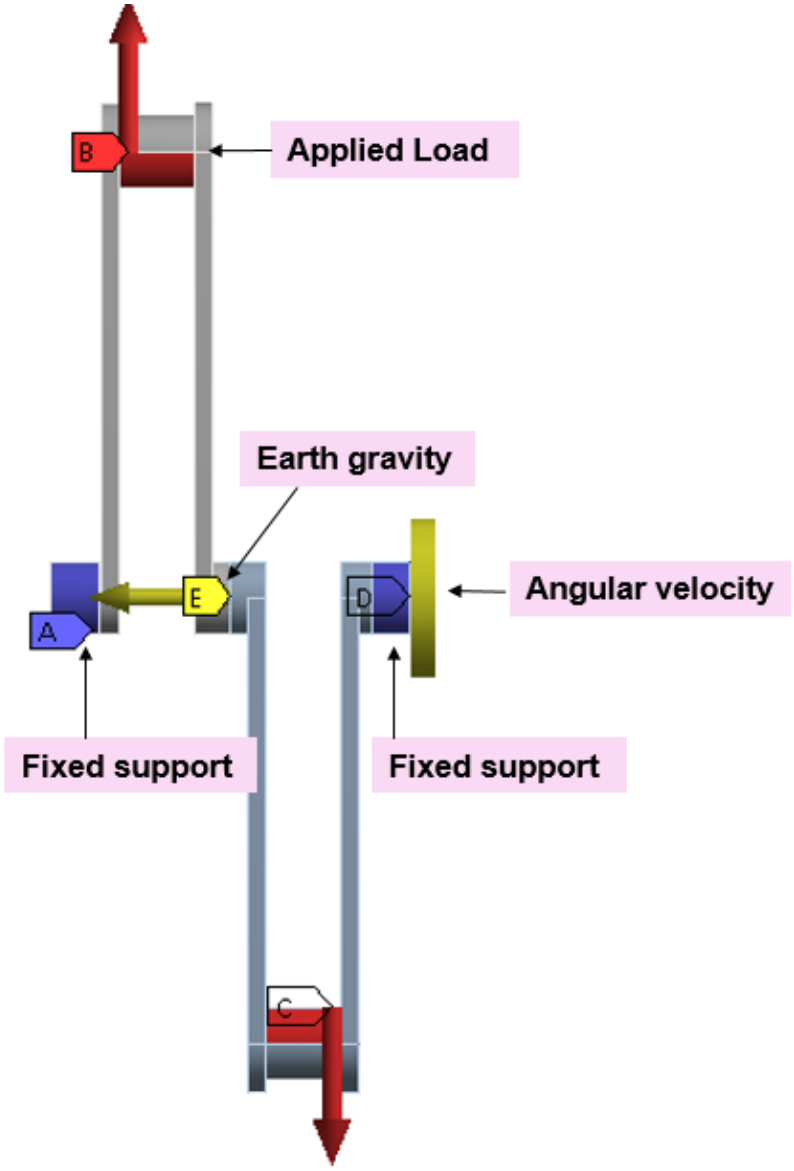

Fig. 3.2: A sample tensile boundary condition setup for static structural analysis.

4.3 Material selection

Crankshaft material selection is a critical requirement in this study. One of the primary design requirements of the crankshaft is weight minimization so that it will not pose a

significant penalty on the aircraft's total lifting capacity. Also, safety is another highest priority in the design. Therefore, the selected crankshaft material should have sufficient strength to withstand the dynamic load of the wings. In an earlier study, traditional crankshaft materials including forged steel, cast iron, and high strength steel alloys were selected and studied for the present applications but they failed to meet the design requirements. Although they have acceptable strength to withstand the load, the excessive weight due to their high mass density made them inappropriate for our application. As a result, it was concluded that new materials should be used so that they could meet our prime requirements: small weight and high strength.

To find suitable materials for the crankshaft, commercial software Granta's, C. E. S. 2007 has been employed [66]. Based on the materials research result, several materials appear suitable for our applications. Among them, high-strength carbon fiber composite was selected due to its low weight and higher strength. The designation of the selected composite material is termed as Bismaleimide+High Strength Carbon fiber composite. It is the family of thermoset (cross-linked) polyimides of which the simplest member has a formula (CH2(C6H4N(CO)2C2H2), where matrix material and filler/reinforcement material are respectively Bis-Maleimide (BMF-CF65) and carbon fiber. The filler/reinforcement material represents a 60-70 % portion of the total composite weight. Carbon fiber composites have been extensively used in many aerospace-related applications, such as high-speed flight controls, engine inlets, missile components, and aerospace components where elevated-temperature performance is required. Another example is a new Carbon Fiber V12 engine being built by the automobile company

Lamborghini [67,68]. Table 3.1 presents some important mechanical properties of the high-strength carbon fiber.

Table 4.1: Mechanical properties of High strength carbon fiber [66].

Properties	Value	Unit
Density	0.0567-0.0582	lb/in^3
Young's Modulus	$15.9-18.9\times10^6$	psi
Yield Strength	248-252	ksi
Tensile Strength	248-252	ksi
Compressive Strength	175-194	ksi
Flexural Strength (Modulus of rupture)	248-252	ksi
Poisson's ratio	0.3-0.335	
Hardness-Vickers	21.6-47.4	HV
Unit price	43.4-52.1	Usd/lb

4.4 Grid Independent Test and Validation of the FEA

The commercial Ansys Mechanical Solver was used to perform finite element analyses, and the tetrahedral grid was selected to discretize the computational domain (see Fig. 3.3). The grid can easily combine with curvature and proximity, and also the software has the feature of automatically refine the mesh in critical regions. Moreover, it is quick, automatic, and advantageous for complicated geometries. The grid independence test was performed

by varying the number of grids from 0.08 to 1.07 million. The final number of 0.53 million control volumes was selected, at which the grid independence is reached. Figure 3.4 shows the grid-independence test results in terms of the change of total deformation with respect to grid numbers. It is evident from the figure that the percentage change of total deformation becomes insignificant after 0.53 million grid numbers for the present analysis. The grid independence test is a widely practiced approach to maintaining simulation accuracy in numerical fields [69,70].

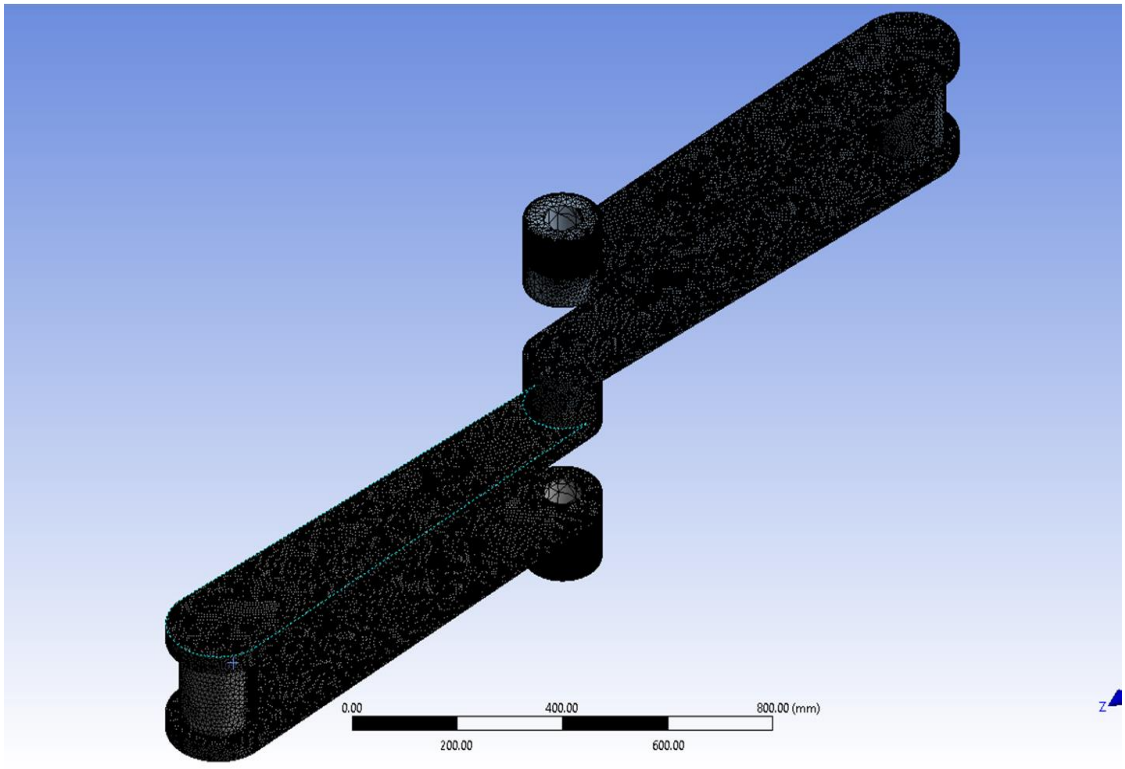

Fig. 3.3: Mesh view of the crankshaft model

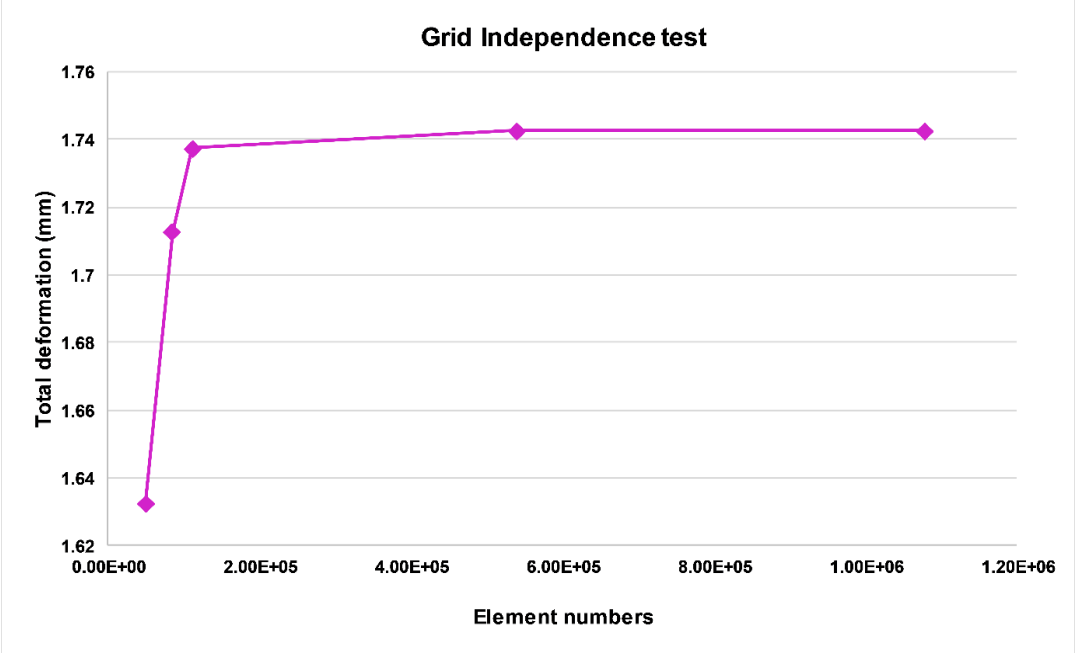

Fig. 3.4: Grid independent test results.

To validate our numerical analysis, the crankshaft developed by Montazersadgh and Fatemi [20] was modeled in our workflow and the results were derived based on the authors' boundary conditions. The study was selected to validate our workflow because it contains experimental, numerical, and analytical results. In their numerical analysis, Abaqus commercial solver has been employed. Therefore, the present validation also provides a constructive comparison between two advanced commercial solvers, Ansys and Abaqus. Table 3.2 presents the Ansys results in terms of stress calculated in two locations (Locations a and b) and the comparison with those of the Abaqus and analytical results. It appears that our result agreed well with both the experimental and numerical results. It is also seen that the Ansys and Abaqus results are almost identical!

Table 4.2: Validation results and comparison with those of Montazersadgh and Fatemi [20].

Load (N)	Location a					Location b				
	Exp. (MPa)	Ansys (MPa)	Diff. % *	Abaqus (MPa)	Anal. (MPa)	Exp. (MPa)	Ansys (MPa)	Diff. % *	Abaqus (MPa)	Anal. (MPa)
-890	-59.3	-61.1	2.94	-61.6	-72	81.4	87.2	6.65	86.9	72
890	65.5	61.2	7.03	61.5	72	-90.3	-87.4	3.31	-86.7	-72

***** Diff.: Percetage difference between the Ansys and experimental results/Anal.: The analytical results of Montazersadgh and Fatemi.

4.5 Result and Discussion

FEM analyses were performed for a range of compressive and tensile loading conditions on the modeled crankshaft to determine the responsive stress conditions. In the analysis, the compressive loads vary from 170 to 180 kN with 5 kN increments while the tensile loads changed from 330 kN to 340 kN. For each loading condition, the crankshaft response was observed and calculated by using different safety tools.

4.6 Effect of Compression Load

In the first step of the analysis, three different compressive loads (170, 175, and 180 kN) were imposed at the crankpin section, and then the response was analyzed and measured by using safety tools. Figure 3.5 shows the total deformation plot for each compressive loading case. The maximum deformation developed is about 1.836 mm for the 180 kN loading case. It seems that all the deformations are small or negligible. It can also be seen

that the two middle crank webs experienced comparatively higher deformation than the upper and lower crank webs.

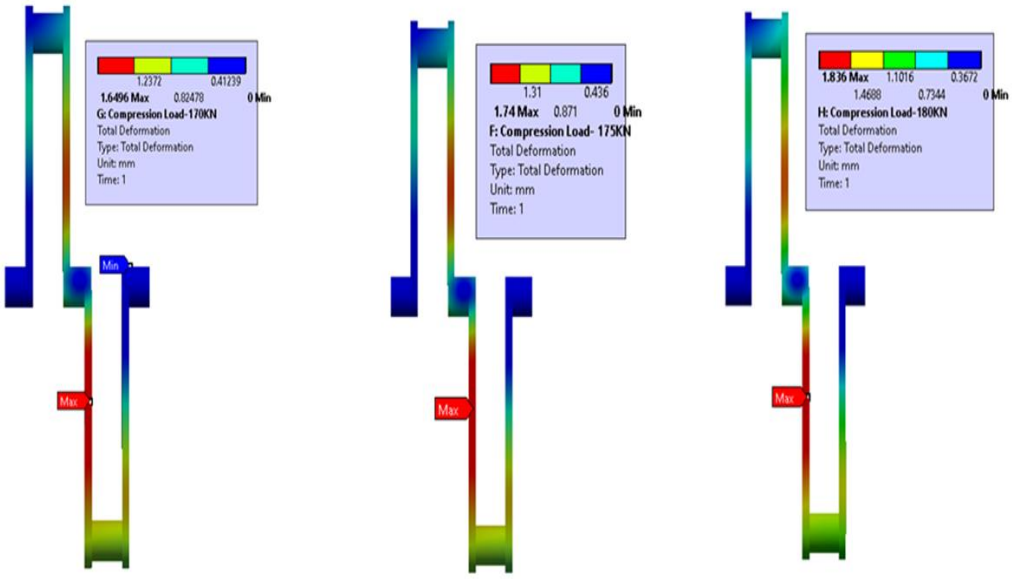

Fig. 3.5: Total deformation plots for compressive loads of 170, 175, and 180 kN.

Similarly, to evaluate the stress response of the crankshaft, von-Mises stress and maximum principal stress theory has been employed. Figure 3.6-3.8 represent Von-Mises stress contour plots for different compressive loads.

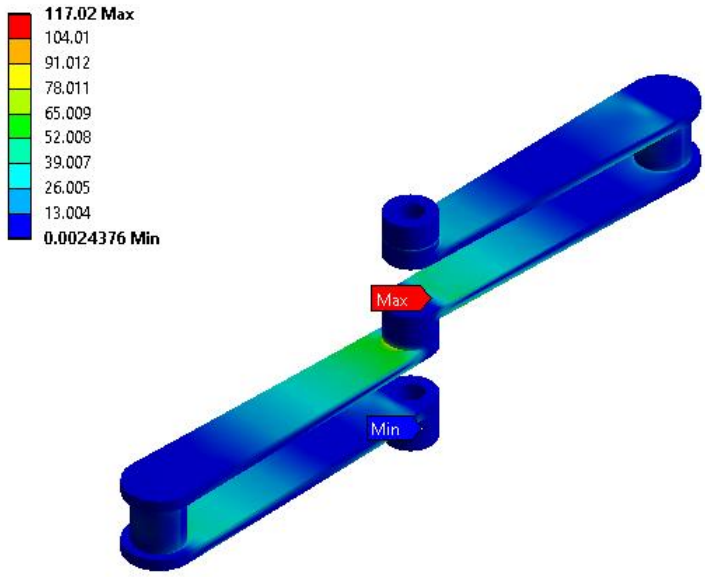

Fig 3.6 : Von-Mises stress contour plot for the compressive load 170 kN.

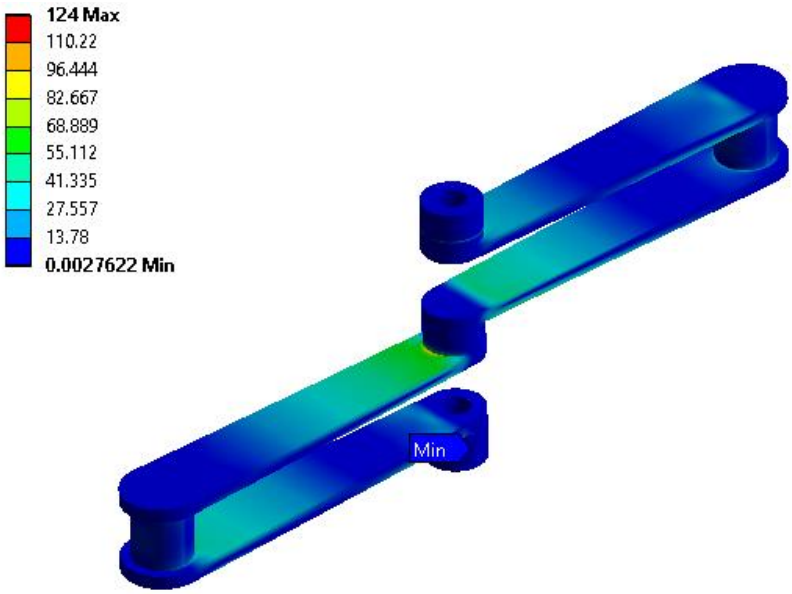

Fig 3.7: Von-Mises stress contour plot for the compressive load 175 kN.

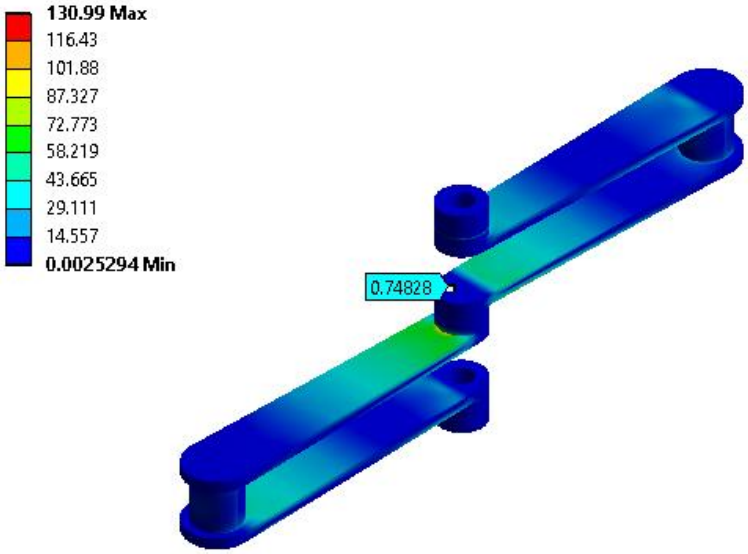

Fig 3.8: Von-Mises stress contour plot for the compressive load 180 kN.

Figure 3.9 shows, graphically represent respectively, the von-Mises stresses (a) and maximum principal stresses (b) for the three different loading conditions. As it can be seen that the von-Mises stress increase with the increase of the load. However, the increment is not that significant. The maximum von-Mises stress develops in the corner zone located at the connection between the main shaft and middle crank web. The low average von Mises stress indicates that the developed von Mises stress in the other portion of the crankshaft is significantly lower than that in the maximum zone. A similar trend can also be observed for maximum principal stress results. The negative minimum principle stress implies that the developed stress is compressive in nature. According to the obtained results, the

maximum von-Mises stress and the maximum principal stress are 130.99 MPa and 148.37 MPa, respectively, for the 180 kN compressive loading condition.

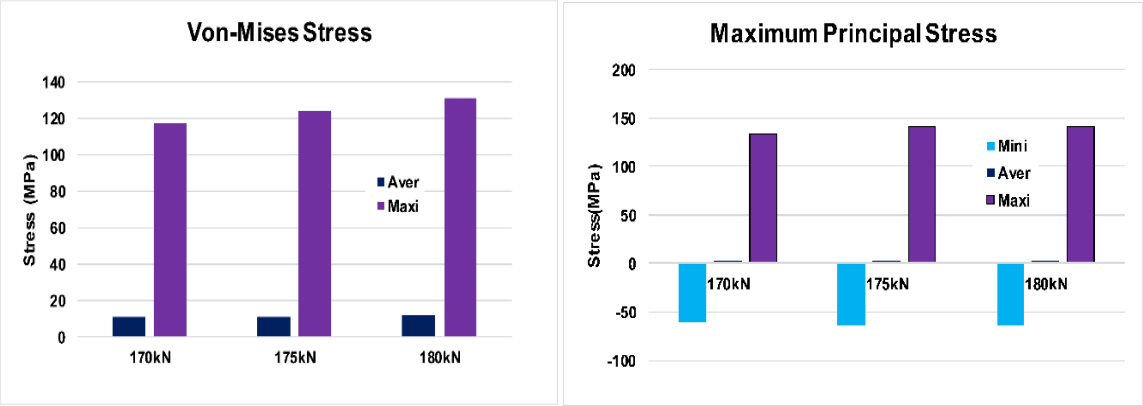

(a) (b)

Fig. 3.9: von-Mises Stress (a) and Maximum Principal Stress (b) for three different compressive loading conditions. Note that Mini represents the minimum principle stress that is compressive in nature.

Likewise, figure 3.10-3.12 represents an equivalent strain contour plot for three different compressive loads. For better comparison, Figure 3.13 also illustrates the equivalent strain and maximum principal strain results for the compressive loading conditions.

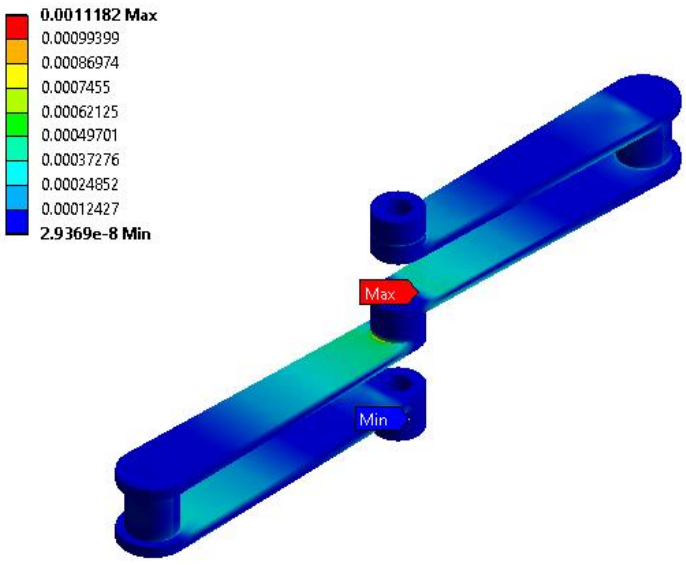

Fig 3.10: Equivalent strain contour plot for compressive load 170Kn

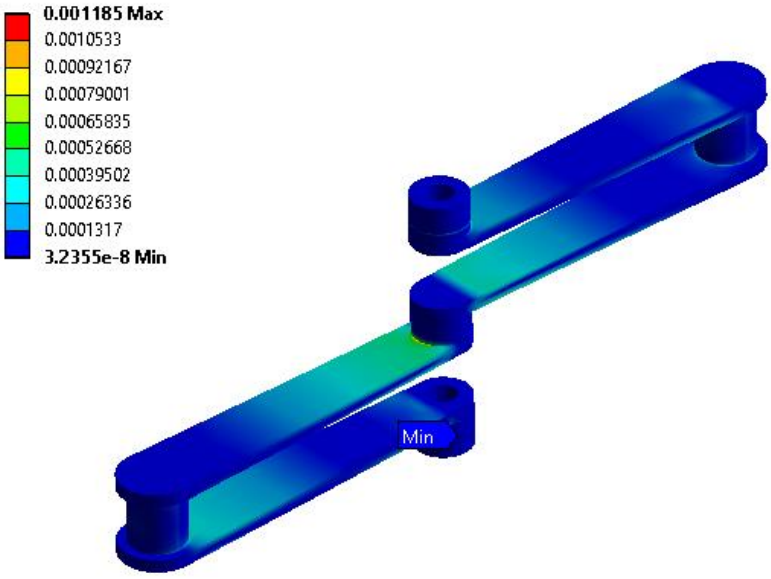

Fig 3.11 : Equivalent strain contour plot for compressive load 175Kn

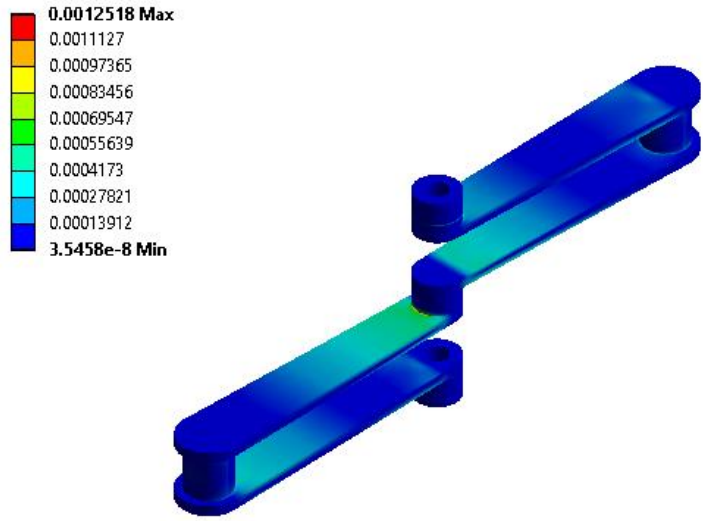

Fig 3.12: Equivalent strain contour plot for compressive load 180 Kn

The maximum equivalent strain and principal strain are detected, respectively, to be 0.0012518 and 0.00089, which are acceptable for the safety of the design. The factor of safety of the design is calculated and plotted in Fig. 3.14. Note that to calculate the factor of safety maximum equivalent stress theory has been deployed. The minimum factor of safety obtained is 13.15 which is far above the design requirements. In this presentation, min and max indicate specific location factors of safety.

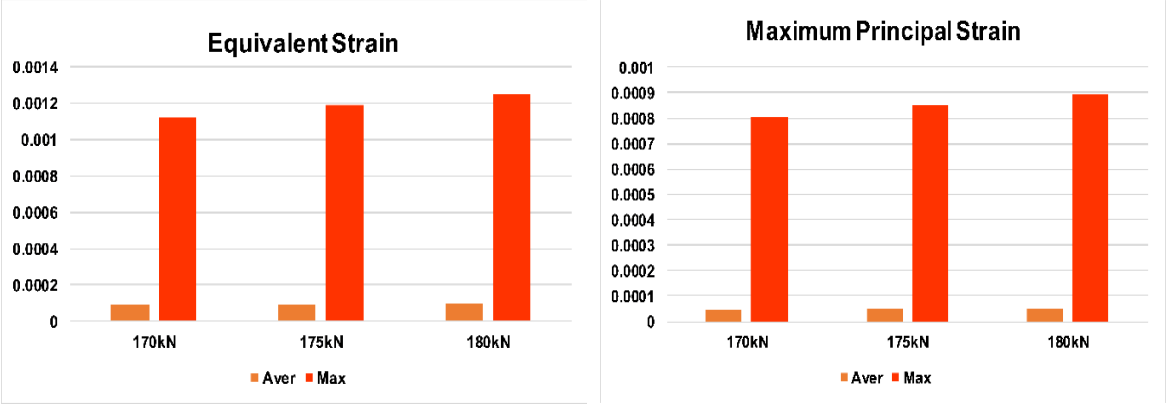

(a) (b)

Fig. 3.13: Equivalent Strain (a) and Maximum Principle Strain (b) for the three compressive loading conditions. Note that Aver represents the average strain throughout the crankshaft whereas Max indicates the maximum strain in the highest strain developed location.

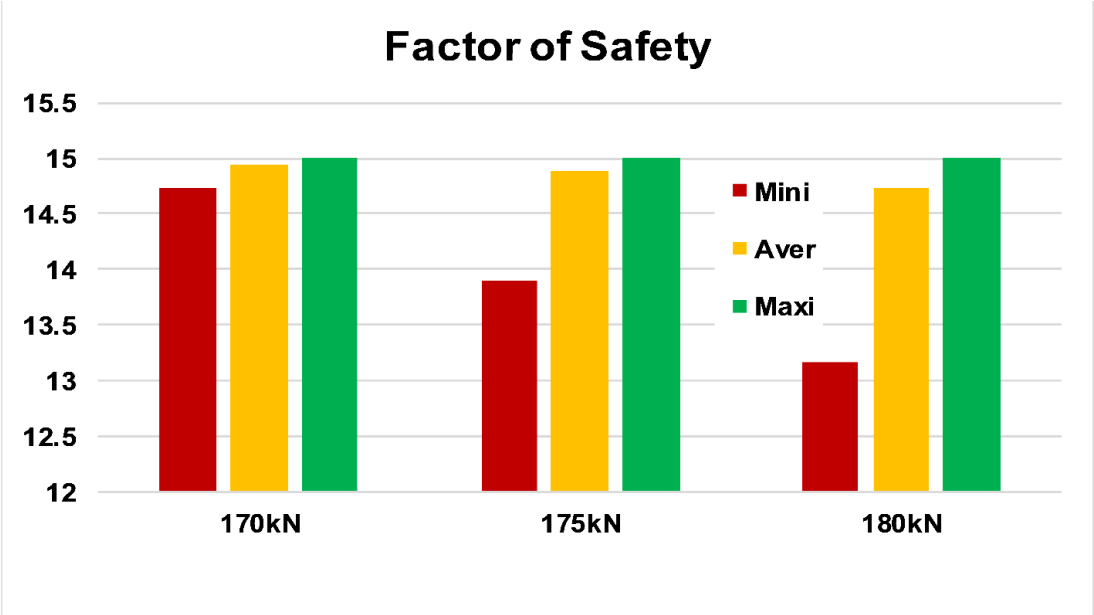

Fig. 3.14: Comparison of the factors of safety for the three compressive loading conditions

4.7 Effect of Tensile Load

In the present design, the crankshaft has to handle a tensile force of 336 kN which is almost twice the corresponding compressive load of 175 kN, which is one of the most challenging design requirements in this research project. Figure 3.15 shows the total deformation plots for three varying loading conditions. A maximum deformation of 6.29 mm has been observed at the middle crank web for 340 kN loading and the corresponding average deformation is 2.49 mm. Fig 3.16 – 3.18 present the Von-Mises contour plots for the associated tensile loading cases.

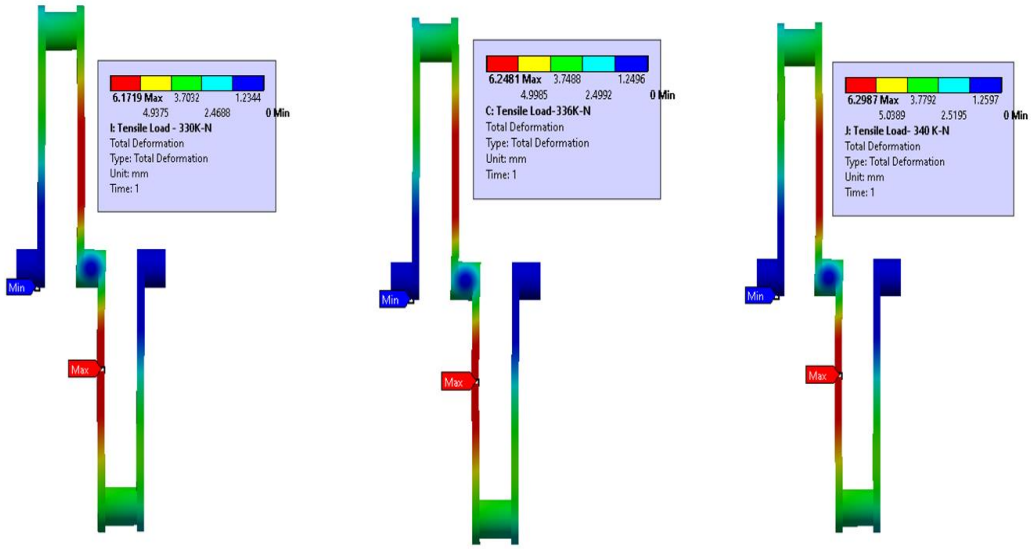

Fig. 3.15: Total deformation plots for tensile loads of 330, 336, and 340 kN.

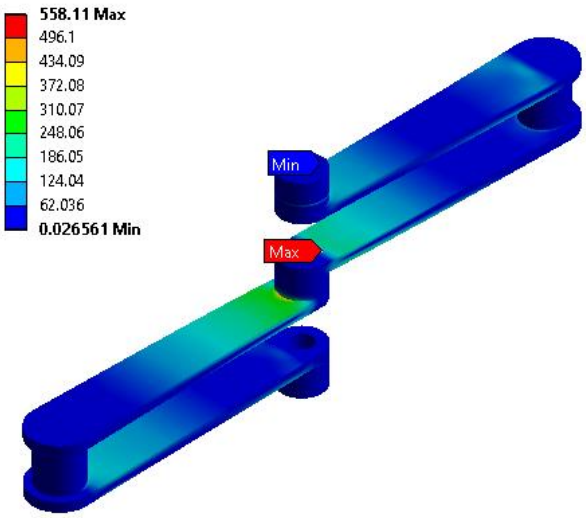

Fig 3.16 : Von-Mises stress contour plot for the compressive load 330 kN

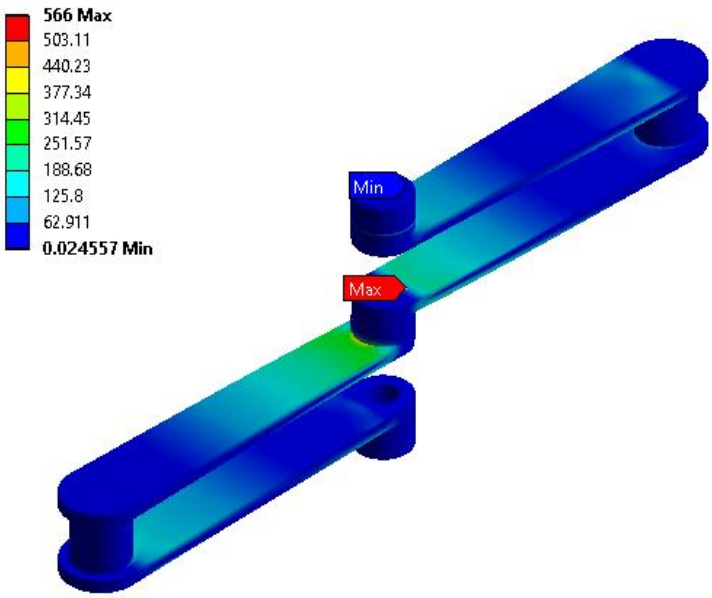

Fig 3.17: Von-Mises stress contour plot for the compressive load 336 kN

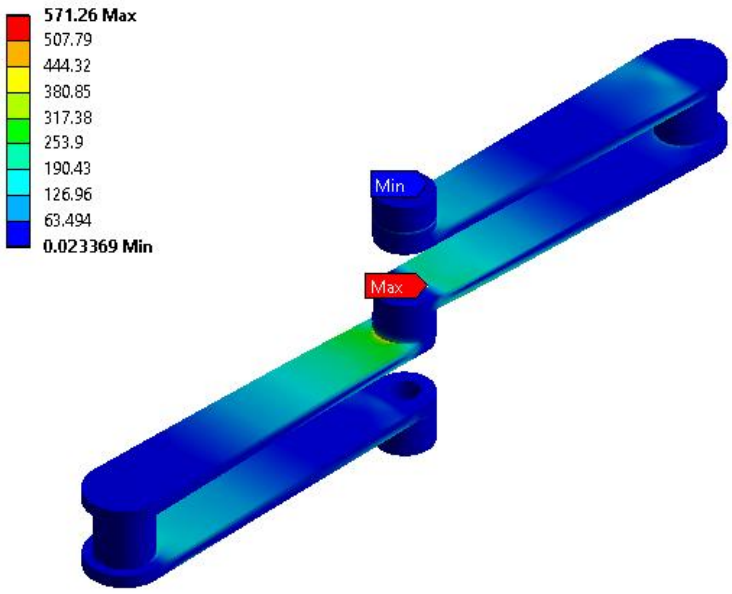

Fig 3.18: Von-Mises stress contour plot for the compressive load 340 kN

The maximum von - Mises stresses, corresponding to 330, 336 and 340 kN loading conditions are, respectively, 558, 566, and 571.26 MPa, as shown in Fig. 22a, and the maximum principal stress varies from 853.07 to 873.11 MPa (Fig. 22b). The maximum stress locations are at the junctions of the main shaft and the middle crank webs (see Fig. 3.23). However, all the developed stresses are within safe zones and tolerable for each loading condition.

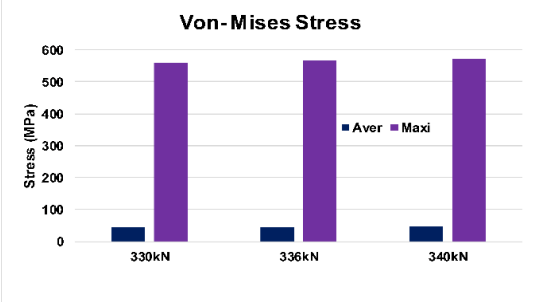

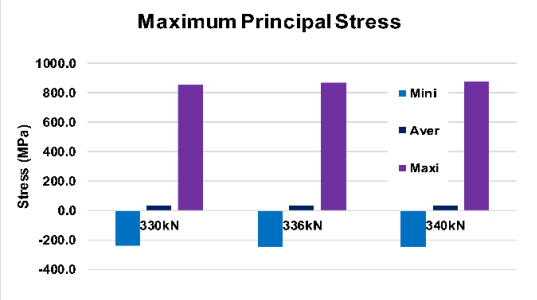

(a) (b)

Fig. 3.22: Stress results for three loading conditions, (a) von-Mises stress and (b) Maximum principal stress. Note that Mini represents the minimum principle stress that is compressive in nature.

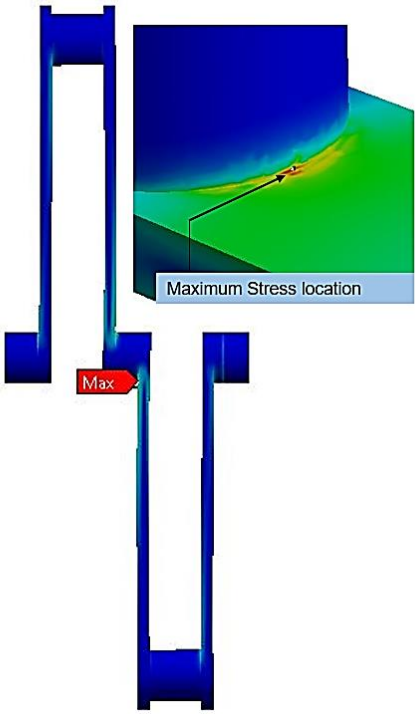

Fig. 3.23: Maximum von-Mises stress locations (corner zone between the main shaft and middle crank webs).

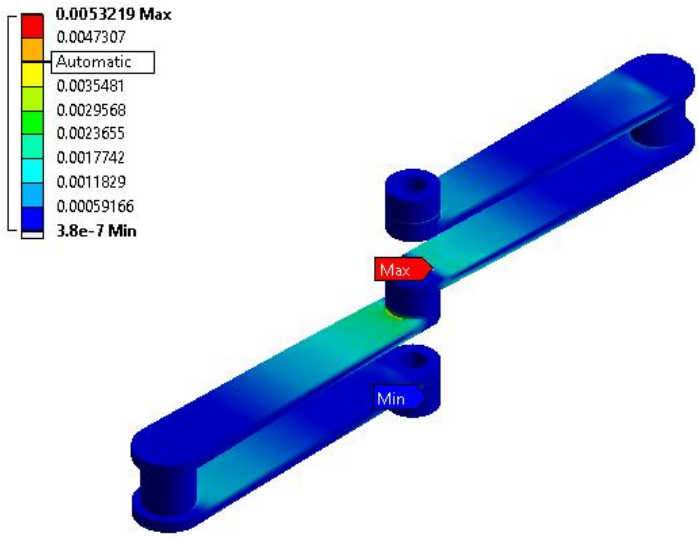

Fig 3.19: Equivalent strain contour plot for compressive load 330 Kn

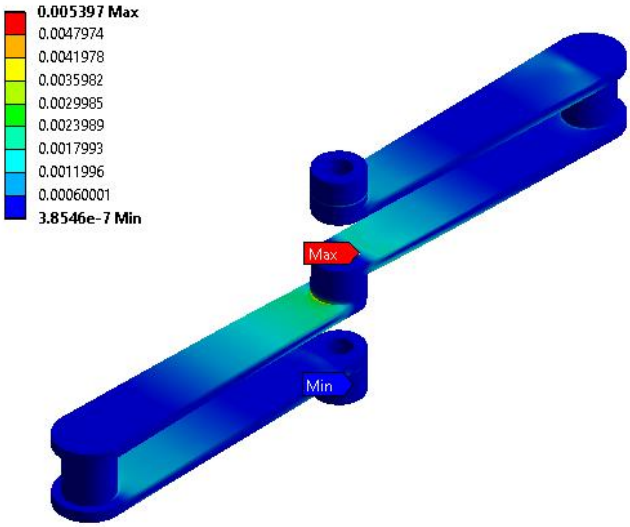

Fig 3.20: Equivalent strain contour plot for compressive load 336 Kn

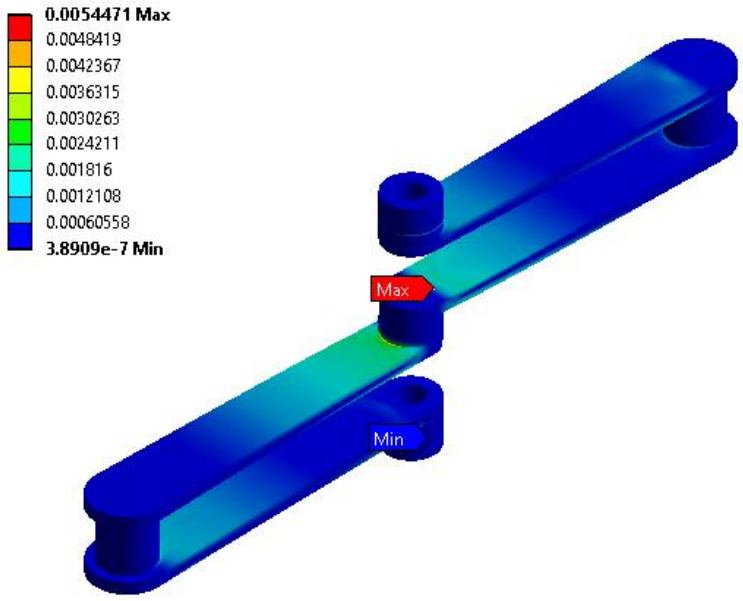

Fig 3.21: Equivalent strain contour plot for compressive load 340 Kn

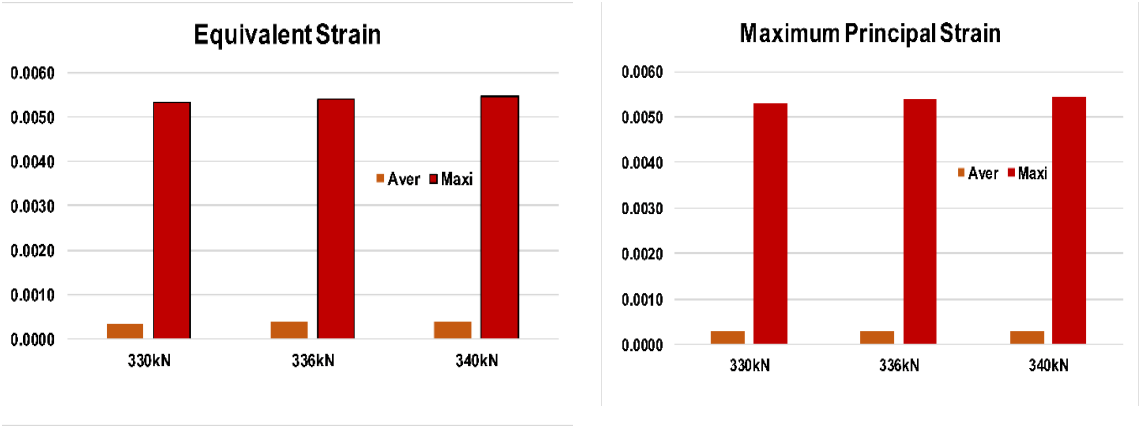

(a) (b)

Fig. 3.24: Equivalent Strains for the three loadings, (a) Maximum equivalent strain and (b) Maximum principal strain. Note that Aver represents the average strain throughout the crankshaft whereas Max indicates only the maximum strain in the highest strain developed area.

Figure 3.19- 3.23 present the equivalent strain contour plots for the three different tensile loading conditions whereas Figure 17 shows the equivalent and maximum strain results for each loading condition. In addition, Figure 3.25 presents the results of the factor of safety for each loading case. The minimum factor of safety obtained is 3.17 in the maximum stress zone, which is considerably lower than that of the compression loading cases. However, the design is still safe for the present loading conditions.

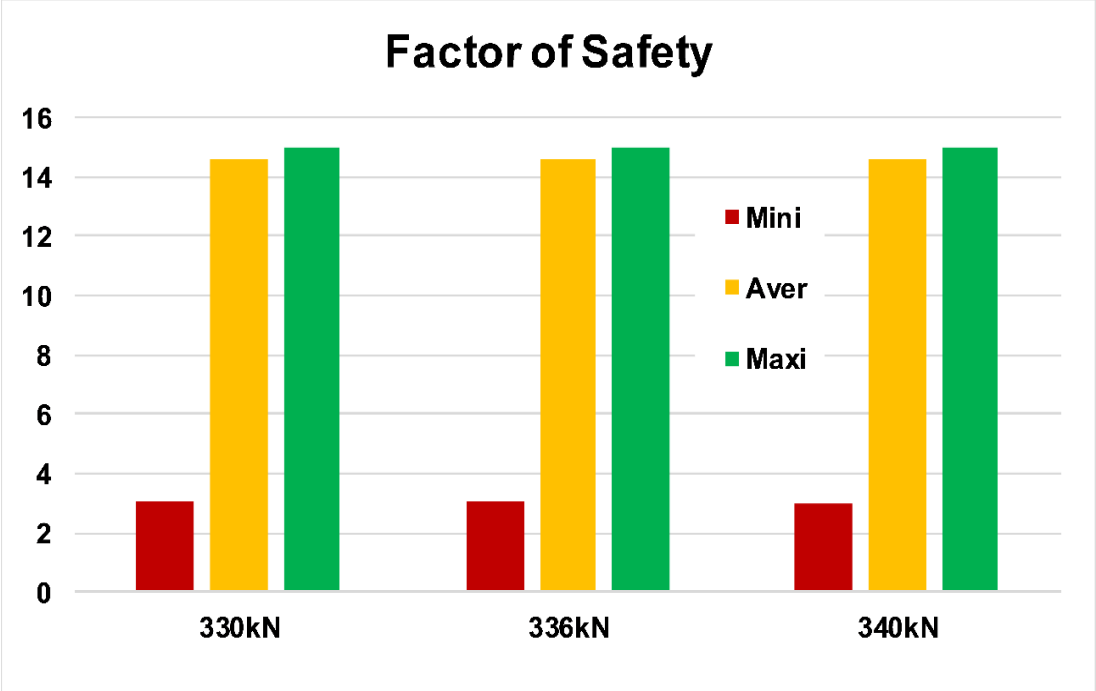

Fig. 3.25: Comparison of the factors of safety for different tensile loading conditions

Based on the above results, it seems that the corner zones experience higher stress than any other locations, and special attention may be directed to these zones. There are four critical corner zones and their respective von - Mises stresses are plotted in Fig. 26. It is noted that location 3 in Fig. 26 is the maximum stress location in the crankshaft. Although the stresses in the corner zone are higher than any other locations in the crankshaft, the developed stresses are acceptable because they are far below the crankshaft material's yield strength.

Also, the critical corner zones may be structurally enhanced to increase the factor of safety in these zones without meaningfully increasing the weight of the crankshaft. These zones have relatively low safety factors because they are sharp corners. However, the application of fillet/chamfer or a simple structural modification could significantly increase safety in these regions with a minimum weight penalty. Also, all the stress results are obtained herein without the support between the two cranks, indicating that the crankshaft herein is structurally sound to work as the reciprocating driver of the RA-driven aircraft.

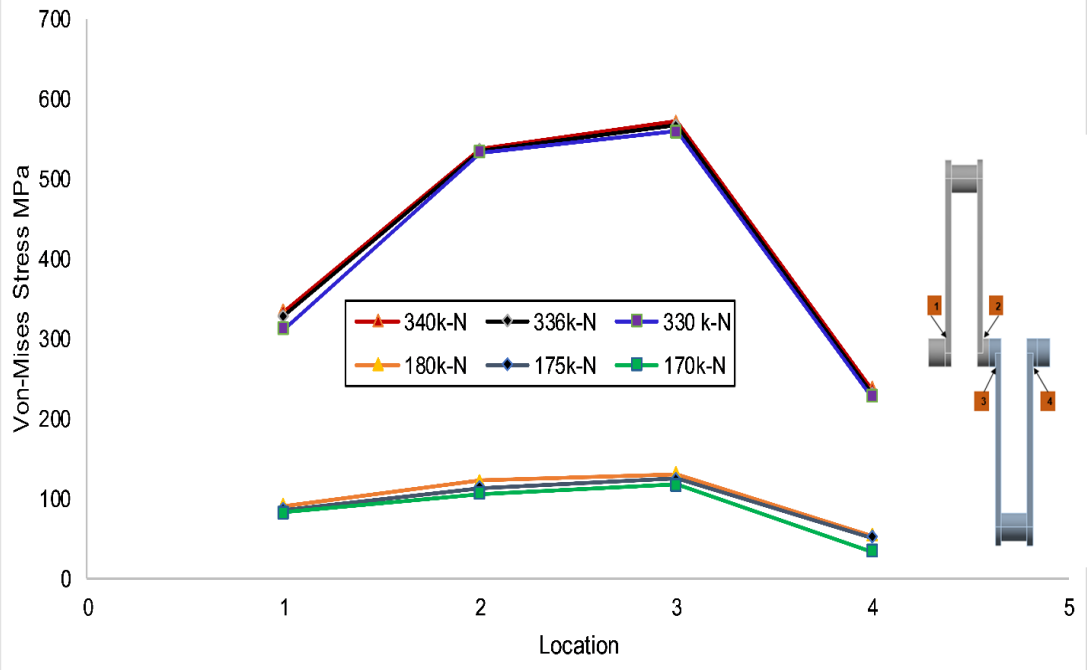

Fig 3.26: Von-Mises stress variation in four corner zones in the Crankshaft

4.8 Free vibration Analysis

To study the dynamic characteristics of the designed crankshaft, a free free modal analysis was undertaken. The purpose of this study is to examine the natural frequencies, mode shapes, and mode vectors of the crankshaft. Table 3 provides the crankshaft's first ten natural frequencies and their corresponding modes. Also, the change of frequencies has been plotted with respect to the mode number (Fig. 3.27). A sample three-mode shape deformation plot is presented in Fig. 3.28. For the present application, the working frequency of the crankshaft is 12 Hz whereas the resonance frequency is 26.51 Hz at the 7th mode. Therefore, the possibility of resonance is low.

Table 4.3: Frequency and corresponding modes

Mode	Frequency	Type of Mode
1	0	Rigid body displacement
2	0	Rigid body displacement
3	0	Rigid body displacement
4	0	Rigid body displacement
5	6.1269e-004	Bending is predominate
6	7.258e-004	Bending is predominate
7	26.51	Torsion is predominant
8	31.031	Torsion is predominant
9	77.937	Bending and Torsion predominant

10	90.947	Bending and Torsion predominant

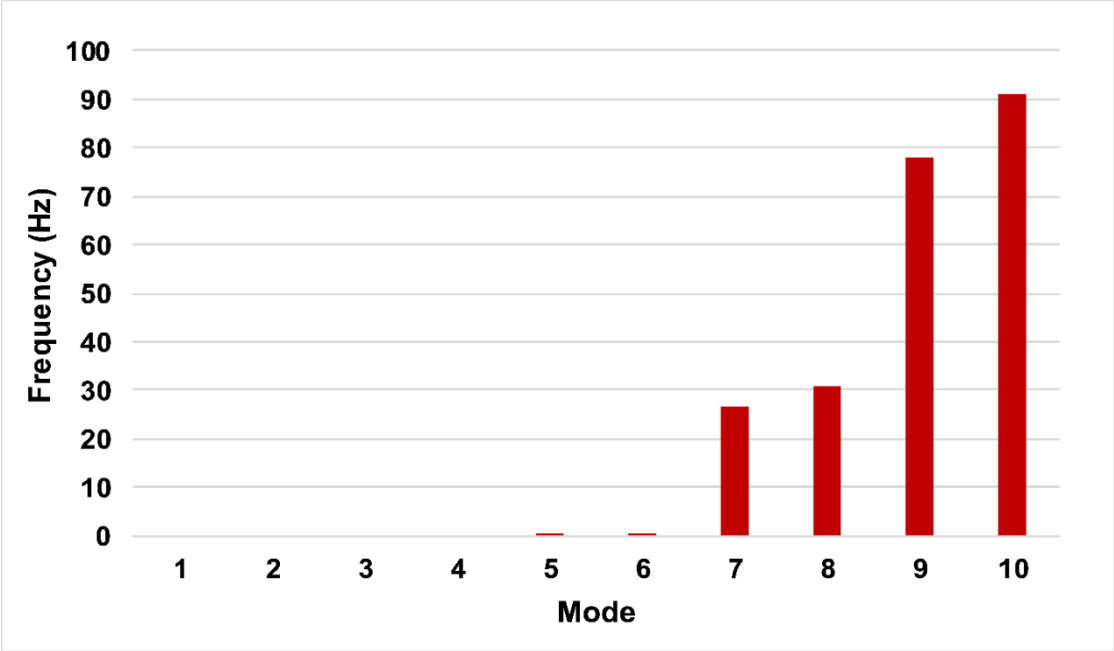

Fig. 3.27: Variation of frequency for first ten-mode shape.

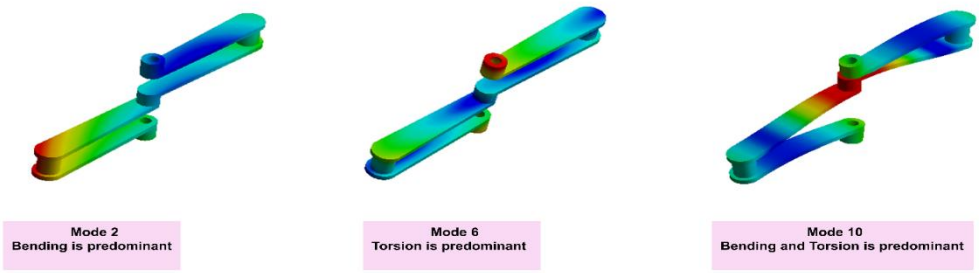

Fig. 3.28: Sample deformation for three modes

Chapter 5

5 Connecting Rod design

5.1 Background

Connecting rod is a dynamic component in IC engine /compressor or any mechanical system which is subjected to alternating direct compressive and tensile forces. The design and structural rigidity of the connecting rod strongly affect the associated system efficiency. Its design and development have always been challenging tasks to satisfy the low costs, minimum weight, sufficient rigidity, and other functional requirements. The objective of this study is structurally model a connecting rod to determine the feasibility of its use in the reciprocating driver of the new VTOL technology. The present study is a continuation of the previous studies where reciprocating the crankshaft has already been designed in the previous chapter. The reciprocating driver is a critical component of the VTOL technology to produce the long-stroke reciprocating motion of the two wings in an RA aircraft to generate lift during takeoff. By using a crankshaft-connecting rod system, the two wings reciprocate simultaneously with the same velocity magnitude, but in opposite directions so that the inertia forces and moments associated with both wings will be canceled. The conventional crankshaft-connecting system is inappropriate for this application because the current system requires a large crank radius, long connecting rods, and a small weight while handling large inertia forces simultaneously. Therefore, reciprocating-driver development is considered to be one of the most important and challenging steps toward the successful demonstration of new aircraft applications.

5.2 Model Design and Boundary Conditions

The primary goal of this research is to model a connecting rod with a length of 2.76 m that has to reciprocate a wing assembly simultaneously in a back-and-forth motion. It should be noted that without sufficient reciprocating stroke, the wings cannot generate the necessary lift during aircraft takeoff and landing time. Figure 5.1 shows a SolidWorks design of the connecting rod with its necessary dimensions.

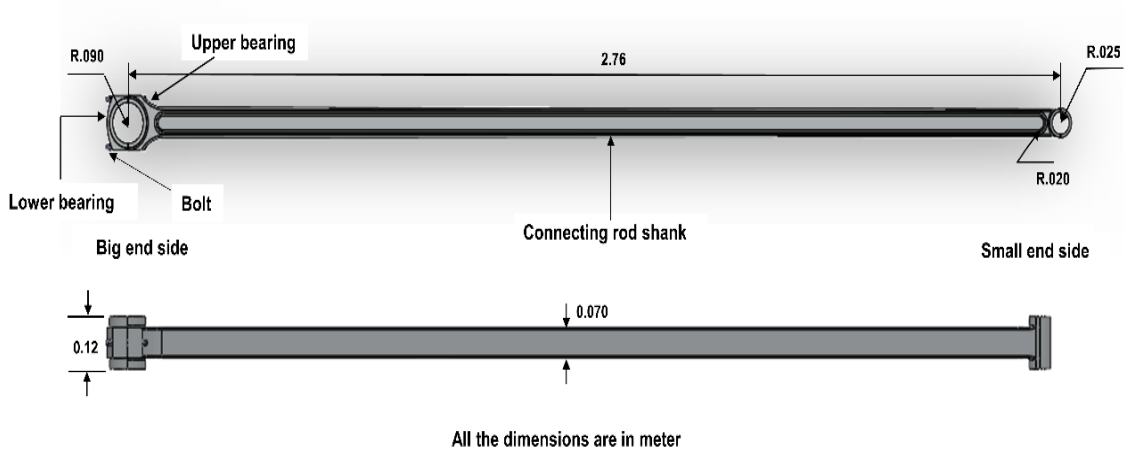

Fig. 5.1: Drawing and SolidWorks designed connecting rod with specified dimensions.

Since the maximum compressive and tensile inertia forces developed in the connecting rod are, respectively, 336 kN and 175 kN where the operating angular velocity of the crankshaft is 750 rpm, the designed connecting rod must withstand this large inertia force along with the other specified operating conditions. Note that the compressive load on the connecting rod is almost twice the tensile force. If it could withstand this massive compressive load, it can survive the tensile load as well. For brevity, the compressive load response of the connecting rod is presented in this chapter and their respective effects are discussed. However, the designed connecting rod is also investigated under maximum tensile load to ensure the design satisfies that criteria also. Since the connecting rod constitute both the large end (crankshaft side) and short end side (Pin), both ends should have sufficient structural rigidity to withstand this large inertial force. We developed numerical models to determine both ends' structural rigidity and presented the results accordingly. Figure 5.2 shows a sample of compressive boundary condition setup when the applied load is incorporated in the big end side along with the other associated conditions for the present numerical analysis. Note that here the acceleration is the maximum acceleration during operation.

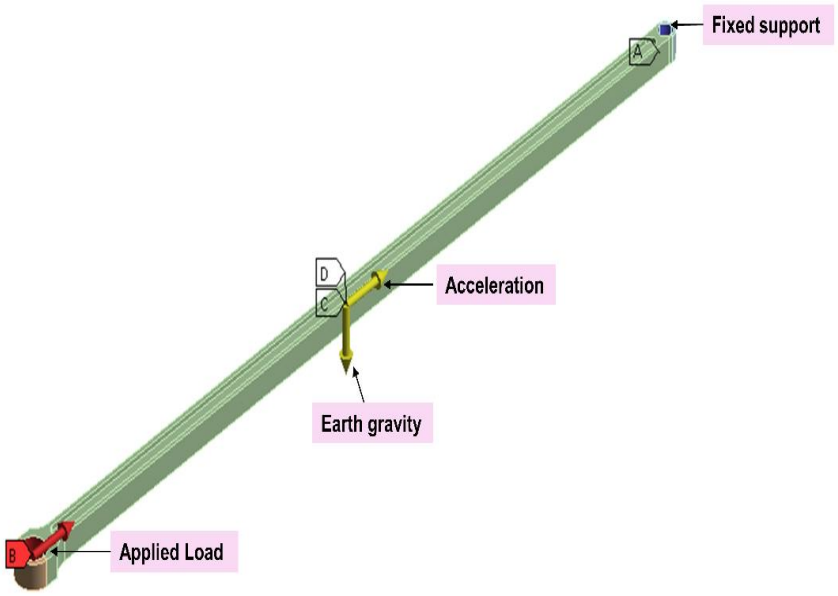

Fig. 5.2: A sample boundary condition setup at the big end side for non-linear static structural analysis.

5.3 Materials Selection

Along with the structural analysis, connecting rod material selection is a critical step. It should be noted that the weight of the reciprocating driver should be as low as possible so that it will not pose a significant penalty on the aircraft's direct lifting capability. Moreover, safety should be the highest priority for the design. Therefore, the selected connecting rod material should have sufficient strength to withstand the dynamic load of the wings with minimum weight. Although traditional connecting rod materials have acceptable strength

to withstand this load, the excessive weight due to their high mass density made them inappropriate for our application. As a result, it was concluded that new materials should be implemented to meet our prime requirements: small weight and high strength.

According to the Commercial software Granta EduPack analysis as well as the author's intensive discussion, several materials seem suitable for the current application. Among them, high-strength carbon fiber composite and widely used aluminum 6061 T6 alloy seem promising due to their low weight density and higher strength. The designation of the selected composite material is termed Bismaleimide + High Strength Carbon fiber composite. It is a family of thermoset (cross-linked) polyimides of which the simplest member has a formula (CH2(C6H4N(CO)2C2H2), where matrix material and filler/reinforcement material are respectively Bis-Maleimide (BMF-CF65) and carbon fiber. The filler/reinforcement material represents a 60–70% portion of the total composite weight. Carbon fiber composites have been extensively used in many aerospace-related applications, such as high-speed flight controls, engine inlets, missile components, and aerospace components where elevated-temperature performance is required. Recently Rolls-Royce manufactures UltraFan demonstrator blades made of Carbon-titanium composite [71]. Another example is a new Carbon Fiber V12 engine being built by the automobile company Lamborghini [67,68]. On the other hand, aluminum alloy 6061 is composed primarily of three different elements: magnesium, silicon, and aluminum. The percentage varies based on its application. It has excellent corrosion resistance, high-moderate strength, superior machinability, and affordability. Table 5.1 presents important mechanical properties of the high-strength carbon fiber and aluminum alloy 6061 T6.

Table 5.1: Mechanical properties of High strength carbon fiber and Aluminum alloy.

Properties	High Strength carbon fiber	Aluminum Alloy 6061 T6	Unit
Density	0.0567-0.0582	0.09708	lb/in^3
Young's Modulus	$15.9\text{-}18.9\times10^{06}$	1.029×10^{07}	psi
Yield Strength	248-252	40-45	ksi
Tensile Strength	248-252	40-45	ksi
Compressive Strength	175-194	40-43	ksi
Flexural Strength (Modulus of rupture)	248-252	43.36	ksi
Poisson's ratio	0.3-0.335	0.33	
Hardness-Vickers	21.6-47.4	107	HV
Unit price	43.4-52.1	5.12-6.20	Usd/lb

5.4 Mesh Independent Test and Validation of the numerical model

The commercial Ansys Mechanical Solver was used to perform finite element analyses where the tetrahedral grid was selected to discretize the computational domain (see Fig. 5.3). The tetrahedral grid can easily combine with curvature and proximity and also the

software has the feature to automatically refine the mesh in critical regions. The tetrahedral grid has been widely used in numerical simulations [72–77]. Moreover, it is quick, and advantageous for complicated geometries. The numerical-model accuracy highly depends on the mesh quality. According to Ansys meshing guidelines, to ensure high-quality mesh, the mesh orthogonal quality should be as high as possible, where very good and excellent mesh spectra are respectively between 0.7-0.95 and 0.95-1.00. Likewise, the skewness mesh matric quality should be as low as possible where very good and excellent quality spectra are respectively 0.25-0.50 and 0-0.25. It should be noted that those mesh quality guidelines are mainly for CFD applications. For structural modeling, this general meshing guideline is more flexible and forgivable. However, we decided to ensure the highest accuracy in our meshing. Regarding that, our average orthogonal mesh metrics and average skewness are respectively 0.72 and 0.26 which fall within the very good mesh quality spectrum. Further, we performed a grid independence test by varying the number of grids from 254890 to 1256540 so that our result is independent of the grid number. The final number of 830140 control volumes was selected, at which the grid independence is achieved. Figure 5.4 shows the grid-independence test results in terms of the change of total deformation with respect to grid numbers. It is evident from Figure 5.4 that the percentage change of total deformation becomes insignificant after a grid number of 830140, and beyond this grid number the computation cost, as well as time, will increase but without increasing solution accuracy meaningfully. In our prior chapter, the validation of the numerical model and its details have been discussed broadly.

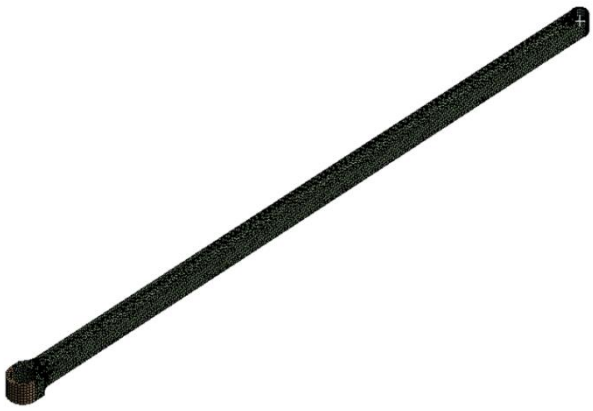

Fig. 5.3: Mesh view of the crankshaft model

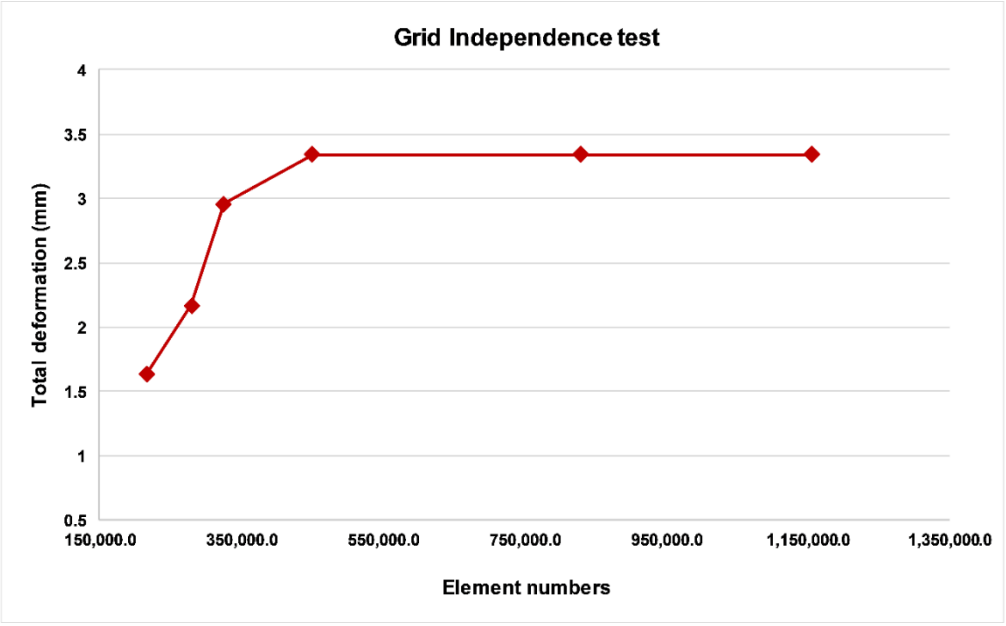

Fig. 5.4: Grid-independent test results.

5.5 Result and Discussion

FEA analyses were performed for the modeled connecting rod for both high-strength carbon fiber and Aluminum 6061 alloys to determine their stress responses. In the analysis, the maximum compressive load of 336 kN was applied on both the big-end and small-end sides of the connecting rod to check its structural rigidity. For each loading condition, the connecting rod response was presented and analyzed under different safety factor tools.

Figure 5.5 shows the total deformation plot for the applied compressive load in connecting rod at both ends. The maximum deformation developed is respectively about 10.11 mm and 3.34 mm for the aluminum alloy and carbon fiber materials when the applied load is incorporated on the big-end side. On the other hand, when the applied load is incorporated on the small-end side the maximum developed deformation is respectively 4.24 mm and 2.34 mm for aluminum alloy and carbon fiber materials. Although the deformations are acceptable, it seems that the developed deformation is large when the load has been applied to the connecting rod's big end side compared with the same loading condition on the small end side.

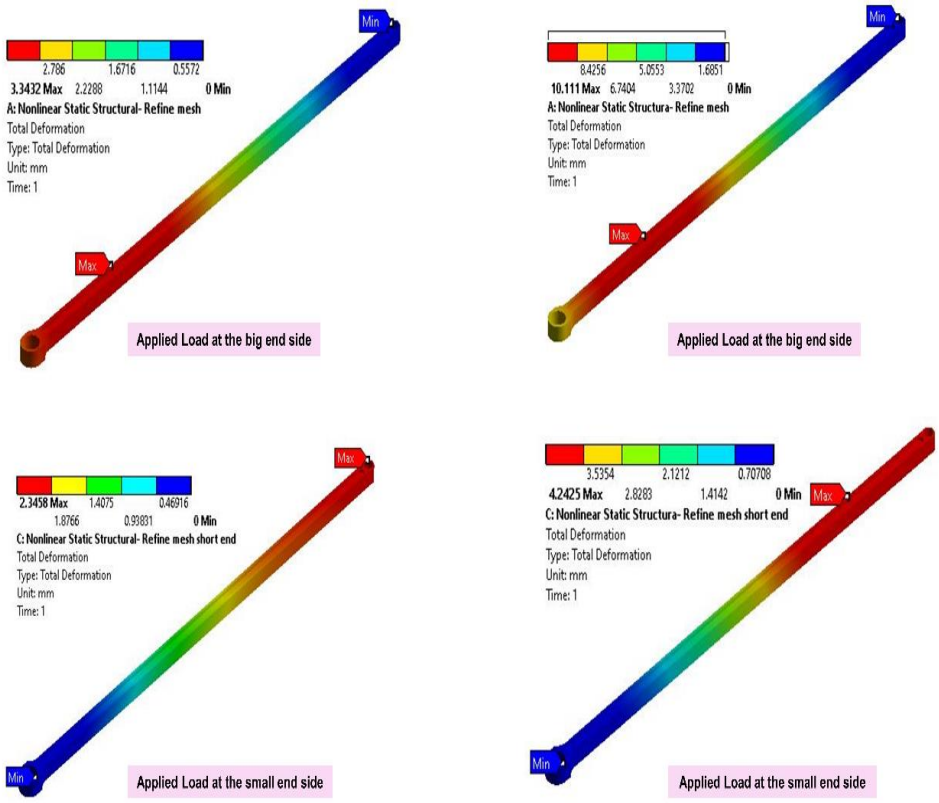

(a) (b)

Fig. 5.5: Total deformation plots (a) Carbon fiber composite (b) Aluminum Alloy

Figures 5.6 to 5.9 represent the von-Mises stress contour plot for both connecting rods. Similarly, Figure 5.10 shows, respectively, (a) The von-Mises stresses and (b) The maximum principal stresses for the connecting rod on both the big-end and small-end sides. As can be seen that the von-Mises stress increase when the load is applied on the small-end side compared to the big-end side. However, the increment is not that significant. The maximum von-Mises stress develops at the junction between the connecting-rod shank and the lower bearing zone. The low average von Mises stress (represent as “aver” in the figure)

indicates that the developed von Mises stress in the other portion of the crankshaft is significantly lower than that in the maximum zone.

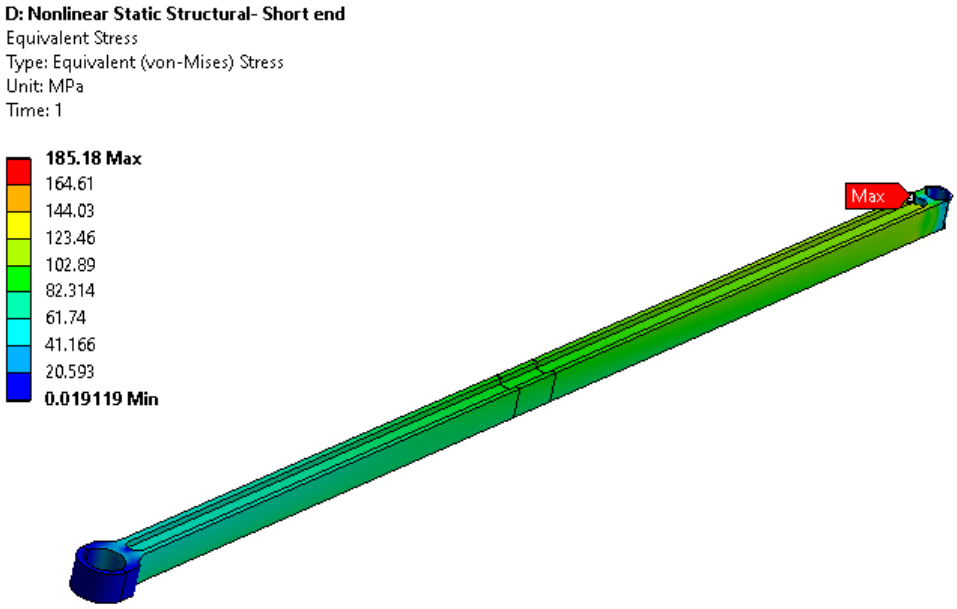

Fig 5.6: Von Mises stress contour for carbon fiber connecting rod when the load applied on Big end side

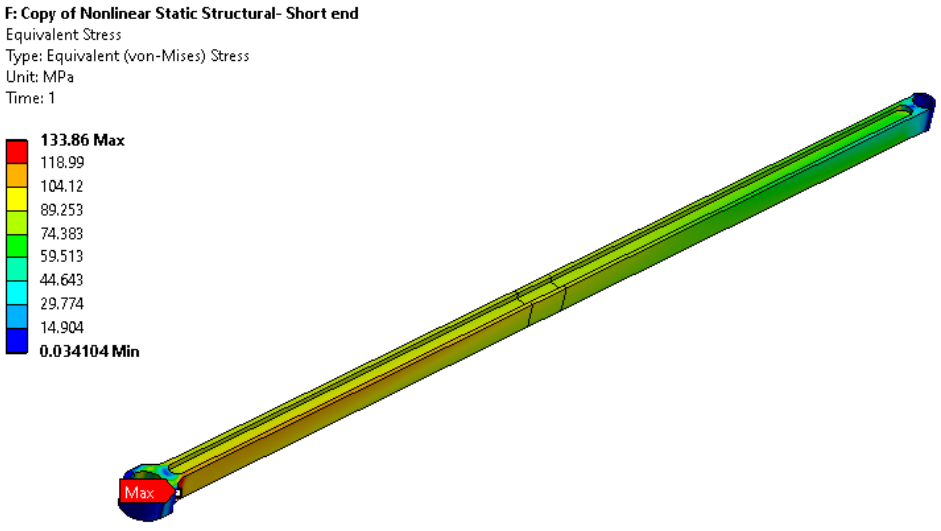

Fig 5.7: Von Mises stress contour for carbon fiber connecting rod when the load is applied on the small-end side.

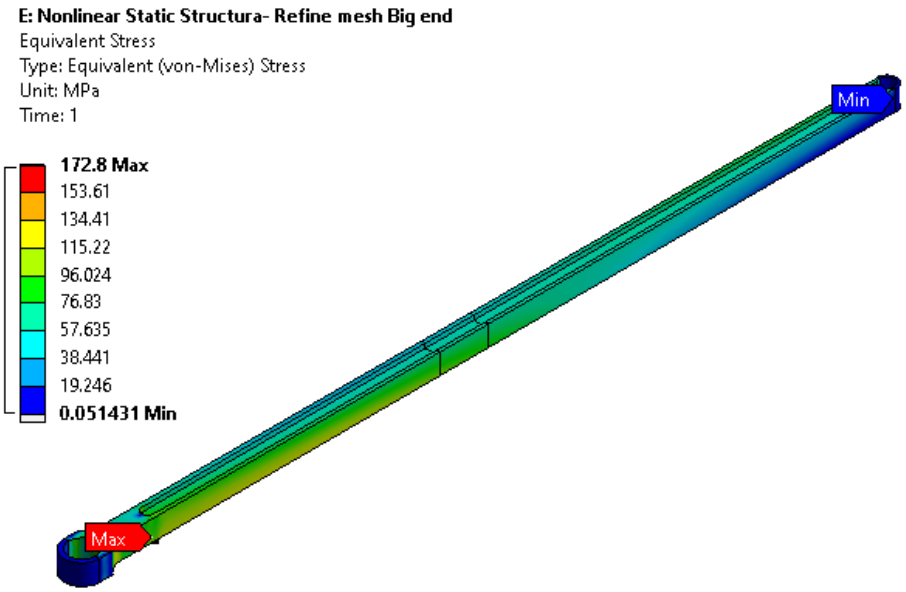

Fig 5.8: Von Mises stress contour for Aluminum connecting rod when the load is applied on the small-end side.

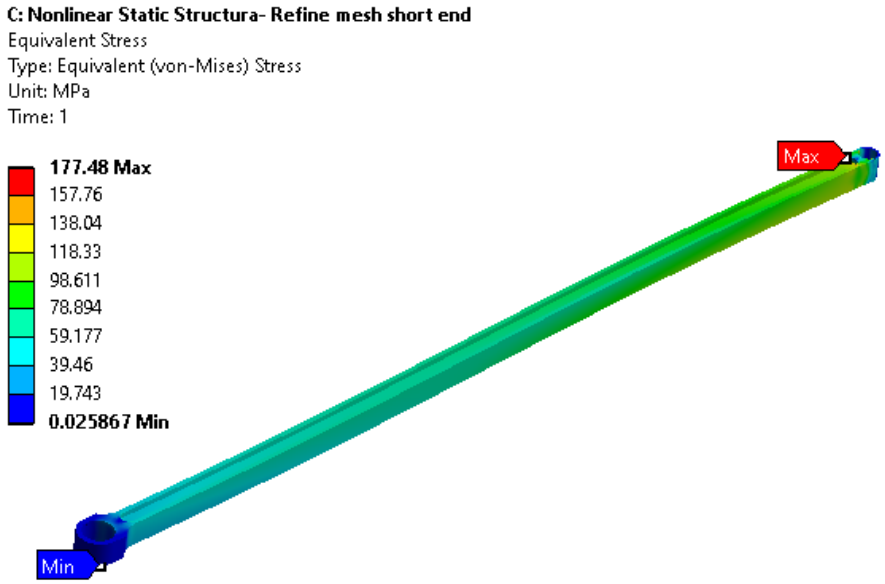

Fig 5.9: Von Mises stress contour for Aluminum connecting rod when the load is applied on the small-end side.

A similar trend can also be observed for maximum principal stress results. The negative minimum principle stress implies that the developed stress is compressive in nature. According to the obtained results, the maximum von-Mises stress and the maximum principal stress are 181.85 MPa and 86.073 MPa, respectively, for the carbon fiber connecting rod when the load is applied on the small-end side.

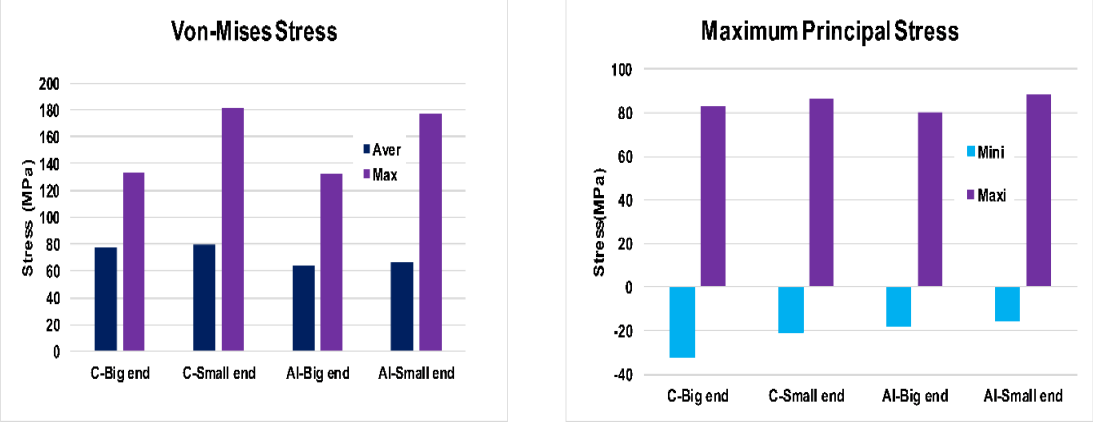

(a) (b)

Fig. 5.10: (a) von-Mises Stress (b) Maximum Principal Stress. Here C represents Carbon fiber composite and Al represents Aluminium alloy. Note that Mini represents the minimum principle stress that is compressive in nature.

Figure 5.11- 5.14 illustrates the equivalent strain and maximum principal strain contour plot for both connecting rods. Likewise, Fig. 5.15 demonstrates results for the equivalent strain and maximum principal strain for the connecting rod under maximum compressive loading conditions. The maximum equivalent strain and maximum principal strain are detected, respectively, to be 0.00250 and 0.00095, which are acceptable for the safety of the design. The design factor of safety is calculated and plotted in Fig. 5.16. The minimum factor of safety obtained is 1.577 when the load is applied on the small-end side in the

aluminum alloy materials. In this presentation, min and max indicate specific location factors of safety.

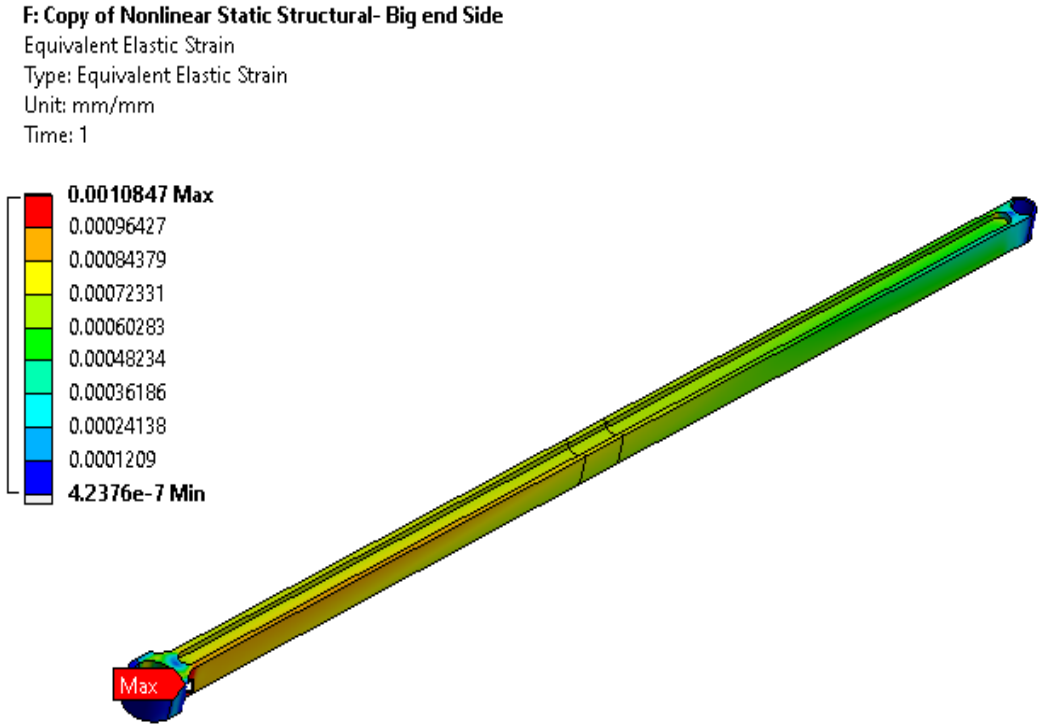

Fig 5.11: Equivalent Elastic Strain contour for carbon fiber connecting rod when the load is applied on the big-end side.

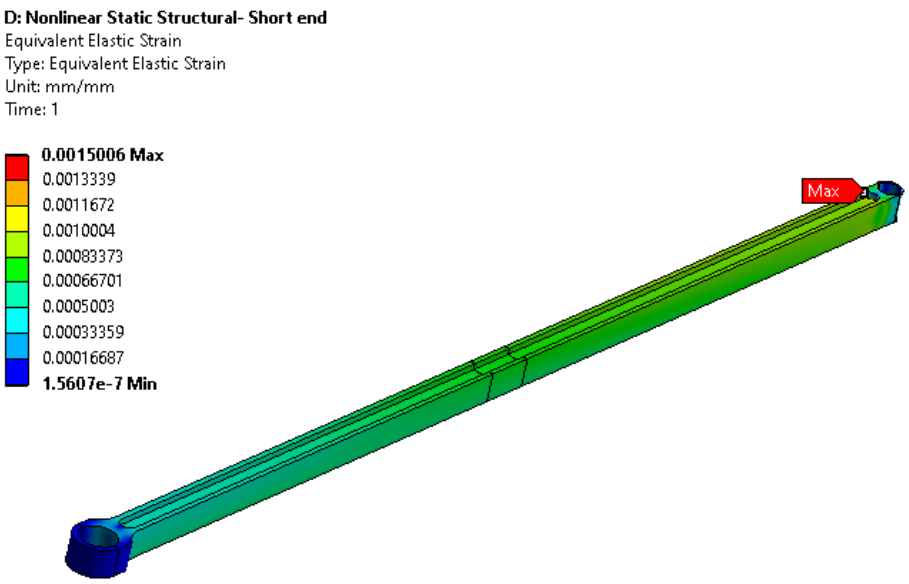

Fig 5.12: Equivalent Elastic Strain contour for carbon fiber connecting rod when the load is applied on the small-end side

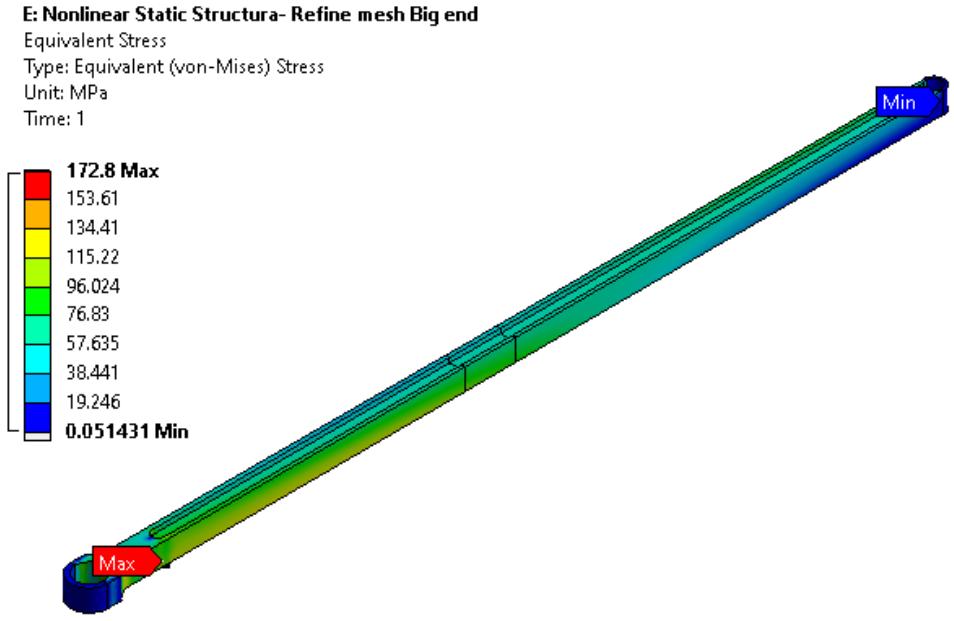

Fig 5.13: Equivalent Elastic Strain contour for Aluminum connecting rod when the load is applied on the big-end side.

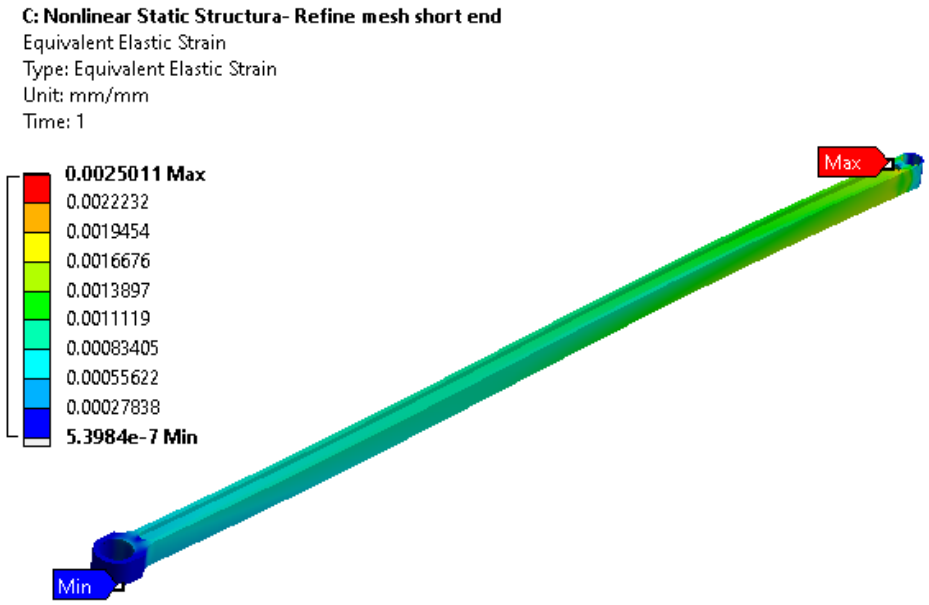

Fig 5.14: Equivalent Elastic Strain contour for Aluminum connecting rod when the load is
applied on the small-end side

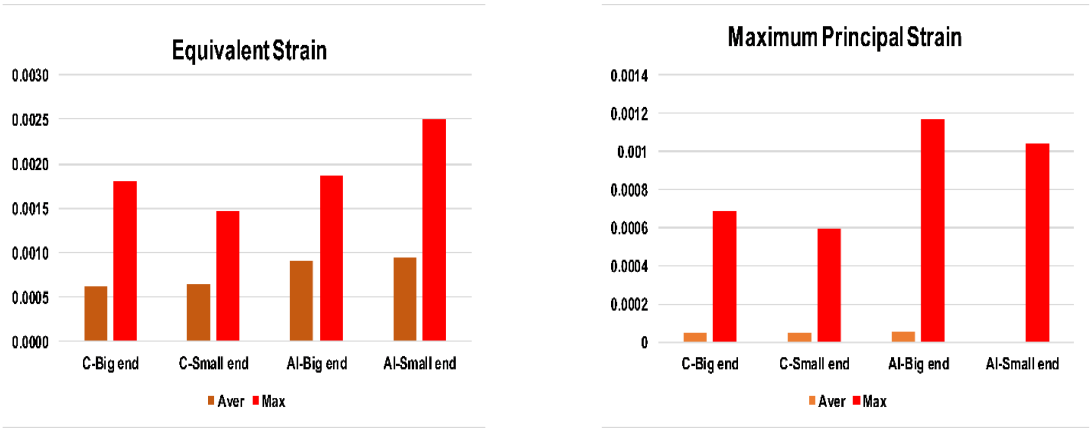

(a) (b)

Fig. 5.15: (a) Equivalent Strain and (b) Maximum Principle Strain for the designed connecting rod. Note that Aver represents the average strain throughout the connecting rod whereas Max indicates the maximum strain in the highest strain developed location.

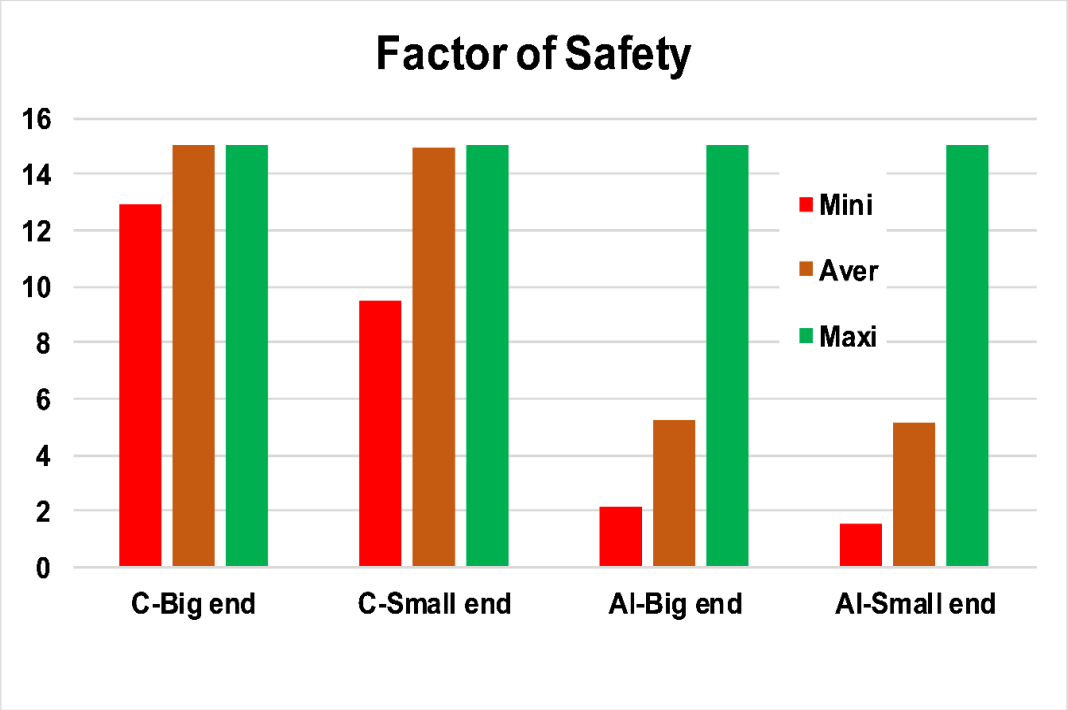

Fig. 5.16: Comparison of the factors of safety between big-end and small-end sides as well as carbon fiber and Aluminium alloy materials.

It should be noted that the associated factor of safety in Fig. 5.16 is obtained by using the Maximum Equivalent stress theory. However, in structural design and analysis, there are several failure theories that have been developed and show merit for successful designs. Using wrong or inaccurate failure theory might lead to compromise and inaccurate designs which ultimately increased cost, time, and effort. As a result, the present design has been analyzed under the most widely practiced all failure theories: maximum equivalent stress, Mohr-coulomb, Max shear stress, and Max tensile stress theory. Table 5.2 represents the safety factor of the connecting rods when the load is applied on the small-end side whereas table 5.3 represents the safety factor of the

connecting rods when the load is applied on the big-end side. According to the result in tables 5.2-5.3, it seems that the factor of safety values for the first three failure theories has less difference. However, the maximum tensile stress theory value overestimates the design factor of safety compared with the rest of the theories.

Table 5.2 Safety factor of the design according to different safety tools when the load is applied on the small-end side

Safety Tool	Aluminum Alloy			Carbon Fiber		
	Min	Max	Aver	Min	Max	Aver
Maximum Equivalent stress theory	1.577	15	5.1726	9.3081	15	14.998
Mohr-Coulomb Stress	1.558	15	5.1223	6.8417	15	14.98
Max Shear Stress	1.565	15	5.1358	9.230	15	13.361
Max Tensile Stress	3.1688	15	14.962	15	15	15

Table 5.3: Safety factor of the design according to different safety tools when the load is applied on the big-end side

Safety Tool	Alluminum Alloy			Carbon Fiber		
	Min	Max	Aver	Min	Max	Aver
Maximum Equivalent stress theory	1.62	15	5.3104	12.87	15	14.998
Mohr-Coulomb Stress	1.60	15	5.26	12.673	15	14.99
Max Shear Stress	1.61	15	5.27	9.33	15	14.474
Max Tensile Stress	3.3668	15	14.945	15	15	15

According to the above presented, the structure developed stress under maximum compressive load is way less than both materials' yield strength. Figure 5.17 represents the maximum stress locations for the big-end and small-end sides.

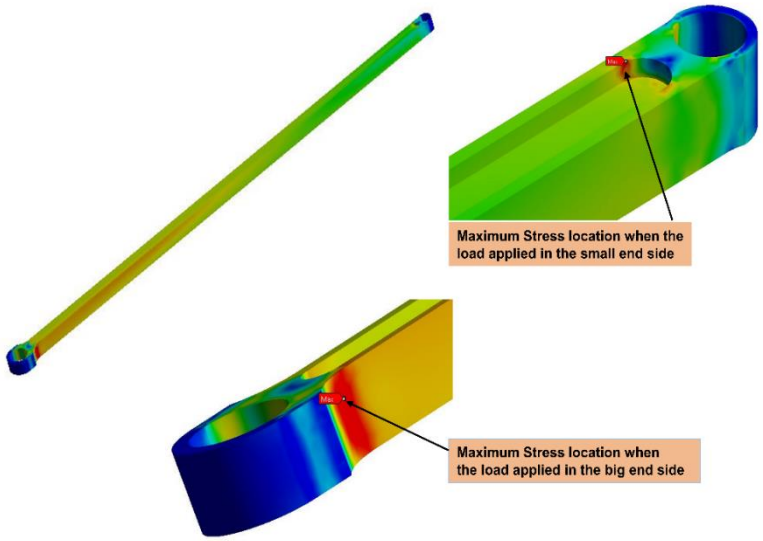

Fig. 5.17: Maximum von-Mises stress locations (Big-end side: transition zone between the connecting rod shank and lower bearing zone; for small-end side: fillet zone near the small-end side)

It can easily be understood from Fig. 5.17 that the presented maximum developed stress is a stress concentration point/zone which defines as a point/zone in the structure where developed stress is significantly higher than the surrounding area. In our design, the average developed stress is significantly lower than this stress concentration point. In engineering practice, there are several ways this stress concentration zone can be improved to enhance the structure's overall rigidity as well as safety. In our case, we could implement a large fillet radius in the stress concentration zone which will definitely improve the stress condition of this stress-concentration zone. Moreover, we could install relief notches in the vulnerable zone that will also reduce the high-stress concentration zone. For the small-end side, the common techniques of avoiding sharp edges will

remove this stress concentration. The application of those techniques not only reduces the stress in the structure but also improves the design's overall rigidity and safety.

5.6 Eigenvalue Analysis

Due to the nature of the current loading conditions and long connecting rod length (high slenderness ratio, *l/r*), it is a prerequisite to analyze the geometric failure/buckling phenomena of the designed connecting rod. Connecting rod demonstrates two types of buckling modes during its operation: One is side buckling and the other is front-rear buckling (Fig. 5.18). There are several approaches that are in use to study structure buckling phenomena. Analytically, the Ranking formula has been used to calculate the critical buckling load which is the harmonic mean of the Euler equation and yield strength. It should be mentioned that the Euler equation applies only to uniform cross-section columns and specific boundary conditions. The elastic term in the Euler equation is valid when not only the column is an ideal slender column with uniform cross-section but also under specific boundary conditions such as pined–pined, fixed–fixed, and pined–fixed joints. Thus, the analytical approach for our connecting rod is incompatible with the Euler formula assumption in three critical aspects. First, the present connecting rod shank has non-uniform cross-sections along with the length. Secondly, connecting rod buckling constant (K) is different from the classical one due to the nature of the present boundary conditions where both ends of the connecting rod are connected with the pin and crankshaft. Finally, it is difficult to define the effective length of connecting rod during

front-rear buckling phenomena. Consequently, an enhanced formula should be adopted for the shaped design of the connecting rod shank.

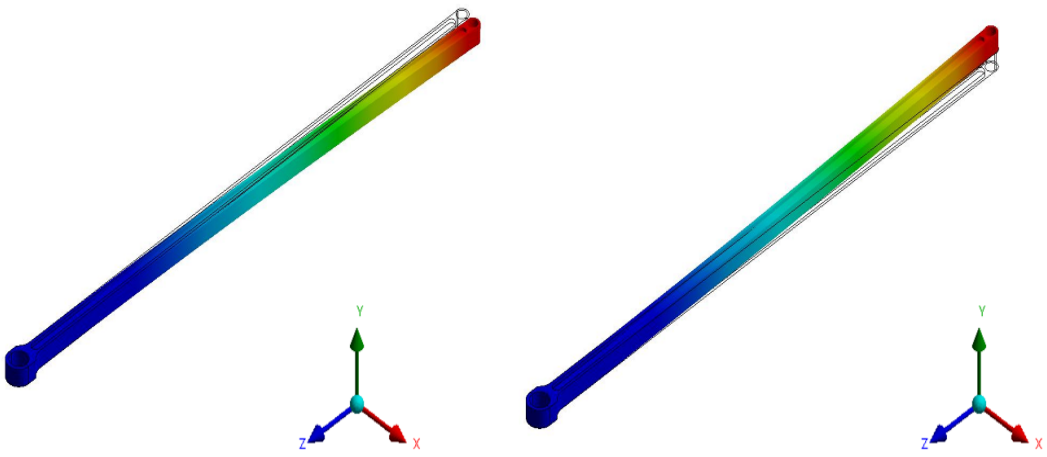

(a) (b)

Figure 5.18: Buckling mode of the connecting rod: (a) Side buckling and (b) Front-rear buckling

In this regard, three-dimensional FEA buckling analysis has the advantage to adopt the actual boundary conditions as well as the present shape design. This study also presents a nonlinear buckling study for the connecting rod via FEA to avoid geometric failure/buckling failure. According to the nonlinear static analysis, all the associated stress is under the material's yield strength. However, the designed connecting rod buckling

response should be evaluated to check the overall lateral stiffness of the structure to overcome any possible local and global buckling failure. According to the nonlinear buckling model analysis, the global load factor is respectively 50.55 and 15.894 for carbon fiber and Aluminium alloy connecting rods whereas the cross-section of the connecting rod has been improved slightly with a weight enlargement. Also, there are no local buckling phenomena that were identified in the designed connecting rods during loading conditions. Table 5.4 represents the first four modes of Buckling load factor (BLF) for both Carbon fiber and Aluminum alloy connecting rods. Here, the buckling load factor (BLF) is defined as the factor of safety against buckling or the ratio of the buckling loads to the applied loads where the first positive load factor is the desired result.

Table 5.4: Buckling load factor for Carbon fiber and Aluminum alloy connecting rods.

BLF value for Carbon fiber Materials	BLF value for Aluminum Materials	Buckling Status	Notes
-98.69	-33.006	-1 < BLF < 0	Buckling is not predicted. It is predicted only if you reverse all loads.
-52.771	-17.962	-1 < BLF < 0	Buckling is not predicted. It is predicted only if you reverse all loads.

50.55	15.894	1 < BLF	The applied loads are less than the estimated critical loads. Buckling is not expected.
96.128	30.832	1 < BLF	The applied loads are less than the estimated critical loads. Buckling is not expected.

Based on the result, the minimum buckling load factors are respectively 50.55 and 15.894 for carbon fiber and aluminum alloy connecting rods and indicate the connecting rod rigidity against buckling failure.

5.7 Free Vibration Test

In this section, both connecting rods undergo a free vibration test to avoid any possible vibration failure. The purpose of this study is to examine the natural frequencies, mode shapes, and associated mode vectors of the connecting rod. Under the extensive vibration test, the connecting rod response was carefully observed, analyzed, and tabulated in Table 5.5 and Table 5.6. Note that table 5.5 presents the first ten natural frequencies and their corresponding modes and briefly describes the dominance of the deformation for aluminum connecting rods. Similarly, Table 5.6 presents the first ten natural frequencies and their corresponding modes and briefly describes the dominance of the deformation for carbon fiber connecting rods. According to the obtained result, none of the natural

frequencies is close to the application working frequency. Therefore, it emphasized that the possibility of resonance, as well as failure of the connecting rod due to vibration, is highly unlikely. Figures 5.19 to 5.21 represent three deformation modes.

Table 5.5: Frequency and corresponding mode for Aluminum connecting rod

Mode	Frequency	Type of Mode
1	0	Rigid body displacement
2	0	Rigid body displacement
3	0	Rigid body displacement
4	5.19e-004	Rigid body displacement
5	1.8277e-003	Bending and Torsion predominant
6	3.5099e-003	Bending and Torsion predominant
7	36.689	Bending is predominant
8	44.896	Bending is predominant
9	101.22	Bending is predominant
10	123.43	Bending and Torsion predominant

Table 5.6: Frequency and corresponding mode for Carbon fiber connecting rod

Mode	Frequency	Type of Mode

1	0	Rigid body displacement
2	0	Rigid body displacement
3	0	Rigid body displacement
4	0	Rigid body displacement
5	4.826e-003	Bending is predominant
6	7.5944e-003	Rigid body displacement
7	64.088	Bending is predominant
8	78.376	Bending is predominant
9	176.83	Bending is predominant
10	215.63	Bending and Torsion predominant

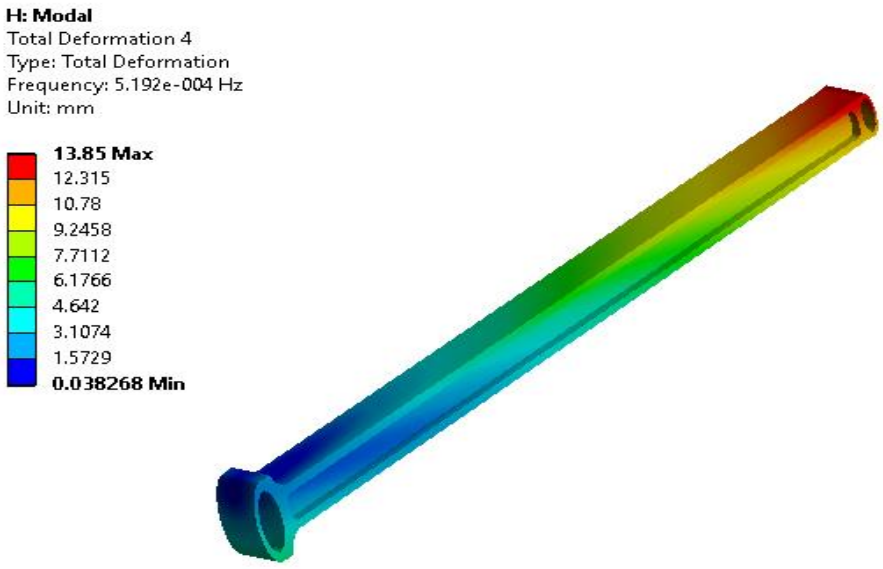

Fig 5.19: Rigid body displacement mode

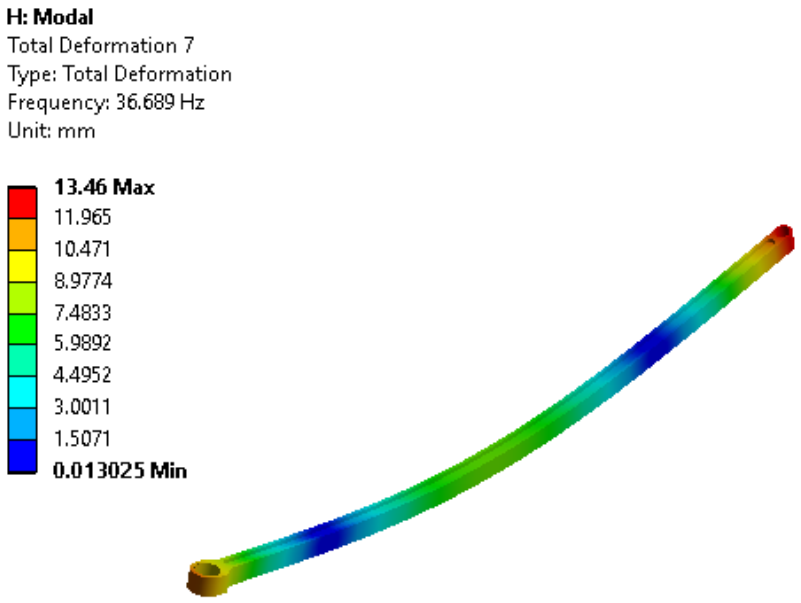

Fig 5.20: Bending is the predominant mode

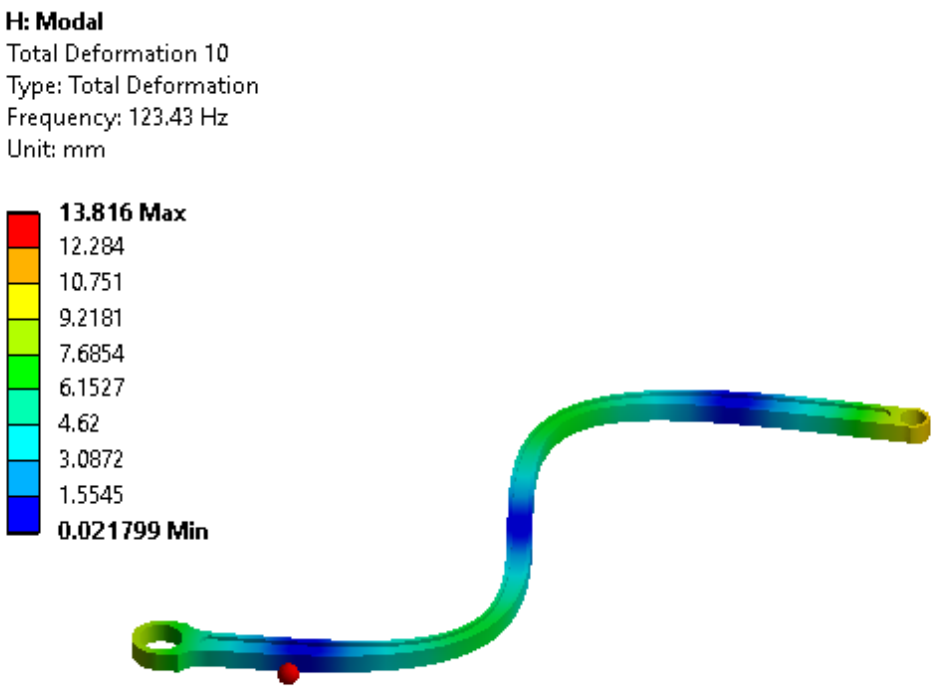

Fig 5.21: Bending and torsion is the predominant mode. Note that the presented deformation is scaled 120 times higher than the actual deformation scale.

Chapter 6

6 Conclusion

In this research, a reciprocating airfoil (RA) driver has been developed numerically for the novel vertical takeoff and landing (VTOL) aircraft. This is the first time that a unique crankshaft driver has proven effective as a driving mechanism for aircraft applications. The design and development of the reciprocating driver have posed a strenuous challenge toward its successful deployment because of the specific nature of the application and the operating conditions. Notably, the driver has to reciprocate two wings simultaneously with the same velocity magnitude but in opposite directions. Additionally, it has to maintain a large crank radius to generate necessary wing strokes in conjunction with a long connecting rod, whereas stringent weight minimization is a prerequisite for handling large inertia forces simultaneously. In this study, a comprehensive numerical framework is proposed in order to model and investigate the reciprocating driver response in a variety of working conditions. Regarding that, three-dimensional Rigid body dynamics, analytical, Nonlinear Static, Modal, and Nonlinear Eigenvalue models were created. The numerical model has been validated against the available experimental data provided by the Forging Industry Educational Research Foundation (FIERF) and the American Iron and Steel Institute (AISI). The response of the designed reciprocating driver was investigated extensively to avoid any possible failure due to stress, vibration, buckling, etc.

In the preliminary stage of this research, several traditional crankshaft designs were proposed and analyzed under different working conditions. However, all the traditional crankshaft systems failed to render reliable systems because of the operational demands

and stringent weight minimization constraints. As such, a high-strength carbon fiber composite crankshaft has been proposed, designed, and analyzed. The crankshaft's detailed responses under different working conditions have been carefully investigated as well as evaluated under various safety tools. The structural parameters examined include total deformation, von-Mises and maximum principal stresses, and equivalent and maximum principal strains, all of which are acceptable to the present structural design. The result showed that the maximum deformation, Von-Mises stress, and principal stress of the crankshaft exposed are, 6.29 mm, 571.26 MPa, and 873.11 MPa, respectively, under 340 kN tensile loading conditions. The maximum stress is developed in the corner zone at the junction between the main shaft and the crank web. However, it is still safe since the safety factor is above 3. Furthermore, the junction can be structurally improved with a minimal weight penalty by applying a fillet, chamfer, or structural modification. The average safety factor under the highest loading is above 14, and the possibility of resonance is low since the close resonance frequency (26.51 Hz) is distant from the working frequency (12 Hz).

In the second stage of the research, the numerical modeling of the connecting rods has been performed to produce a detailed result from the wide-ranging nonlinear static, vibration, and eigenvalue studies. The proposed connecting rods have been made of both Carbon fiber and Aluminum alloy 6061 T6 materials where the structural rigidity of the connecting rods was tested on both big and small end sides. According to the nonlinear static analysis, the maximum von-Mises stress and the maximum principal stress are 181.85 MPa and 86.073 MPa, respectively, for the Carbon fiber connecting rod, while the maximum von-Mises stress and the maximum principal stress are 179.85 MPa and 89.053 MPa,

respectively, for the Aluminum connecting rod when the load is applied on the small end side. The minimum factor of safety is confirmed at 9.308 and 1.57, respectively, for Carbon fiber and Aluminum connecting rods. The Nonlinear Eigenvalue model investigated the local and global bucking phenomena due to the presence of a large compressive load. The findings confirmed that the designs are able to circumvent both local and global buckling failures. Furthermore, according to the modal analysis result, the closed natural frequency is 36.689 and 64.088, respectively, for Aluminum and Carbon fiber connecting rods to avoid any possible resonance.

In conclusion, the current study proposed and developed a structurally sound reciprocating crankshaft driver as a driving mechanism for the novel Vertical Takeoff and Landing (VTOL) aircraft. Successful implementation of this novel driver will facilitate a fixed-wing aircraft with added Vertical Takeoff and Landing (VTOL) capability. Moreover, it is intended that the present study and comprehensive numerical framework/workflow can also serve as a useful reference for the structural design and development community. Finally, this study beacons the potential implementation of the novel RA-driven VTOL technology for drone and Unmanned Aerial Vehicle (UAV) flying mechanisms as well.

References

[1] O'brien, M. A., and Mcmasters, A. W., 1992, "The V-22 Osprey: A Case Analysis."

[2] Nalls, A., and Stortz, M., 1993, "Assessment of Russian VSTOL Technology Evaluating the YAK-38'FORGER'and YAK-141'FREESTYLE'."

[3] Dow, A., 2009, *Pegasus, the Heart of the Harrier: The History and Development of the World's First Operational Vertical Take-off and Landing Jet Engine*.Pen and sword.

[4] Charles, B. C., 1961, "Flight Tests of a 1/6-Scale Model of the Hawker P 1127 Jet VTOL Airplane."

[5] Abras, J., and Narducci, N., 2010, "Analysis of CFD Modeling Techniques over the MV-22 Tiltrotor," in 66th Annual Forum of the American Helicopter Society, pp. 11–13, American Helicopter Society, Inc.

[6] Kemp, E. D. G., 1969, "Studies of Exhaust-Gas Recirculation for VTOL Aircraft," J. Aircr., **6**(2), pp. 102–108. https://doi.org/10.2514/3.44015.

[7] Lieblein, S., 1970, "A Review of Lift Fan Propulsion Systems for Civil VTOL Transports," arc.aiaa.org. https://doi.org/10.2514/6.1970-670

[8] Lieblein, S., 1970, "Problem Areas for Lift Fan Propulsion for Civil VTOL Transports."

[9] Akturk, A., Camci, C., 2011, "A Computational and Experimental Analysis of a Ducted Fan Used in VTOL UAV Systems," personal.psu.edu.

[10] Carlson, S., 2014, "A Hybrid Tricopter/Flying-Wing Vtol Uav," 52nd Aerospace Science Meeting, National Harbor, MD, January 13-17, 2014.

[11] Gu, H., Lyu, X., Li, Z., Shen, S., and Zhang, F., 2017, "Development and Experimental Verification of a Hybrid Vertical Take-off and Landing (VTOL) Unmanned Aerial Vehicle (UAV)," ieeexplore.ieee.org. pp. Doi: 10.1109/ICUAS.2017.7991420.

[12] Cao, Y., US Patent App. 16/967, 200, 2020, "Reciprocating Lift and Thrust Systems," Google Patents.

[13] Solidworks, D. S.-V., 1995, "SolidWorks®," dl-ak.solidworks.com.

[14] Cao, Y., "Congruity Aerospace" [Online]. Available: https://www.congruityaerospace.com/.

[15] Heath, A., and McNamara, P., 1990, "Crankshaft Stress Analysis—Combination of Finite Element and Classical Analysis Techniques." J. Eng. Gas Turbines Power., 112(3): 268-275. https://doi.org/10.1115/1.2906491.

[16] Prakash, V., Aprameyan, K., and Shrinivasa, U., 1998, "An FEM Based Approach to Crankshaft Dynamics and Life Estimation," JSTOR. https://doi.org/10.4271/980565.

[17] Espadafor, F. J., Villanueva, J. B., and García, M. T., 2009, "Analysis of a Diesel Generator Crankshaft Failure," Eng. Fail. Anal., **16**(7), pp. 2333–2341. https://doi.org/10.1016/j.engfailanal.2009.03.019.

[18] Gomes, J., Gaivota, N., Martins, R. F., and Pires Silva, P., 2018, "Failure Analysis of Crankshafts Used in Maritime V12 Diesel Engines," Eng. Fail. Anal., **92**, pp. 466–479. https://doi.org/10.1016/j.engfailanal.2018.06.020.

[19] Mourelatos, Z. P., 2000, "An Efficient Crankshaft Dynamic Analysis Using Substructuring With Ritz Vectors," J. Sound Vib., **238**(3), pp. 495–527. https://doi.org/10.1006/jsvi.2000.3208.

[20] Montazersadgh, F. H., and Fatemi, A., 2007, "Stress Analysis and Optimization of Crankshafts Subject to Dynamic Loading." Final Project Report Submitted to the Forging Industry Educational Research Foundation and American Iron and Steel Institute. The University of Toledo, Toledo, OH.

[21] Peng, B., and Zhang, H., 2013, "Dynamic Loading and Stress Analysis on Crankshaft of Reciprocating Mud Pump," J. Vibroengineering, **15**(2), pp. 1048–1058.

[22] Kang, Y., Sheen, G. J., Tseng, M. H., Tu, S. H., and Chiang, H. W., 1998, "Modal Analyses and Experiments for Engine Crankshafts," J. Sound Vib., **214**(3), pp. 413–430. https://doi.org/10.1006/jsvi.1997.1512.

[23] Imumbhon, J. O., Alam, M. D., and Cao, Y., 2021, "Design and Structural Analyses of a Reciprocating S1223 High-Lift Wing for an RA-Driven VTOL UAV," Aerospace **8**(8), p. 214. https://doi.org/10.3390/aerospace8080214

[24] Alam, M. D., and Cao, Y., 2021, "Static and Modal Analysis of a Crankshaft Reciprocating Driver for Reciprocating-Airfoil (RA) Driven VTOL Aircraft," Mechanics Based Design of Structures and Machines. https://doi.org/10.1080/15397734.2021.1991807.

[25] Thejasree, P., Dileep Kumar, G., and Leela Prasanna Lakshmi, S., 2017, "Modelling and Analysis of Crankshaft for Passenger Car Using ANSYS," Mater. Today Proc., **4**(10), pp. 11292–11299. https://doi.org/10.1016/j.matpr.2017.09.053.

[26] Witek, L., Sikora, M., Stachowicz, F., and Trzepiecinski, T., 2017, "Stress and Failure Analysis of the Crankshaft of Diesel Engine," Eng. Fail. Anal., **82**(June), pp. 703–712. https://doi.org/10.1016/j.engfailanal.2017.06.001.

[27] Shahane, V. C., and Pawar, R. S., 2017, "Optimization of the Crankshaft Using Finite Element Analysis Approach," Automot. Engine Technol., **2**(1–4), pp. 1–23. https://doi.org/10.1007/s41104-016-0014-0.

[28] Singh, A., Mittal, V. K., and Angra, S., 2014, "Strength Analysis and Optimization Methods for Four Cylinder Engine Crankshaft Based on CATIA and ANSYS," Appl. Mech. Mater., **592**–**594**, pp. 1789–1793. https://doi.org/10.4028/www.scientific.net/AMM.592-594.1789

[29] Aliakbari, K., 2021, "Failure Analysis of Ductile Iron Crankshaft in Four-Cylinder Diesel Engine," Int. J. Met., **15**, pp. 1223-1237. https://doi.org/10.1007/s40962-020-00550-y.

[30] Mateus, J., Anes, V., Galvão, I., and Reis, L., 2019, "Failure Mode Analysis of a 1.9 Turbo Diesel Engine Crankshaft," Eng. Fail. Anal., **101**, pp. 394–406. https://doi.org/10.1016/j.engfailanal.2019.04.004.

[31] Jiao, A., Liu, B., Chen, X., Zou, X., and Wang, F., 2020, "Fracture Failure Analysis of KL Crankshaft," Eng. Fail. Anal., **112**, p. 104498. https://doi.org/10.1016/j.engfailanal.2020.104498.

[32] Pani, A., Patel, R., and Ghosh, G. K., 2020, "Buckling Analysis and Material Selection of Connecting Rod to Avoid Hydro-Lock Failure," Materials Today: Proceedings, **27**, pp. 2121-2126. https://doi.org/10.1016/j.matpr.2019.09.079. .

[33] Sathish, T., and Muthulakshmanan. A., 2018, "Design and Simulation of Connecting Rods with Several Test Cases Using AL Alloys and High Tensile Steel," academia.edu. DOI:10.24247/ijmperdfeb2018133

[34] Sonsino, CM., 1990, "Fatigue Design of Sintered Connecting Rods," Metal Powder Report, **45**(6) pp.408-412. https://doi.org/10.1016/S0026-0657(10)80139-0

[35] Yoo, Y. M., Haug, E. J., and Choi, K. K., 1984, "Shape Optimal Design of an Engine Connecting Rod." J. Mech., Trans., and Automation. **106**(3) pp. 415-419. https://doi.org/10.1115/1.3267428.

[36] Goenka, P., and Oh, K., 1986, "An Optimum Connecting Rod Design Study—a Lubrication Viewpoint." J. Tribol. **108**(3) pp. 487-493. https://doi.org/10.1115/1.3261247.

[37] Charkha, P., and Jaju, S., 2009, “Analysis & Optimization of Connecting Rod,” ieeexplore.ieee.org. DOI: 10.1109/ICETET.2009.30.

[38] Webster, W., Coffell, R., and Alfaro, D., 1983, “A Three Dimensional Finite Element Analysis of a High Speed Diesel Engine Connecting Rod.” SAE Technical Paper. https://doi.org/10.4271/831322.

[39] Folgar, F., Widrig, J., and Hunt, J., 1987, “Design, Fabrication and Performance of Fiber FP/Metal Matrix Composite Connecting Rods,” SAE Transactions, **96** (2), pp. 155-163.

[40] Strozzi, A., Baldini, A., Giacopini, M., Bertocchi, E., and Mantovani, S., 2016, “A Repertoire of Failures in Connecting Rods for Internal Combustion Engines, and Indications on Traditional and Advanced Design Methods,” Eng. Fail. Anal., **60**, pp. 20–39. https://doi.org/10.1016/j.engfailanal.2015.11.034.

[41] Witek, L., and Zelek, P. 2019, “Stress and Failure Analysis of the Connecting Rod of Diesel Engine,” Engineering Failure Analysis, **97**, pp. 374-382. https://doi.org/10.1016/j.engfailanal.2019.01.004.

[42] Rabb, R., 1996, “Fatigue Failure of a Connecting Rod,” European Structural Integrity Society, **22**, pp. 97-112. https://doi.org/10.1016/S1566-1369(97)80011-8.

[43] Ilman, M., and Barizy, R., 2015, “Failure Analysis and Fatigue Performance Evaluation of a Failed Connecting Rod of Reciprocating Air Compressor,” Engineering Failure Analysis, **56**, pp. 142-149. https://doi.org/10.1016/j.engfailanal.2015.03.010.

[44] Singh, P., Pramanik, D., and Singh, P., 2015, “Fatigue and Structural Analysis of Connecting Rod’s Material Due to (CI) Using FEA,” researchgate.net, **4**, pp. 245–253.

[45] Hussin, M., and Sinha, E., 2014, “Design and Analysis of Connecting Rod Using Aluminium Alloy 7068 T6, T6511,” academia.edu, **5**(10), pp. 57–69.

[46] Griza, S., Bertoni, F., Zanon, G., Reguly, A., and Strohaecker, T., 2009, “Fatigue in Engine Connecting Rod Bolt Due to Forming Laps,” Engineering Failure Analysis, **16** (5), pp. 1542-1548. https://doi.org/10.1016/j.engfailanal.2008.10.002.

[47] Fan, X., Pan, M., and Zhang, C., 2011, “Fatigue Analysis of Diesel Engine Connecting Rod Based on Finite Element Method,” Applied Mechanics and Materials, **39,** pp. 550-554. https://doi.org/10.4028/www.scientific.net/AMM.39.550

[48] Rahman, M. H., Rahman, S. M. M., Tanvir Bhuiya, A., and Sakib, S., 2014, "Design of an Accessible Door System in High Floor Buses for Wheel Chair Users," Int. Conf. Mech. Ind. Energy Eng 2014, Khulna, Bangladesh, December 26-27, pp 1-6.

[49] Kumar, R., Kumar, K., Kumar, P. S., Gopinath, D., and Sushma, C. V, 2015, "Design and Optimization of Four Wheeler Connecting Rod Using Finite Element Analysis," Materials today: Proceedings, **2**, pp. 2291–2299. https://doi.org/10.1016/j.matpr.2015.07.267.

[50] Mirehei, A., Zadeh, M., Jafari, A., and Omid, A., 2008, "Fatigue Analysis of Connecting Rod of Universal Tractor through Finite Element Method (ANSYS)," Journal of Agricultural Technology, **4**(2), pp. 21-27.

[51] Cho, S., Optimization, S. H.-S. and M., and 2009, "Isogeometric Shape Design Optimization: Exact Geometry and Enhanced Sensitivity," Structural and Multidisciplinary Optimization, **38**(1), pp. 53–70. https://doi.org/10.1007/s00158-008-0266-z.

[52] Sarihan, V., and Song, J., 1990, "Optimization of the Wrist Pin End of an Automobile Engine Connecting Rod with an Interference Fit." J. Mech. Des., **112**(3), pp. 406-412 .https://doi.org/10.1115/1.2912622

[53] Lee, T., and Jung, J., 2006, "Metamodel-Based Shape Optimization of Connecting Rod Considering Fatigue Life," Key Engineering Materials, **306**, pp. 211-216. https://doi.org/10.4028/www.scientific.net/KEM.306-308.211.

[54] Shenoy, P., and Fatemi, A., 2005, "Connecting Rod Optimization for Weight and Cost Reduction," SAE Technical Paper, pp. 10. https://doi.org/10.4271/2005-01-0987.

[55] Hippoliti, R., 1993 "FEM Method for Design and Optimization of Connecting rods for small two-stroke engines," In Small Engine Technology Conference, pp. 217-231.

[56] Myagkov, L., Chirskiy, S., Panchenko, V., Kharchenko, V., and Vasant, P., 2020, "Application of the Topological Optimization Method of a Connecting Rod Forming by the BESO Technique in ANSYS APDL," Adv. Intell. Syst. Comput., **1072**, pp. 239–248. https://doi.org/10.1007/978-3-030-33585-4_24.

[57] Vegi, L., and Vegi, V., 2013, "Design and Analysis of Connecting Rod Using Forged Steel," International Journal of Scientific & Engineering Research, **4**(6).

[58] Lee, M., Lee, H., Lee, T., and Jang, H., 2010, "Buckling Sensitivity of a Connecting Rod to the Shank Sectional Area Reduction," Materials & Design, **31**(6), pp. 2796-2803. https://doi.org/10.1016/j.matdes.2010.01.010.

[59] Cantamessa, M., 1998, “Investigating Productivity in Engineering Design: A Theoretical and Empirical Perspective,” Des. Product. Debate, pp. 13–31. https://doi.org/10.1007/978-1-4471-1538-0_2.

[60] Haddad, S., and Tijan, K., 1995, “An Analytical Study of Offset Piston and Crankshaft Designs and the Effect of Oil Film on Piston Slap Excitation in a Diesel Engine,” Mechanism and Machine Theory, **30**(2), pp. 271-284. https://doi.org/10.1016/0094-114X(94)00035-J.

[61] Vijaykumar, K., Manoj, U., Girish, and Rajesh, M., 2015, “Crankshaft Design Optimization to Improve Dynamic Balancing and Fatigue Strength,” International Journal of Automotive Engineering, 6(2), pp. 59-66.

[62] Thriveni, K., and Chandraiah, B., 2013, “Modeling and Analysis of the Crankshaft Using ANSYS Software,” International Journal of Computational Engineering Research, **3**(5).

[63] Chottiner, J., 1998, “Cranktrain Design for Ford’s HEV DI Diesel Engine.” SAE Technical Paper. https://doi.org/10.4271/981915.

[64] Fagan, D., 1994 “A Blackboard Approach to the Integration of Crankshaft Analysis Applications,” Proceedings of the Tenth Conference on Artificial Intelligence for Applications, pp. 231-237, doi: 10.1109/CAIA.1994.323670.

[65] “Ansys | Engineering Simulation Software” [Online]. Available: https://www.ansys.com/. [Accessed: 10-Oct-2022].

[66] process, C. G.-T. resources for materials, 2007, “EduPack,” tms.org.

[67] “Lamborghini Wants To Build A Carbon Fiber V12 Engine | CarBuzz” [Online]. Available: https://carbuzz.com/news/lamborghini-wants-to-build-a-carbon-fiber-v12-engine. [Accessed: 10-Oct-2022].

[68] “Lamborghini Developing Carbon Fiber Engine Parts » AutoGuide.Com News” [Online]. Available: https://www.autoguide.com/auto-news/2016/07/lamborghini-developing-carbon-fiber-connecting-rods.html. [Accessed: 10-Oct-2022].

[69] Untaroiu, A., Rahman, S. M. M., and Martin, C. R., 2023 “ Role of Secondary Ions on the i-v Characteristics of Oxyfuel Flame Subject to an Electric Field.” Journal of Fluids Engineering, in press.

[70] Al-Rifai, S., and Lin, C.-X., 2022, “Heat and Mass Transfer Correlations for Staggered Nanoporous Membrane Tubes in Flue Gas Crossflow,” J. Heat Transfer, **144**(6). https://doi.org/10.1115/1.4054122.

[71] “Rolls-Royce Starts Manufacture of World’s Largest Fan Blades, Made with Composites, for UltraFan Demonstrator | CompositesWorld” [Online]. Available: https://www.compositesworld.com/news/rolls-royce-starts-manufacture-of-worlds-largest-fan-blades-made-with-composites-for-ultrafan-demonstrator. [Accessed: 10-Oct-2022].

[72] Alam, M.D., Hossain, S.T., Simanto, H.S., Shoyeb, M., and Mithu, U., 2014, “Experimental and Numerical Investigation of an Air to Water Heat Exchanger.” In Proceedings of the 3rd International Conference on Mechanical, Industrial and Energy Engineering, Khulna, Bangladesh, December 26-27, pp. 1-5.

[73] Rahman, S.M. M., Warrier, R., Untaroiu, A. and Martin, C. R., 2022, “Electrical Characteristics Of The Oxyfuel Preheat Flame: 3D Computational Model Subject To Electric Bias Voltages.” Proceedings of the ASME 2022 International Mechanical Engineering Congress and Exposition, Columbus, OH, Oct 30-Nov 03.

[74] Piperni, P., and Rahman, S. M. M., 2021, “Singlepoint and Multipoint Robust Design of Airfoils using CST Functions.” In AIAA Scitech 2021 Forum (p. 1359). https://doi.org/10.2514/6.2021-1359.

[75] Alam, M. D., and Soeimanikutanaei, S., 2021, “Effects of Geometrical Configuration on the Aerodynamic Performance of the Joined Wings,” Proceedings of the ASME 2021 International Mechanical Engineering Congress and Exposition. Volume 10: Fluids Engineering. Virtual, Online. November 1–5, V010T10A051. ASME. https://doi.org/10.1115/IMECE2021-72087 .

[76] Lin, C. X. C., Al-Rifai, S., Polanka, M. D., and Bohan, B. T., 2022, “Lean Blowout Limit Prediction for Combustion in a Swirler by a New IndicatorAssisted RANS Approach,” AIAA SciTech Forum 2022, San Diego, CA &Virtual. https://doi.org/10.2514/6.2022-0824.

[77] Rahman, S.M. M., and Mashud, M., 2014 "Simulation investigation on flow characteristics for the flow over a propeller used in VTOL RC aircrafts," In International Conference on Mechanical, Industrial and Energy Engineering. 2014.Khulna, December 26-27, pp. 1-6.

VITA

MOHAMMAD DIDARUL ALAM

2011-2015	B.Sc., Mechanical Engineering Khulna University of Engineering & Technology Khulna, Bangladesh
2018-2021	M.S., Mechanical Engineering Florida International University Miami, Florida
2021 -2022	Doctoral Candidate Florida International University Miami, Florida

PUBLICATIONS AND PRESENTATIONS

[1] Alam, M. D., and Cao, Y., 2021, "Static and Modal Analysis of a Crankshaft Reciprocating Driver for Reciprocating-Airfoil (RA) Driven VTOL Aircraft," Mech. Based Des. Struct. Mach., pp. 1–16. https://doi.org/10.1080/15397734.2021.1991807

[2] Alam, M. D., Almas, M., Soleimanikutanaei, S., and Cao, Y., 2022, "Experimental and Analytical Studies of Reciprocating Flow Heat Transfer in a Reciprocating Loop Device for Electronics Cooling," Fluids, **7**(4), p. 132. https://doi.org/10.3390/fluids7040132.

[3] Alam, M., Popoola, O. T., and Cao, Y., 2019, "MECHANICALLY DRIVEN OSCILLATING FLOW COOLING LOOPS – A REVIEW," Front. Heat Mass Transf., **13**, p. 17. DOI: 10.5098/hmt.13.17.

[4] Imumbhon, J. O., Alam, M. D., and Cao, Y., 2021, “Design and Structural Analyses of a Reciprocating S1223 High-Lift Wing for an RA-Driven VTOL UAV,” Aerospace, **8**(8), p. 214. https://doi.org/10.3390/aerospace8080214.

[5] Alam, M. D., and Soeimanikutanaei, S., 2021, “Effects of Geometrical Configuration on the Aerodynamic Performance of the Joined Wings,” Proceedings of the ASME 2021 International Mechanical Engineering Congress and Exposition. Volume 10: Fluids Engineering. Virtual, Online. November 1–5, V010T10A051. ASME. https://doi.org/10.1115/IMECE2021-72087 .

[6] Imumbhon, J. O., Alam, M.D., Cao, Y., 2021, “Structural and Modal Analyses of an S1223 High Lift Airfoil Wing for Drone Design,” International Conference on Mechanical and Aerospace Engineering, 15(09),

[7] Alam, M.D., Hossain, S.T., Simanto, H.S., Shoyeb, M., and Mithu, U., 2014, “Experimental and Numerical Investigation of an Air to Water Heat Exchanger.” In Proceedings of the 3rd International Conference on Mechanical, Industrial and Energy Engineering, Khulna, Bangladesh, December 26-27, pp. 1-5.

[8] Mithu, M.S.U., Hossain, M.S., Haque, M.E., Alam, M.D., Simanto, H.S. and Hossaim, S.T., 2014, “Analysis of Renewable Sources as a Solution to Power Crisis in Bangladesh,” In Proceedings of the 3rd International Conference on Mechanical, Industrial and Energy Engineering, Khulna, Bangladesh, December 26-27, pp. 1-5.